



THE CALIBRATION OF BISTATIC RADAR CROSS SECTION MEASUREMENTS

THESIS

Christopher J. Bradley, Second Lieutenant, USAF

AFIT/GE/ENG/01M-03

Approved for public release, distribution unlimited

20010706 169

THE CALIBRATION OF BISTATIC RADAR CROSS SECTION MEASUREMENTS

THESIS

Presented to the Faculty of the Graduate School of Engineering and Management

of the Air Force Institute of Technology

Air University

Air Education and Training Command

In Partial Fulfillment of the Requirements for the
Degree of Masters of Science in Electrical Engineering

Christopher J. Bradley, B.S.E.E

Second Lieutenant, USAF

March 2001

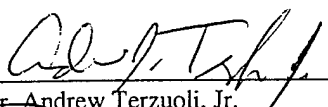
Approved for public release, distribution unlimited

The views expressed in this thesis are those of the author and do not reflect the official policy or position of the Department of Defense or the United States Government.

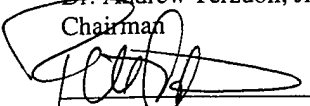
THE CALIBRATION OF BISTATIC RADAR CROSS SECTION MEASUREMENTS

Christopher J. Bradley, B.S.E.E.
Second Lieutenant, USAF

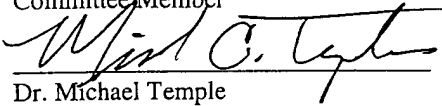
Approved:



Dr. Andrew Terzuoli, Jr.
Chairman



Major Peter Collins, Ph. D.
Committee Member



Dr. Michael Temple
Committee Member

2 Mar 2001
date

2 MAR 01
date

2 Mar 01
date

TABLE OF CONTENTS

TABLE OF CONTENTS	I
ACKNOWLEDGEMENTS	III
LIST OF FIGURES	V
LIST OF TABLES	VII
ABSTRACT.....	VIII
1 INTRODUCTION.....	1
2 BACKGROUND.....	6
2.1 DEFINITION OF TERMS.....	6
2.1.1 <i>Scattering</i>	6
2.1.2 <i>Radar cross section</i>	6
2.1.3 <i>Bistatic scattering regions</i>	7
2.1.4 <i>Scattering mechanisms</i>	8
2.1.5 <i>Polarization</i>	10
2.1.6 <i>Scattering matrix</i>	11
2.1.7 <i>Subsystem Distortion matrix</i>	12
2.1.8 <i>Near-field and far-field</i>	12
2.2 COORDINATE CONVENTION.....	13
2.3 SOURCES OF MEASUREMENT INACCURACY.....	14
2.3.1 <i>Reflections from chamber walls and mounting apparatus</i>	15
2.3.2 <i>Antenna coupling</i>	15
2.3.3 <i>Subsystem distortion</i>	16
2.3.4 <i>Object alignment error</i>	16
2.3.5 <i>Near-field effects</i>	17
2.4 RANGE GATING AND BACKGROUND SUBTRACTION	17
2.5 TYPES AND APPLICABILITY OF CALIBRATION.....	21
2.5.1 <i>Amplitude and phase (Type-1) calibration</i>	21
2.5.2 <i>Simple polarimetric (Type-2) calibration</i>	22
2.5.3 <i>Fully polarimetric (Type-3) calibration</i>	24
3 BISTATIC CALIBRATION METHODS.....	25
3.1 BASIC TYPE-1 CALIBRATION.....	25
3.2 EMSL SIMPLE POLARIMETRIC CALIBRATION	25
3.3 GENERALIZED DUAL-ANTENNA CALIBRATION	29
3.4 BISTATIC VIA MONOSTATIC CALIBRATION.....	33
4 METHODOLOGY.....	36
4.1 PURPOSE.....	36
4.2 RESOURCES REQUIRED	38
4.3 APPROACH.....	39
4.3.1 <i>Assessment of Air Force-wide calibration needs</i>	39
4.3.2 <i>Calibration object selection</i>	40
4.3.3 <i>Experimental validation of measurement facility</i>	42
4.3.4 <i>Validation of measurements via computational methods</i>	42
4.3.5 <i>Implementation of calibration techniques</i>	43

4.4	CHARACTERIZATION OF THE EMSL	43
4.4.1	<i>Design of the EMSL</i>	44
4.4.2	<i>Alignment of reference objects</i>	45
4.4.3	<i>Antenna polarization purity</i>	47
4.4.4	<i>Signal-to-noise ratio and repeatability</i>	49
4.4.5	<i>Ease, efficiency, and versatility</i>	51
4.5	MEASUREMENT	52
5	RESULTS.....	54
5.1	DIHEDRAL (MONOSTATIC)	54
5.2	DIHEDRAL (BISTATIC)	58
5.3	LONG CYLINDER	58
5.4	SQUAT CYLINDER.....	61
5.5	TRIHEDRAL.....	64
5.6	CIRCULAR DISK.....	66
5.7	SPHERE.....	67
5.8	WIRE MESH.....	70
5.9	INITIAL CALIBRATION ANALYSIS	73
5.10	BASIC TYPE-1 CALIBRATION TECHNIQUE	75
5.11	EMSL SIMPLE POLARIMETRIC CALIBRATION TECHNIQUE.....	77
5.12	GENERALIZED DUAL-ANTENNA CALIBRATION TECHNIQUE.....	79
5.13	BICOMS FULL-POLARIMETRIC CALIBRATION TECHNIQUE.....	83
6	CONCLUSIONS	86
6.1	CALIBRATION OBJECT SELECTION.....	86
6.2	PERFORMANCE OF TYPE-1, TYPE-2, AND TYPE-3 CALIBRATIONS.....	87
	APPENDIX A: VALIDATION OF MBETS AND MOM COMPUTATIONS.....	89
6.3	MBET THEORY.....	89
6.4	METHODOLOGY	96
6.5	RESULTS.....	98
6.5.1	<i>Far-field MoM code and MBET evaluation</i>	98
6.5.2	<i>Near-field MBET evaluation (fixed-angle bistatic RCS)</i>	99
6.5.3	<i>Near-field MBET evaluation (swept angle bistatic RCS)</i>	100
6.5.4	<i>Near-field MBET evaluation (swept range bistatic RCS)</i>	104
6.5.5	<i>Conclusions</i>	106
	APPENDIX B: MATLAB SCRIPTS	108
	APPENDIX C: THE EMSL.....	142
	BIBLIOGRAPHY	145

ACKNOWLEDGEMENTS

The completion of this work was a result of the collaboration of many individuals who have made selfless and invaluable contributions to the end product. I would first like to thank Dr. Andrew Terzuoli, for his encouragement and dedication to making this the best thesis possible by bringing a wide spectrum of knowledgeable sources into the fold. Also, Major Peter Collins offered essential technical help in the computational and measurement rigors involved in the work, and for making the tremendous sacrifice of trekking to Italy to supervise me for a week. Dr. Michael Temple's perspective and meticulous feedback in the process of publishing our conference papers is also much appreciated.

I would also like to thank the fantastic people of the Technologies for Detection and Positioning of Landmines, headed by Dr. Alois Sieber, at the Joint Research Center in Ispra, Italy, especially Dr. Giuseppe Nesti, who made it possible to perform the measurements at his laboratory, Dr. Gareth Lewis and Joaquim Fortuny for their willingness to pour time and effort into my research, and for their friendship while I was at their facility. I am indebted to them for making this whole project possible.

Dr. Ron Marhefka, from the Electrosience Laboratory at The Ohio State University helped me tremendously in the early stages of this project. Special thanks go to Dr. Alan Buterbaugh, Dr. Rob Layden, Dr. Bill Kent, and Dr. Byron Welsh of Mission Research Corporation. They all provided essential direction and insight that could only have been a result of years of experience in the field.

LIST OF FIGURES

FIGURE 1: MONOSTATIC AND BISTATIC CONFIGURATIONS (EIGEL, 1999)	2
FIGURE 2: BISTATIC SCATTERING REGIONS	7
FIGURE 3: WAVE POLARIZATION	10
FIGURE 4: FORWARD SCATTERING COORDINATE CONVENTION (ULABY AND ELACHI, 1990)	13
FIGURE 5: ANTENNA COUPLING IN FORWARD SCATTERING REGION	15
FIGURE 6: TIME-DOMAIN SPHERE RCS (HH-POL) WITH BACKGROUND SUBTRACTION (RIGHT) AND WITHOUT SUBTRACTION (LEFT)	19
FIGURE 7: TIME-DOMAIN SPHERE RCS (HH-POL) WITH 10 NS RANGE GATE APPLIED	21
FIGURE 8: BICOMS CALIBRATION GEOMETRY (ALEXANDER, ET AL, 1995).....	33
FIGURE 9: VALIDATION OF VV-POL MEASUREMENT IN EMSL	43
FIGURE 10: PHYSICAL LAYOUT OF THE EMSL	44
FIGURE 11: ALIGNMENT OF CALIBRATION DISK IN THE EMSL	46
FIGURE 12: REPEATABILITY COMPARISON OF CALIBRATION DISK MEASUREMENTS	47
FIGURE 13: ANTENNA CROSS-POLARIZATION PURITY	48
FIGURE 14: REPEATABILITY OF A MEASUREMENT OF THE 30.5 CM METALLIC SPHERE, $\alpha=120^\circ$	50
FIGURE 15: NOISE FLOOR DERIVED FROM SPHERE MEASUREMENT (512-AVERAGING)	51
FIGURE 16: MEASUREMENT OF CIRCULAR DISK WITH SYSTEMATIC MISALIGNMENT	53
FIGURE 17: MoM SIMULATION OF AN EMSL MONOSTATIC MEASUREMENT OF THE VERTICAL DIHEDRAL ..	56
FIGURE 18: CALIBRATED RCS RATIOS OF MEASUREMENT OF DIHEDRAL IN TWO ORIENTATIONS— PERFORMED IN THE EMSL	57
FIGURE 19: EMSL MEASUREMENTS (TYPE-2 CALIBRATED) OF THE LONG CYLINDER	59
FIGURE 20: EMSL MEASUREMENTS OF FIGURE 19 VS. MoM SIMULATIONS	60
FIGURE 21: EMSL MEASUREMENT OF LONG CYLINDER, TILTED 45°	61
FIGURE 22: EMSL MEASUREMENT OF SHORT CYLINDER, TILTED 45°	62
FIGURE 23: EMSL MEASUREMENTS (TYPE-2 CALIBRATED) OF THE SHORT CYLINDER	63
FIGURE 24: EMSL MEASUREMENTS OF FIGURE 23 VS. MoM SIMULATION	64
FIGURE 25: EMSL MEASUREMENT OF THE TRIHEDRAL	65
FIGURE 26: EMSL MEASUREMENT OF FIGURE 25 VS. MoM SIMULATION	66
FIGURE 27: EMSL MEASUREMENT OF THE SMALL DISK VS. PO PREDICTION	67
FIGURE 28: EMSL MEASUREMENT OF THE 30.5 CM DIAMETER SPHERE	68
FIGURE 29: EMSL MEASUREMENT OF FIGURE 28 VS. MIE SERIES PREDICTION.....	69
FIGURE 30: EMSL MEASUREMENT OF WIRE MESH (VERTICAL ORIENTATION).....	70
FIGURE 31: EMSL MEASUREMENT OF WIRE MESH (ORIENTED 45° COUNTER-CLOCKWISE).....	71
FIGURE 32: METALLIC SPHERE CALIBRATED USING BASIC TYPE-1 CALIBRATION TECHNIQUE	73
FIGURE 33: METALLIC SPHERE CALIBRATED USING SIMPLE POLARIMETRIC CALIBRATION TECHNIQUE	74
FIGURE 34: METALLIC SPHERE CALIBRATED USING BISTATIC VIA MONOSTATIC CALIBRATION TECHNIQUE ..	74
FIGURE 35: METALLIC SPHERE CALIBRATED USING THE GENERAL DUAL-ANTENNA CALIBRATION TECHNIQUE	75
FIGURE 36: ERROR IN GCT CALIBRATION USING SMALL DISK, VERTICAL, AND TILTED DIHEDRAL	80
FIGURE 37: ERROR IN GCT CALIBRATION WITH 2° MISALIGNMENT ASSOCIATED WITH EACH REFERENCE OBJECT	81
FIGURE 38: FALCONER'S MBET GEOMETRY. R IS OBSERVATION SPHERE RADIUS, α AND β OBSERVATION ANGLES, BOTH PRESUMED SMALL, D REPRESENTS OBJECT'S NOMINAL DIAMETER, AND H ITS NOMINAL HEIGHT RELATIVE TO THE ILLUMINATION DIRECTION. (FALCONER, "EXTRAPOLATION OF...", 1988) ...	94
FIGURE 39: TEST OBJECTS (DIMENSIONS IN MM) (EIGEL, 1999).....	97
FIGURE 40: OBJECT A MEASURED VS. PREDICTED BISTATIC RCS, VV POLARIZATION, 8 HGz, 0° TRANSMIT ANGLE.....	98
FIGURE 41: OBJECT B MoM VS. F2 MBET FIXED ANGLE BISTATIC RCS, HH POLARIZATION, 8 GHZ, 10° BISTATIC ANGLE.	100
FIGURE 42: MBET ERROR PLOT FOR A 0° TRANSMITTER ANGLE. THIN LINE: OBJECT A, THICK LINE: OBJECT B. DASHED LINES ARE FOR THE F1 MBET AND SOLID LINES ARE FOR THE F2 MBET.	101
FIGURE 43: MBET ERROR PLOT FOR A 45° TRANSMITTER ANGLE.	102
FIGURE 44: MBET ERROR PLOT FOR A 135° TRANSMITTER ANGLE.	102

FIGURE 45: FALCONER'S F1 MBET ERROR PLOT.....	103
FIGURE 46: FALCONER'S F1 MBET ERROR PLOT.....	104
FIGURE 47: FALCONER'S F1 MBET ERROR PLOT.....	104
FIGURE 48: OBJECT A MBET VS. MOM.....	105
FIGURE 49: OBJECT A RANGE DEPENDENT ERROR PLOT.....	105
FIGURE 50: OBJECT B MBET VS. MOM.....	105
FIGURE 51: OBJECT B RANGE DEPENDENT ERROR PLOT.....	106

LIST OF TABLES

TABLE 1: TEST MATRIX	41
TABLE 2: AVERAGE ALIGNMENT ERROR STATISTICS FOR TYPE-1 CALIBRATION (SMALL DISK).....	76
TABLE 3: ERROR STATISTICS FOR TYPE-1 CALIBRATION (METALLIC SPHERE).....	76
TABLE 4: ERROR STATISTICS FOR TYPE-1 CALIBRATION (DIHEDRAL TILTED 22.5°).....	77
TABLE 5: ERROR STATISTICS FOR EMSL CALIBRATION (T1: SMALL DISK, T2: VERTICAL WIRE MESH, T3: TILTED WIRE MESH)	78
TABLE 6: ERROR STATISTICS FOR MODIFIED EMSL CALIBRATION (T1: SMALL DISK, T2: DIHEDRAL TILTED 22.5°)	79
TABLE 7: AVERAGE ALIGNMENT ERROR STATISTICS FOR GCT CALIBRATION (T1: SMALL DISK, T2: VERTICAL DIHEDRAL, T3: TILTED DIHEDRAL)	82
TABLE 8: ERROR STATISTICS FOR GCT CALIBRATION (T1: TILTED DIHEDRAL, T2: SMALL DISK, T3: VERTICAL DIHEDRAL)	82
TABLE 9: ERROR STATISTICS FOR BICOMS CALIBRATION (T0: SMALL DISK, T1: SHORT CYLINDER, T2: TILTED DIHEDRAL, T3: VERTICAL DIHEDRAL)	84
TABLE 10: BISTATIC RCS MEASUREMENT	97
TABLE 11: ANGULAR SIZE OF VALID REGIONS FOR EACH OF FALCONER'S MBETS.....	102

ABSTRACT

Recent advances in signal processing and remote sensing have highlighted the importance of bistatic radar systems for the purposes of environmental monitoring, surveillance, and tracking radar. The calibration of such systems has been problematic—much more so than similar monostatic systems, primarily as a result of the lack of reference objects suitable for calibrating at any given bistatic angle. This research deals with the problems of calibrating full-polarimetric laboratory-environment bistatic radar systems, including the lack of suitable calibration targets and procedures, and operational considerations such as alignment and mounting. Several popular bistatic calibration techniques are classified, evaluated, and comparisons are made between the relative merits of various calibration objects. The analysis addresses sensitivity to target alignment error, sensitivity to polarization impurity, and ease of implementation. Both theoretical concepts and practical considerations are discussed, based on measurements accomplished at the European Microwave Signature Laboratory (EMSL) of the Joint Research Center (JRC) in Ispra, Italy. Significant gains in co-polarized channel accuracy and cross-polarization purity are realized with calibrations that utilize the complete system distortion model, and these conclusions are discussed in detail.

THE CALIBRATION OF BISTATIC RADAR CROSS SECTION MEASUREMENTS

1 INTRODUCTION

Radar calibration is a procedure used to compensate for irregularities in the hardware or measurement systems and to account for systematic error-producing phenomenon present in the measurement. A good radar calibration technique takes into consideration the uniqueness of each measurement system as well as its application. Applications for radar calibration come in two main configurations: *monostatic* and *bistatic*.

Figure 1 shows the difference between the monostatic and bistatic geometries. Monostatic radar is defined as a system that transmits a radio-frequency electromagnetic wave and receives the scattered wave at the same location for the purposes of detection and ranging of objects within the antenna's illumination area. Typically, a monostatic radar will employ a single antenna that is switched between transmit and receive modes. Often, however, two closely placed antennas are used; one for transmission and one for reception. This mitigates problems due to cross talk between the Tx/Rx channels, and allows each antenna to be designed specifically for transmitting or receiving.

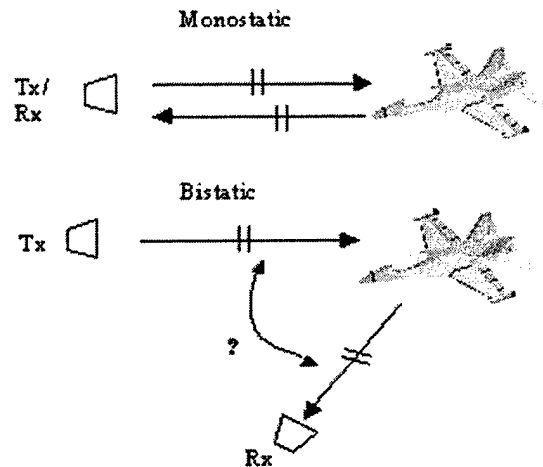


Figure 1: Monostatic and Bistatic Configurations (Eigel, 1999)

The proper calibration of radars is highly dependent on the type. A *monostatic calibration* is one that is designed to calibrate based on the considerations for monostatic measurements. This type of calibration is relatively straightforward and the procedures follow well-known heuristics. *Bistatic calibration*, however, is much more complicated. Additional measurement concerns such as the presence of more than one antenna, cabling and non-linearities in antenna phase response over the angular sweep, and calibration object selection make this type of calibration difficult. Much less is known about bistatic calibration, though bistatic radar itself has been in development almost as long as monostatic radar. It is a direct result of recent advantages in signal processing capabilities that bistatic radar, and thus bistatic calibration, have become popular.

The use of bistatic radar has its advantages over the monostatic case. The electromagnetic scattering *signature* (most often referred to as *radar cross-section*, or RCS) can be determined in a much more complete way as opposed to monostatic radar. Monostatic radar can only observe the *backscatter* of an object, or the radiation that returns from the object directly back in the direction of the source. We know from

electromagnetic scattering theory that objects, in general, radiate in *all* directions, not just the backscatter direction. A bistatic measurement can observe how the object scatters in every direction in a plane that intersects the object, for a given look angle. The disadvantage of bistatic radar is directly coupled to its main advantage. A complete bistatic measurement can require hundreds of times the amount of data as a monostatic measurement for a given look angle. Analysis of the data becomes computationally expensive and much less intuitive than in the monostatic case.

The inherent advantage to bistatic radar has a direct impact the future of U.S. Air Force operations. Currently, low observable (LO) aircraft have been designed to have a low backscatter cross-section. It can be shown that using aircraft shaping techniques to reduce the backscatter return of LO aircraft tends to *increase* the bistatic RCS of the same aircraft (Tuley, Alexander, 1995), thereby increasing its probability of detection. With the increased use of bistatic radar for aircraft detection, the threat to U.S. LO aircraft increases accordingly. It is for this reason that it is necessary to understand bistatics and how best it can be used for the detection of low observables. A logical first step to this end would be to develop a way to maximize the accuracy with which one can measure the bistatic scattering characteristics of a given object, ergo the need for efficient and precise calibration techniques.

Two major problems exist that make bistatic calibration difficult. First of all, the reference objects preferred in monostatic calibration such as dihedrals and trihedrals are not appropriate for bistatic measurements. For monostatic backscatter measurements, dihedrals and trihedrals have a high radar return, which ensures data collection within the dynamic range of the radar system. In addition, the theoretical backscatter of these

objects can be easily and precisely calculated based on specular scattering. For any measurement other than backscatter, i.e. bistatic measurements, these objects are no longer desirable. The response of the object is no longer dominated by specular scattering, and as a result the theoretical response is much more difficult to calculate precisely, and the radar return will be much lower at some bistatic angles, which makes accurate calibration difficult. Other objects such as spheres, cylinders, and plates are often used for bistatic reference objects, since their solution can be calculated more easily, and the radar return is sufficiently high for most bistatic angles.

The second problem is that the theoretical RCS of the reference objects for a bistatic calibration, which are necessary to compare with the measurement in order to calibrate, are often more rigorous than in a monostatic calibration. In a complete, *full-polarimetric* calibration for instance, usually three objects are used and each must have precisely known scattering characteristics, which often means several days of moment method calculations on a fast computer.

This work addresses the problem of finding suitable calibration objects for bistatic calibration, and also evaluates the various techniques that are currently used and are available in current literature. Calibration techniques detailed in (Alexander et al., 1995), (Jersak, 1993), (Kahny, et al., 1992), (Mortensen, 1995), (Ulaby, Elachi, 1990), and (Whitt et al, 1991) were performed at the European Microwave Signature Laboratory (EMSL) of the European Commission Joint Research Center (JRC) in Ispra, Italy. The EMSL was chosen as the location to perform the measurements because of its capability and availability to produce far-field, fully polarimetric, bistatic measurements on a variety of objects. The precision of this facility is of paramount importance for the

objects can be easily and precisely calculated based on specular scattering. For any measurement other than backscatter, i.e. bistatic measurements, these objects are no longer desirable. The response of the object is no longer dominated by specular scattering, and as a result the theoretical response is much more difficult to calculate precisely, and the radar return will be much lower at some bistatic angles, which makes accurate calibration difficult. Other objects such as spheres, cylinders, and plates are often used for bistatic reference objects, since their solution can be calculated more easily, and the radar return is sufficiently high for most bistatic angles.

The second problem is that the theoretical RCS of the reference objects for a bistatic calibration, which are necessary to compare with the measurement in order to calibrate, are often more rigorous than in a monostatic calibration. In a complete, *full-polarimetric* calibration for instance, usually three objects are used and each must have precisely known scattering characteristics, which often means several days of moment method calculations on a fast computer.

This work addresses the problem of finding suitable calibration objects for bistatic calibration, and also evaluates the various techniques that are currently used and are available in current literature. Calibration techniques detailed in (Alexander et al., 1995), (Jersak, 1993), (Kahny, et al., 1992), (Mortensen, 1995), (Ulaby, Elachi, 1990), and (Whitt et al, 1991) were performed at the European Microwave Signature Laboratory (EMSL) of the European Commission Joint Research Center (JRC) in Ispra, Italy. The EMSL was chosen as the location to perform the measurements because of its capability and availability to produce far-field, fully polarimetric, bistatic measurements on a variety of objects. The precision of this facility is of paramount importance for the

accurate evaluation of these sometimes-sensitive measurements and calibration techniques.

The scope of the project provided for a performance analysis of existing techniques based on the following factors:

- Sensitivity of calibration to reference object alignment error
- Sensitivity to antenna polarization impurity
- Robustness and repeatability of the technique
- Applicability to fixed-bistatic or true bistatic measurements
- Ease and efficiency of implementation

The following pages introduce the theoretical and practical concepts of bistatic measurements and calibration, and also document the process, analysis, results, and conclusions of the experimentation.

2 BACKGROUND

2.1 Definition of Terms

2.1.1 Scattering

When an electromagnetic wave strikes a material discontinuity (in the case of radar, a wave traveling in free space strikes an object), electric currents are induced in the region of the discontinuity. These currents travel within or on the surface of the body and re-radiate an electromagnetic field. The radiation can, in general, be in any direction. This re-radiation is called *scattering*. The manner in which an object scatters radiation is highly dependent on the geometry of an object and the direction of the incident radiation, and thus any given object has its own unique scattering signature.

2.1.2 Radar cross section

Radar cross-section (RCS) is a measure of the magnitude of the electromagnetic scattering of an object with reference to a metal sphere. If a metal sphere were constructed to produce the same scattered power that the object scatters the cross-sectional area of that sphere would be the object's radar cross-section. RCS is defined mathematically as:

$$\sigma = \lim_{R \rightarrow \infty} 4\pi R^2 \frac{|E_s|^2}{|E_i|^2} \quad (1)$$

Where R is the range from the transmitting antenna to the scatterer, E_s is the scattered E-field (V/m), and E_i is the incident E-field.

2.1.3 Bistatic scattering regions

At different bistatic angles, measurement considerations can change significantly. For the purposes of this project, the regions of bistatic scattering are separated into three zones: *quasi-monostatic*, *normal bistatic*, and *forward scatter*. Figure 2 shows these regions and the placement of the receiving antenna at the boundaries.

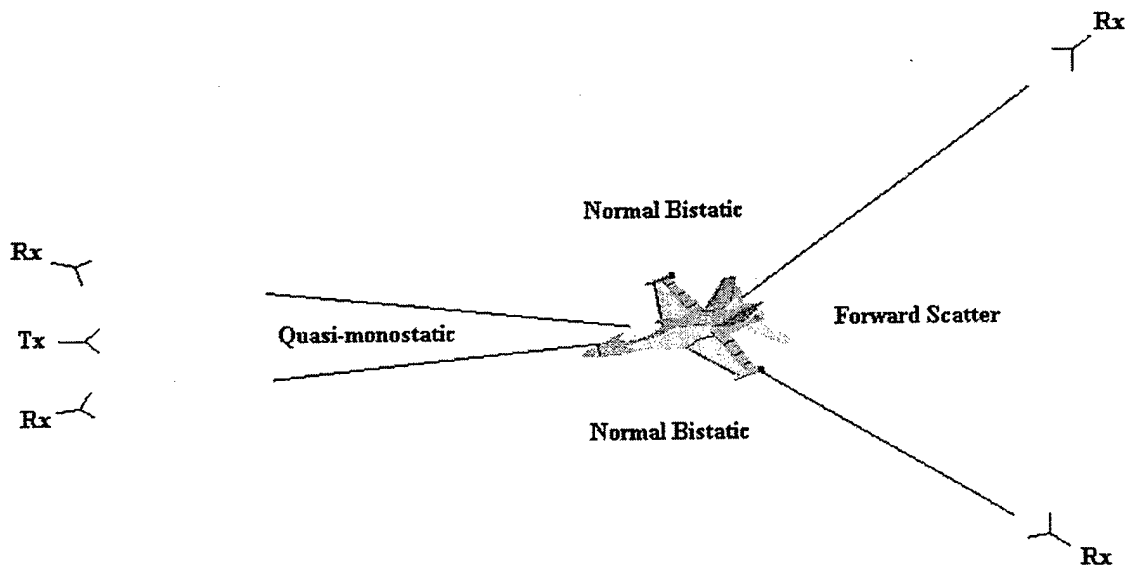


Figure 2: Bistatic Scattering Regions

In the quasi-monostatic region, the transmitter and receiver are not co-located as in the true monostatic case, but have a small angular separation. The size of the quasi-monostatic region is dependent on the type of object to be measured. For many simple objects, the quasi-monostatic RCS will be almost identical to the monostatic RCS, with a correction applied. Corrections of this type, called *monostatic-to-bistatic equivalence theorems* (MBETs), have been studied in depth in (Kell, 1965) and will not be elaborated on any further in this paper. More complex objects may have an RCS that varies

significantly at small angles, and the region defined to be quasi-monostatic may be much smaller.

In the normal bistatic region, MBETs in general do not apply. RCS in this region is generally less than in the quasi-monostatic region, but large variances in RCS may arise as a result of the object geometry. As a consequence, reference object selection for bistatic calibration in this region is very difficult.

In the forward scattering region, the electromagnetic signature of the object is better characterized by its *shadow*, or absence of scattered energy in this area. However, this is exceedingly difficult to measure. The power received at the receiver begins to be dominated by the incident field rather than the scattered field, as the receiver approaches the main beam of the transmitter. In this region, accurate measurements are nearly impossible due to the large ratio of incident energy to scattered energy.

2.1.4 *Scattering mechanisms*

The type of scattering mechanism that dominates on a particular body is an important factor in reference object selection. It is desired that the bodies scatter in a predictable way for many bistatic angles, and some mechanisms are more predictable than others.

Specular reflection is the dominant scattering mechanism for bodies with features much larger than one wavelength (λ). It occurs when a wave strikes a smooth surface and reflects back at the same angle from the normal vector to the surface (Snell's Law). The method of Geometrical Optics (GO) predicts this mechanism by the use of ray tracing (Balanis, 1989). Specular reflection tends to produce a larger radar return from an

incident plane wave, because the wave *spreading* is much less than in the case of diffraction, dependent on the geometry. Spreading is a term used to describe the attenuation of an electromagnetic wave, due to the divergence of rays as it propagates. For a plane wave, the rays spread at a rate proportional to the square root of the distance. As the wave reflects off an object, the spreading in the return path will be a function of the curvature of the illuminated surface. A convex surface with a small radius of curvature will cause the wave to spread more, and a flat surface will introduce no additional spreading. Thus, for objects with relatively large, flat features, specular reflection will be the dominant scattering mechanism.

Diffraction can be produced in a number of different ways. For complex geometries, it is likely that diffraction may be the dominant scattering mechanism on the body. For a large set of geometries, diffraction can be modeled as a local phenomenon and solved for numerically with the Uniform Geometrical Theory of Diffraction (UTD) (Kouyoumjian, Pathak, 1974). This technique predicts diffraction from features that create an instantaneous change of the radius of curvature on an object. It models an arbitrary object as an assembly of canonical objects that the code can calculate precisely. This set includes objects such as plates, cylinders, spheroids, ellipsoids, cone frustrums, etc. Other mechanisms of diffraction are *surface traveling waves*, which, depending on the polarization of the incident wave, will propagate along the surface of the body and produce diffractions at edges. Surface waves that travel in the non-illuminated region (or shadow region) of the object are called *creeping waves*.

An object with a large number of diffraction-producing features can be calculated using asymptotic high-frequency codes. Codes utilizing GO, Physical Optics (PO), UTD,

or the Physical Theory of Diffraction (PTD), are often used, but it is sometimes not well-known whether the solution that is output will be completely accurate, especially in the case of bistatic predictions. For complex bodies it is usually desirable to use a prediction code based on the Method of Moments (MoM) (Harrington, 1993), which can produce an exact solution at the cost of computational time.

2.1.5 Polarization

The term polarization refers to the alignment of the electric field vector with respect to whatever coordinate system is in use. In general, the electric field will rotate as it propagates through the medium. This is *elliptical polarization*. In the case of most radar measurements, the *linearly polarized* waves are used; meaning the alignment of the electric field vector does not change as a function of time or distance.

The E-field, H-field, and direction of propagation (β) are all mutually orthogonal, as seen in Figure 3.

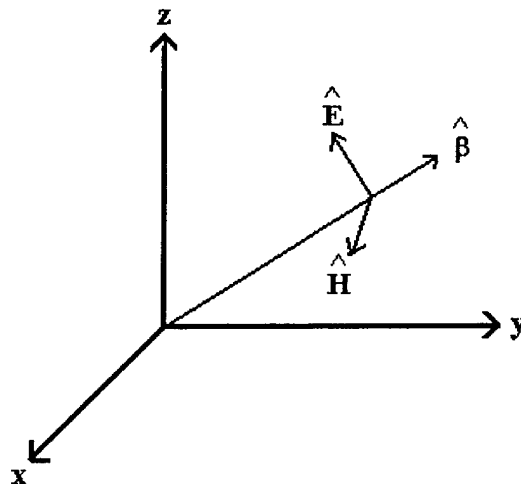


Figure 3: Wave Polarization

The typical naming convention for polarization is horizontal (H-pol) and vertical (V-pol). An H-polarized wave is transmitted with the E-field vector aligned parallel to

the horizontal axis (in the x-y plane), and a V-polarized wave is transmitted with the E-field vector aligned perpendicular to the horizontal axis (parallel to the z-axis). A *polarimetric* measurement is one that transmits and receives every combination of polarizations. In other words, HH, VV, (co-polarized); HV, and VH (cross-polarized) data are collected, where the first letter identifies the received polarization, and the second letter identifies the transmitted polarization. Thus the polarization “HV” means that a vertically polarized field was transmitted, and the receiver collected the horizontally polarized field. The collection of cross-polarized data gives a more unique description of the object scattering characteristics. Some object geometries may *depolarize* one or more polarizations, meaning the polarization that is reflected had a component perpendicular to the polarization that was transmitted. The field of radar polarimetry is dedicated to the analysis of this type of measurement.

2.1.6 *Scattering matrix*

A polarimetric measurement gathers four complex RCS values for a measurement of a single bistatic angle and frequency. These values are arranged into a 2 x 2 complex scattering matrix. Scattering matrices usually take the form

$$\mathbf{S} = \begin{bmatrix} HH & VH \\ HV & VV \end{bmatrix}$$

where the elements HH, VH, HV, and VV are the amplitude and phase of each respective measurement. The scattering matrix is also referred to as the *Sinclair matrix*. The matrix representation of a polarimetric measurement becomes very useful in performing calibrations for analysis and calibration, as we will see in the chapters to follow.

2.1.7 Subsystem Distortion matrix

The errors introduced into a measurement as a result of non-ideal hardware systems can be calculated using two 2x2 complex matrices called *subsystem distortion matrices*. The two matrices correspond to the distortion of the receiver subsystem and the transmitter subsystem, as given by:

$$\mathbf{R} \equiv \begin{bmatrix} R_{HH} & R_{VH} \\ R_{HV} & R_{VV} \end{bmatrix} \qquad \mathbf{T} \equiv \begin{bmatrix} T_{HH} & T_{VH} \\ T_{HV} & T_{VV} \end{bmatrix}$$

Where \mathbf{R} is the receiver subsystem distortion matrix and \mathbf{T} is the transmitter subsystem distortion matrix. The matrices operate on the actual value of the object scattering matrix (thereby *distorting* the actual RCS) to yield the value of the measurement of the same object. The object's measured scattering matrix can be expressed as

$$\mathbf{M} = \mathbf{RST} \tag{2}$$

Where \mathbf{M} is the measured 2x2 scattering matrix and \mathbf{S} is the actual scattering matrix.

2.1.8 Near-field and far-field

In RCS measurements, the incident wave is assumed to be a plane wave. The reason is that in an actual radar scenario, especially that involving ground-based radar illuminating an aircraft, the object is located at a long range from the illuminating antenna. The wavefront of this antenna is roughly spherical, so the radius of curvature of the wavefront is the range from the antenna to the object. At long ranges such as these, the radius of curvature is large enough so that the wavefront looks planar.

The region in which a spherical wave front can be assumed to be planar is called the *far-field*. At ranges smaller than this, it is called the *near-field*.

2.2 Coordinate Convention

With the wide variety of measurement facilities and conventions, the H- and V-polarization conventions can sometimes be ambiguous. For this reason it is desirable to link the convenience of the H and V notation with the spherical coordinate system in order to eliminate confusion. For the measurement geometry of the EMSL, the plane in which the receiver tracks is taken to be the y-z plane, and the z-axis is perpendicular to the ground. The coordinate convention most convenient for this configuration is described in (Ulaby, Elachi, 1990), and is depicted in Figure 4 below, although the same system is used for measurements in other configurations (for example, in (Sarabandi, et al, 1990)).

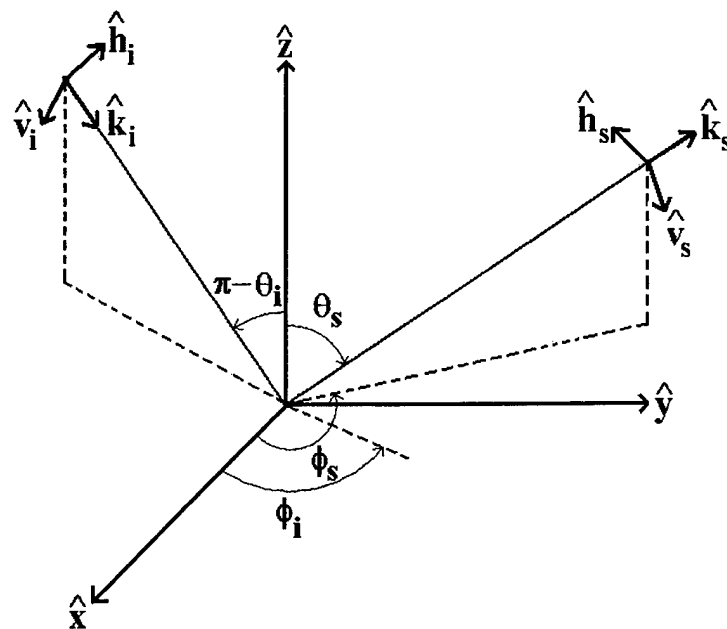


Figure 4: Forward Scattering Coordinate Convention (Ulaby and Elachi, 1990)

Here the \mathbf{h} and \mathbf{v} unit vectors corresponding to their respective polarizations correspond directly to the ϕ and θ unit vectors, respectively. The \mathbf{v} and \mathbf{h} directions for the incident field (\mathbf{v}_i and \mathbf{h}_i) and the scattered field (\mathbf{v}_s and \mathbf{h}_s) are defined with respect to

the direction of propagation (\mathbf{k}_i and \mathbf{k}_s), making this a *wave oriented* coordinate system. The set of equations governing the directions of propagation and polarization in relation to the spherical coordinate system are:

$$\hat{\mathbf{k}}_i = \cos\phi_i \sin\theta_i \hat{\mathbf{x}} + \sin\phi_i \sin\theta_i \hat{\mathbf{y}} + \cos\theta_i \hat{\mathbf{z}} \quad (3)$$

$$\hat{\mathbf{h}}_i = \frac{|\hat{\mathbf{z}} \times \hat{\mathbf{k}}_i|}{\hat{\mathbf{z}} \times \hat{\mathbf{k}}_i} = -\sin\phi_i \hat{\mathbf{x}} + \cos\phi_i \hat{\mathbf{y}} \quad (4)$$

$$\hat{\mathbf{v}}_i = \hat{\mathbf{h}}_i \times \hat{\mathbf{k}}_i = \cos\phi_i \cos\theta_i \hat{\mathbf{x}} + \sin\phi_i \cos\theta_i \hat{\mathbf{y}} - \sin\theta_i \hat{\mathbf{z}} \quad (5)$$

$$\hat{\mathbf{k}}_s = \cos\phi_s \sin\theta_s \hat{\mathbf{x}} + \sin\phi_s \sin\theta_s \hat{\mathbf{y}} + \cos\theta_s \hat{\mathbf{z}} \quad (6)$$

$$\hat{\mathbf{h}}_s = \frac{|\hat{\mathbf{z}} \times \hat{\mathbf{k}}_s|}{\hat{\mathbf{z}} \times \hat{\mathbf{k}}_s} = -\sin\phi_s \hat{\mathbf{x}} + \cos\phi_s \hat{\mathbf{y}} \quad (7)$$

$$\hat{\mathbf{v}}_s = \hat{\mathbf{h}}_s \times \hat{\mathbf{k}}_s = \cos\phi_s \cos\theta_s \hat{\mathbf{x}} + \sin\phi_s \cos\theta_s \hat{\mathbf{y}} - \sin\theta_s \hat{\mathbf{z}} \quad (8)$$

For bistatic calibration, the primary purpose of such a coordinate system is to eliminate the ambiguity in calling a wave H- or V-polarized.

2.3 Sources of Measurement Inaccuracy

The motivation for radar calibration is to minimize the effect of systemic errors on the measurement. When raw, uncalibrated data is taken, it includes undesirable information that must be filtered out before the data can have any value. There are several sources of this measurement inaccuracy.

2.3.1 Reflections from chamber walls and mounting apparatus

An indoor anechoic chamber is covered with radar-absorbing material (RAM) to minimize reflections from the transmitting antenna that would interfere with the scattered field from the object. RAM typically covers the walls of the chamber as well as the object-mounting pedestal. This usually reduces the magnitude of the reflection down to a reasonable level, but it is often desirable to reduce it further by means of *background subtraction* and *range gating*, but these methods introduce errors of their own. These methods are discussed in the next section.

2.3.2 Antenna coupling

At large bistatic angles, as the receiving antenna moves into the main beam of the transmitter, the incident field of the transmitter becomes much larger than the scattered field from the object, and it is difficult to subtract the two (Figure 5). There are two techniques for mitigating this error, discussed in the next section.

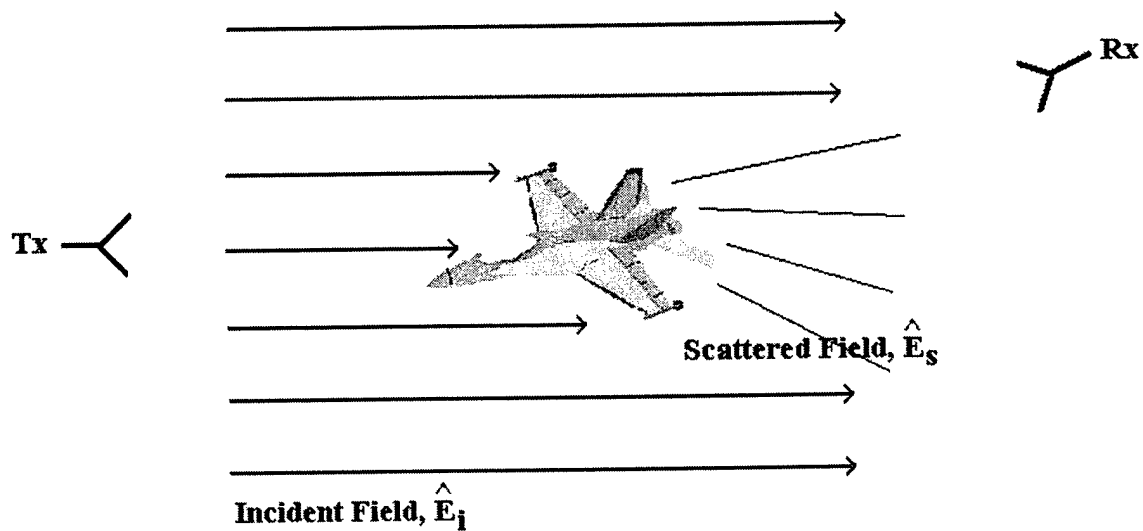


Figure 5: Antenna Coupling in Forward Scattering Region

2.3.3 Subsystem distortion

Subsystem distortion, or cross-polarization impurities occurring in the transmitter or receiver subsystems, can have a subtle yet significant affect on the accuracy of a polarimetric measurement, especially when considering *depolarizing objects*, or objects which scatter both polarizations with a single, linearly polarized incident wave. Due to hardware imperfections and/or the positioning of either antenna, antenna cross-polarization leakage is inevitable. This leakage can occur in either the transmitter or receiver, and often both. When a wave of a particular polarization is transmitted, the transmitted wave will have a small component of the opposite polarization. In the receiver, a particular antenna oriented to receive a single polarization may have a rotation that lets it receive some of the opposite polarization simultaneously.

2.3.4 Object alignment error

It can sometimes be very difficult to precisely align an object for measurement or calibration. A misalignment of an object will always produce a deviation from the theoretical behavior of the object, but some objects may be more sensitive to alignment error, and produce deviations that are much worse than another object. If the object is used for calibration, much care needs to be taken to choose an object that is not sensitive to alignment error, or a precise and sometimes complex alignment system is necessary.

A sphere, for instance, is completely insensitive to alignment error, because it has rotational symmetry about any axis. This makes it a popular calibration object. The radar return from a sphere, however, is relatively low, and the location of the noise floor of the measurements may preclude its use. *Louder* objects such as dihedrals and

trihedrals are often used in monostatic measurements, but these objects have a degree of alignment sensitivity that may introduce error into the measurement.

2.3.5 *Near-field effects*

Scattering behavior for an object is not the same in the near-field as it is in the far-field. A spherical wavefront does not illuminate a distributed object with a single phase. Scattering points along the object are illuminated at a phase dictated by their location relative to the axis defined by the direction of propagation. The object will scatter these various phases, and they will interfere, as in the far-field case; but this interference will obviously produce different patterns because the relative phase of each scattering point from a near-field excitation are different than that of a far-field excitation.

Simulating a planar wave front in an anechoic chamber is a major problem. Indoor ranges are limited in size, so parabolic reflectors are often used to distort the wave front to make it planar. Measurement chambers that use parabolic reflectors to create plane waves are called *compact ranges*.

2.4 **Range Gating and Background Subtraction**

Background subtraction is done by performing an *empty room* measurement: that is, a measurement with the object removed and the pedestal and antennas in exactly the same position. The empty room return is coherently subtracted from the measurement in order to isolate the object from its environment.

Two phenomena are often present in the background of RCS measurements that cannot be subtracted: first, interaction between the object and its pedestal, most often involving multipath reflections between the portion of the object facing the pedestal and

the more specular (flat) portions of the pedestal. Since this interaction is not possible with the object absent, it cannot be subtracted. Second, shadowing as a result of the object blocking the antenna's view of the pedestal can also be a problem. For objects with a large footprint on the pedestal, in the empty room measurement, the antenna sees a portion of the pedestal not seen in the measurement, which turns up in the time domain as a spurious return overlaid upon the object. Often this shadowing cannot be removed by range gating since the shadowed surface is many times very close to the object.

The next set of time-domain plots help to visualize the effects of the aforementioned error sources. Figure 6 is the calibrated RCS of a metallic sphere with and without background subtraction.

The vertical axis is the bistatic angle ($4 - 184$ degrees), the horizontal is the range (0 ns is the center of the chamber), and the color dimension is the RCS in dBsm. The feature labeled (1.) is the coupling between the Tx and Rx antennas. One can gain intuition into the reason for the arc-like shape of the coupling by visualizing the chamber with the Rx antenna in the forward scattering position. At the edge of the forward scatter region (around 150 degrees), the angular position of the receiver is offset from the equiphase plane of the incident wave. This means that the coupling that strikes the antenna at this point is from a more recent phase front, and the apparent location of the coupling at this angle would be closer to the Tx antenna. As the bistatic angle increases, the apparent location of the coupling grows closer to the pedestal, as the plane of the aperture of the Rx antenna moves perpendicular to the incident phase front. After background subtraction, feature 1 is greatly suppressed, but is still visible in the time-

domain plot. However, the level is around 20-30 dBsm lower than the return from the sphere.

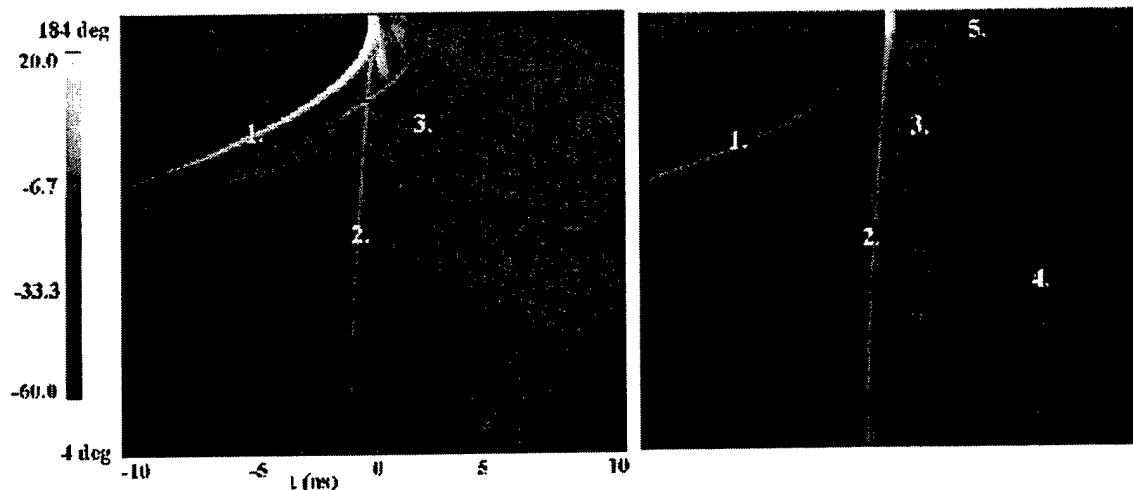


Figure 6: Time-Domain Sphere RCS (HH-pol) With Background Subtraction (right) and Without Subtraction (left)

The red vertical line labeled feature 2 is the RCS of the sphere itself. The line shifts somewhat as a function of bistatic angle, which is to be expected. In the backscatter direction (4 degrees) the specular point occurs at about -1 ns—closer to the Tx antenna. This is because the sphere is centered at 0 ns, and the specular point occurs at one radius-length behind the center. As the bistatic angle increases, the specular return moves as the specular point moves to the top of the sphere, and the creeping wave grows larger and interferes with the specular return. As expected, the forward scatter RCS of the sphere is quite large. This is not the energy radiated by the sphere in the forward direction, but the *absence of radiation*, or shadow of the sphere.

The phenomenon of shadowing can be seen in feature 3 of Figure 6. It is clear that this return is not part of the object return, since the return of the object is largely localized to the region between -1 and 0 ns. At near-monostatic angles, the receiver sees the same pedestal in the empty room measurement as it does with the object in place. As the

receiver moves past 90 degrees, the absence of the sphere reveals a portion of the pedestal that was shadowed; in this case it is the flat horizontal surface and the concave “cup” that the sphere rests on.

Feature 4 is a reflection within the transmission lines of the system. The return from the sphere enters the receiver, propagates along the coaxial cables to the network analyzer, and due to imperfect impedance matching in the system, it is attenuated, bounces back to the antenna, and bounces again back to the network analyzer and appears as a delayed and attenuated replica of the object.

Feature 5 is a by-product of the time-domain transform. To get a time-domain plot, an FFT is performed over the bandwidth of the measurement. Since the bandwidth is finite, a rippling occurs as a result of the transform, which gives rise to feature 5. This rippling occurs everywhere in the plot, but is most apparent at 184 degrees because the return is much larger at this angle.

Figure 7 shows the same calibrated and subtracted data after a range gate is applied with a width of 10 ns. In the vertical regions around the main object return the rippling due to the range gate is visible. Comparing this plot with Figure 6, one can see that the object/pedestal interaction is still present. It is possible and quite easy to make the range gate tight enough to eliminate this interaction, and still leave all of the object return, but the tighter range gate will make the rippling effects more prevalent. As it is, the data taken at the edge of the band (here, the data around 6 GHz and 14 GHz) is already unusable due to the range gate. If it is necessary to use these frequencies for analysis or for calibration, measurements must be done on a wider bandwidth.

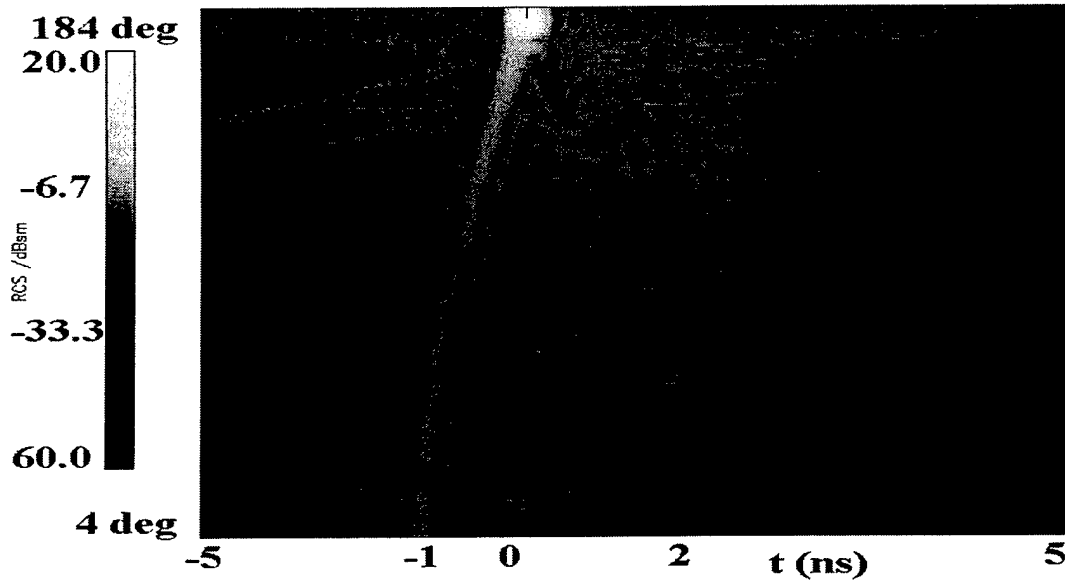


Figure 7: Time-Domain Sphere RCS (HH-pol) with 10 ns Range Gate Applied

2.5 Types and Applicability of Calibration

For a given measurement, there is more than one type of calibration that can be used. The determination of the calibration type will be dependent on the quality of the measurement facility, the measurement conditions, and the degree of accuracy that is required. Radar calibration can be of three basic types:

- Amplitude and phase (Type-1)
- Simple polarimetric (Type-2)
- Full Polarimetric (Type-3)

2.5.1 Amplitude and phase (Type-1) calibration

A Type-1 calibration applies a complex constant scale factor to each scattering matrix. The scale factor is usually calculated by measuring an object with a known RCS and phase center, and comparing the ratio of the measured and *exact* responses. Type-1 calibrations all have a common form. For each polarization channel (HH, VH, HV, and VV), the calibrated RCS is:

$$\sigma_{cal} = \frac{\sigma_{tar} - \sigma_{tar,bkg}}{\sigma_{cal_tar} - \sigma_{cal_tar,bkg}} \sigma_{cal_tar,theoretical} \quad (9)$$

where σ_{cal} is the calibrated response of the object. The calibrated scattering matrix takes the form of:

$$\mathbf{S}_{cal} = \begin{bmatrix} \sigma_{cal,HH} & \sigma_{cal,VH} \\ \sigma_{cal,HV} & \sigma_{cal,VV} \end{bmatrix} \quad (10)$$

where S_{cal} is the calibrated scattering matrix of the unknown object and the σ 's correspond to the amplitudes and phases of their corresponding polarizations.

The advantage of using a Type-1 calibration technique is in its simplicity. Only one calibration reference object is necessary and it is computationally very simple to implement. The disadvantages of using only a Type-1 technique, however, are numerous. An object must be selected that has high RCS for every polarization, in order for the calibration to be accurate for the complete scattering matrix. Often, however, a Type-1 technique is used only to calibrate co-polar channels. It is practical to perform a Type-1 calibration with more than one reference object, but at this point the technique is not much more efficient than a Type-2 or 3 technique. In addition, a Type-1 technique does not account for distortion occurring in the transmitter and receiver subsystems.

2.5.2 Simple polarimetric (Type-2) calibration

In order to account for system distortion, a Type-2 or 3 calibration technique is usually employed. The Type-2 calibration technique, or *simple polarimetric calibration*, accounts for zero-order antennae polarization distortion effects. Each of the co-polarized subsystem distortion terms, R_{HH} , T_{HH} , R_{VV} , T_{VV} , cannot be determined distinctly, but can

be found as products of the receiver subsystem distortion (**R**) and transmitter subsystem distortion (**T**) for each polarization channel combination. The distortion terms are expressed as a 4x4 complete system distortion matrix, **C** is introduced, which carries the same information as the 2x2 matrices **R** and **T**. The **C** matrix has the form:

$$\mathbf{C} \equiv \begin{bmatrix} R_{HH}T_{HH} & R_{HV}T_{HH} & R_{HH}T_{VH} & R_{HV}T_{VH} \\ R_{VH}T_{HH} & R_{VV}T_{HH} & R_{VH}T_{VH} & R_{VV}T_{VH} \\ R_{HV}T_{HH} & R_{HV}T_{HV} & R_{HH}T_{VV} & R_{HV}T_{VV} \\ R_{VV}T_{HH} & R_{VV}T_{HV} & R_{VH}T_{VV} & R_{VV}T_{VV} \end{bmatrix} \quad (\text{Mortensen, 1995})$$

where the elements R_{**} and T_{**} correspond directly to the elements of the **R** and **T** matrices mentioned earlier. For a simple polarimetric calibration, only the elements lying on the diagonal of **C** (analogous to the products of the elements lying on the diagonals of **R** and **T**) are calculated. Thus the form of the **C** matrix for a simple polarimetric calibration is:

$$\mathbf{C} = \begin{bmatrix} R_{HH}T_{HH} & 0 & 0 & 0 \\ 0 & R_{VV}T_{HH} & 0 & 0 \\ 0 & 0 & R_{HH}T_{VV} & 0 \\ 0 & 0 & 0 & R_{VV}T_{VV} \end{bmatrix} \quad (11)$$

All other terms correspond to cross-polarization impurity of the subsystems, the calculation of which requires a full-polarimetric calibration (Type-3). It is important to note that, though a Type-2 calibration solves for the products of the **R** and **T** coefficients, this calibration can give no information about **R** and **T** separately, so the combined matrix (**C**) must be used instead.

A Type-2 calibration will require a minimum of two calibration objects: a single reference calibration object, for which the theoretical solution is precisely known, and an

additional depolarizing object for cross-polarization correction, also with a known scattering matrix.

2.5.3 Fully polarimetric (Type-3) calibration

A fully polarimetric calibration is able to solve for all eight coefficients of the **R** and **T** matrices (and thereby all 16 terms of the **C** matrix). The first and second order subsystem distortion effects are all accounted for, including the cross-polarization impurity of the individual transmit and receive antennas.

The Type-3 technique is the best available for accuracy in calibration, at the cost of complexity. A fully polarimetric technique requires three calibration objects whose theoretical scattering matrices are precisely known (Whitt, et al, 1991). By definition, a fully polarimetric technique must solve for the coefficients of the distortion matrices separately, as opposed to a Type-2 technique. This neglects the dependent nature of each distortion term on another. A rigorous mathematical process is necessary in order to solve for the subsystem distortion matrices simultaneously. Once the distortion matrices are computed, the corrected scattering matrix for an unknown object is given by:

$$\mathbf{S} = \mathbf{R}^{-1}\mathbf{M}\mathbf{T}^{-1} \quad (12)$$

Where **S** is the corrected scattering matrix and **M** is the measured matrix, with background subtraction performed. This relationship can be derived from equation (2) by re-arranging terms under the assumption that the subsystem distortion matrices are invertible (Ulaby and Elachi, 1990). A technique of this type requires a minimum of three calibration reference objects with known scattering matrices.

3 BISTATIC CALIBRATION METHODS

Several existing calibration methods were sampled, for the reasons listed above, and they are listed in this section.

3.1 Basic Type-1 Calibration

This technique is not documented in the literature, but it is essentially the only way one would perform a Type-1 calibration. An object is selected which has zero or negligible cross-polarization return (a sphere or circular disk, for example). The calibrated measurement values for each polarization (HH and VV) are computed by Eqn (9).

3.2 EMSL Simple Polarimetric Calibration

This is the bistatic calibration method (Type-2) currently used in the EMSL (Mortensen, 1995). A circular disk is used for the reference object. This object provides a high specular RCS and well-defined phase center, as well as an accurate theoretical prediction by Physical Optics, although the disk is somewhat difficult to align in the quasi-monostatic configuration. The reference object is used to solve for the (1,1) and (4,4) elements of the \mathbf{C} matrix, or the coefficients $R_{HH}T_{HH}$ and $R_{VV}T_{VV}$. The (2,2) and (3,3) elements of the matrix are computed first by correcting the amplitudes of the depolarizing object with the (1,1) and (4,4) coefficients already found, and computing the ratio of the measured cross-polar amplitude to the absolute corrected amplitude. The PO approximation for the backscatter RCS of the disk, assuming a perfectly conducting surface is (in dB),

$$\mathbf{S}_{\text{disk}} = 20 * \log_{10} \left(\frac{i2(\pi)^{3/2} r^2}{\lambda} \right) \begin{bmatrix} 1 & 0 \\ 0 & 1 \end{bmatrix} = \begin{bmatrix} S_{\text{disk}}^{HH} & 0 \\ 0 & S_{\text{disk}}^{VV} \end{bmatrix} \quad (13)$$

where r is the radius of the sphere in meters, and λ is the wavelength in meters. For matrix multiplication by a 4x4 matrix, the normal 2x2 scattering matrix format is modified to a 4x1 vector of the form:

$$\mathbf{S}_{\text{disk}} = \begin{bmatrix} S_{\text{disk}}^{HH} \\ 0 \\ 0 \\ S_{\text{disk}}^{VV} \end{bmatrix} \quad (14)$$

The elements $C_{1,1}$ and $C_{4,4}$ are solved by relating the measured scattering matrix of the disk (\mathbf{M}_{disk}) to the theoretical prediction:

$$\mathbf{M}_{\text{disk}}^{HH} = C^{1,1} S_{\text{disk}}^{HH} + C^{1,2} S_{\text{disk}}^{VH} + C^{1,3} S_{\text{disk}}^{HV} + C^{1,4} S_{\text{disk}}^{VV} \quad (15)$$

$$\mathbf{M}_{\text{disk}}^{VV} = C^{4,1} S_{\text{disk}}^{HH} + C^{4,2} S_{\text{disk}}^{VH} + C^{4,3} S_{\text{disk}}^{HV} + C^{4,4} S_{\text{disk}}^{VV} \quad (16)$$

For the circular disk, the cross-polarized elements are approximately zero, and we assume that the elements due to the cross-talk in the system, $C^{1,4}$ and $C^{4,1}$, are negligible so the equation simplifies to:

$$M_{\text{disk}}^{HH} = C^{1,1} S_{\text{disk}}^{HH} \quad (17)$$

$$M_{\text{disk}}^{VV} = C^{4,4} S_{\text{disk}}^{VV} \quad (18)$$

We can now rearrange this formula to solve for $C^{1,1}$ and $C^{4,4}$ and use these coefficients to find the corrected amplitude of the depolarizing object. This allows us to use the wire mesh as a calibration object without knowing its exact RCS. The EMSL uses a mesh of parallel wires as a depolarizer. Two measurements are made on the mesh: one in the vertical orientation, and one with the mesh tilted 45 degrees from vertical in

the counter-clockwise direction. In the vertical orientation, it is reasonable to assume that only the VV-polarized wave will be reflected, and all others will be transmitted through the mesh, giving the 4x1 scattering vector the form

$$\mathbf{S}_{\text{mesh,vert}} = S_{\text{mesh}} \begin{bmatrix} 0 \\ 0 \\ 0 \\ 1 \end{bmatrix} \cos^2\left(\frac{\theta}{2}\right) = \begin{bmatrix} 0 \\ 0 \\ 0 \\ S_{\text{mesh,vert}}^{VV} \end{bmatrix} \quad (19)$$

In the tilted configuration, the vector takes the form

$$\mathbf{S}_{\text{mesh,tilt}} = \frac{S_{\text{mesh}}}{2} \begin{bmatrix} 1 \\ -\cos\left(\frac{\theta}{2}\right) \\ -\cos\left(\frac{\theta}{2}\right) \\ \cos^2\left(\frac{\theta}{2}\right) \end{bmatrix} = \begin{bmatrix} S_{\text{mesh,tilt}}^{HH} \\ S_{\text{mesh,tilt}}^{VH} \\ S_{\text{mesh,tilt}}^{HV} \\ S_{\text{mesh,tilt}}^{VV} \end{bmatrix} \quad (20)$$

where θ is the bistatic angle. This approximation is valid for small bistatic angles (Bicci, 1992). In the tilted orientation, the amplitude of the monostatic ($\theta = 0$) RCS of the mesh should be the same for all polarizations. The cosine dependence of the VH, HV, and VV polarizations can be seen intuitively by visualizing the measurement geometry. In the EMSL, the receiver tracks in the vertical direction and therefore over the object (the tilted wire mesh, for instance) rather than around it in azimuth. As the receiver moves, the V-polarized component of the wave that is transmitted is not completely V-polarized from the receiver's perspective. This polarization distortion at the receiver is expressed mathematically as a loss in the V-polarized RCS as a function of the bistatic angle.

To find the corrected values of the mesh in the vertical orientation, we simply divide the VV-component (the only component that is non-zero) of the measurement by the element of \mathbf{C} corresponding to VV-pol, $C^{4,4}$:

$$S_{mesh,vert}^{VV} = \frac{M_{mesh,vert}^{VV}}{C^{4,4}} \quad (21)$$

From the corrected magnitude of $S_{mesh,vert}$, we can find the corrected monostatic RCS of the vertical mesh, S_{mesh} :

$$S_{mesh} = \frac{S_{mesh,vert}^{VV}}{\cos^2(\frac{\theta}{2})} \quad (22)$$

Substituting equation (22) into equation (20), and selecting the HV and VH polarizations, we get

$$S_{mesh,tilt}^{VH} = -\frac{S_{mesh,vert}^{VV}}{2\cos(\frac{\theta}{2})} \quad (23)$$

$$S_{mesh,tilt}^{VH} = S_{mesh,tilt}^{HV} \quad (24)$$

And this is all the information we need to solve for the remaining coefficients of the diagonal \mathbf{C} matrix:

$$C^{2,2} = \frac{M_{mesh,tilt}^{VH}}{S_{mesh,tilt}^{VH}} \quad (25)$$

$$C^{3,3} = \frac{M_{mesh,tilt}^{HV}}{S_{mesh,tilt}^{HV}} \quad (26)$$

After the four calibration coefficients have been computed, the calibration can be performed for a single frequency by a simple matrix multiplication:

$$\mathbf{S} = \mathbf{C}^{-1}(\mathbf{M} - \mathbf{B}) \quad (27)$$

Where \mathbf{S} is the calibrated scattering matrix, \mathbf{M} is the measured scattering matrix, and \mathbf{B} is the scattering matrix of the background.

3.3 Generalized Dual-Antenna Calibration

This technique, proposed in (Whitt, et al, 1991) and elaborated in (Ulaby and Elachi, 1990), is the most general technique available in current literature. Its advantage is that it makes few assumptions about the form of the scattering matrix of each object. It requires that one of the scattering matrices must be invertible, and assumes that the scattering matrices are all symmetric (cross-polarized components are equal). This is a good assumption for any passive object in the monostatic or quasi-monostatic configurations, but is not always true for bistatic measurements, in general. Therefore this assumption practically limits the use of the technique to dual-antenna systems calibrated in the quasi-monostatic configuration.

The main limitation of the technique is the requirement that the theoretical RCS of each of the three reference objects be exactly known. In addition, the technique is much more mathematically complex than other calibration techniques, but this obviously has no effect on the ease of implementation of the technique once the mathematical routine is successfully implemented.

The technique is able to account for all eight error terms included in the matrix formula of equation (2) but the notation includes a complex scale factor ($ce^{i\phi}$) so that the relationship between the measured scattering matrix (**M**) and the theoretical matrix (**S**) expands to:

$$\mathbf{M} = ce^{i\phi} \mathbf{RST} \quad (28)$$

The technique requires three reference objects, and exact theoretical predictions for each, producing three similar equations:

$$\mathbf{M}_j = c e^{i\phi_j} \mathbf{R} \mathbf{S}_j \mathbf{T}, j = 1, 2, 3 \quad (29)$$

The real constant, c , will be the same for each object, as it is a characteristic of the radar. The phase constant (ϕ_j) is subscripted to allow for the phase centers of each object to differ, thus eliminating the need to place the objects such that their phase centers all coincide. We must solve for the unknowns \mathbf{R} , \mathbf{T} , c , and ϕ_j . Following the procedure of Ulaby and Elachi, the steps are described in the following pages.

We first assume that one of the calibration reference objects has an invertible scattering matrix. For the purposes of this derivation we assume that matrix to be the object corresponding to $j = 1$. We first define the similarity transformations:

$$\mathbf{N}_T = e^{i(\phi_1 - \phi_2)} \mathbf{T}^{-1} \mathbf{P}_T \mathbf{T} \quad (30)$$

$$\underline{\mathbf{N}}_T = e^{i(\phi_1 - \phi_2)} \mathbf{T}^{-1} \underline{\mathbf{P}}_T \mathbf{T} \quad (31)$$

Where $\mathbf{N}_T = \mathbf{M}_1^{-1} \mathbf{M}_2$, $\underline{\mathbf{N}}_T = \mathbf{M}_1^{-1} \mathbf{M}_3$, $\mathbf{P}_T = \mathbf{P}_1^{-1} \mathbf{P}_2$, and $\underline{\mathbf{P}}_T = \mathbf{P}_1^{-1} \mathbf{P}_3$.

It is now necessary to express the above matrices \mathbf{P}_T and \mathbf{N}_T in terms of their eigenvectors and eigenvalues.

$$\mathbf{P}_T \mathbf{X}_T = \mathbf{X}_T \mathbf{\Lambda}'_T \quad (32)$$

$$\mathbf{N}_T \mathbf{Y}_T = \mathbf{Y}_T \mathbf{\Lambda}_T \quad (33)$$

the eigenvalues and eigenvectors are related by

$$\mathbf{\Lambda}'_T = \mathbf{\Lambda}_T e^{i(\phi_1 - \phi_2)} \quad (34)$$

$$\mathbf{Y}_T = \mathbf{T}^{-1} \mathbf{X}_T \quad (35)$$

The matrices \mathbf{X}_T and \mathbf{Y}_T are defined as 2x2 matrices, the columns of which are the eigenvectors of \mathbf{P}_T and \mathbf{N}_T , respectively. $\mathbf{\Lambda}'_T$ and $\mathbf{\Lambda}_T$, respectively, are diagonal matrices of the eigenvalues. Using the equation (35) and manipulating the matrices to solve for the transmitter subsystem distortion matrix, \mathbf{T} , and introducing an multiplicative scale factor to account for the arbitrary constant that cannot be solved for in the above equations, we arrive at the expression of equation (36):

$$\mathbf{T} = \mathbf{X}_T \mathbf{C} \mathbf{Y}_T^{-1} \quad (36)$$

The matrix \mathbf{C} is a diagonal matrix of real constants (c_1 and c_2). We can now define a new set of equations,

$$\mathbf{P}_T \mathbf{X}_T = \mathbf{X}_T \mathbf{\Lambda}'_T \quad (37)$$

$$\mathbf{N}_T \mathbf{Y}_T = \mathbf{Y}_T \mathbf{\Lambda}_T \quad (38)$$

and then say that

$$\mathbf{T} = \mathbf{X}_T \mathbf{C} \mathbf{Y}_T^{-1} \quad (39)$$

Again, \mathbf{C} is a diagonal matrix of constants (\underline{c}_1 and \underline{c}_2). Understanding that the \mathbf{T} of equation (36) and of equation (39) are identical, we now have enough information to solve for the arbitrary constants c_1 and c_2 (as well as \underline{c}_1 and \underline{c}_2 , however we only need one set of constants). Through a process of solving the above matrix equations in terms of sets of scalar equations, we find the constants to be:

$$c_1 = \Delta(\mathbf{Y}_T) (x_{11}y_{22} - \frac{c_2}{c_1} x_{12}y_{21})^{-1} \quad (40)$$

$$c_2 = \Delta(\mathbf{Y}_T) \left(\frac{c_1}{c_2} x_{11} y_{22} - x_{12} y_{21} \right)^{-1} \quad (41)$$

where the scalars x_{**} and y_{**} are the corresponding elements of the matrices \mathbf{X}_T and \mathbf{Y}_T . After substituting the right side of equations (40) and (41) into the matrix \mathbf{C} in equation (36), we now have a unique value for the transmitter subsystem distortion matrix.

The receiver subsystem distortion matrix is solved for in an identical matter. First the similarity transformations of equations (42) and (43) are created,

$$\mathbf{N}_R = e^{i(\phi_2 - \phi_1)} \mathbf{T}^{-1} \mathbf{P}_R \mathbf{T} \quad (42)$$

$$\underline{\mathbf{N}}_R = e^{i(\phi_3 - \phi_1)} \mathbf{T}^{-1} \underline{\mathbf{P}}_R \mathbf{T} \quad (43)$$

Where $\mathbf{N}_R = \mathbf{M}_2 \mathbf{M}_1^{-1}$, $\underline{\mathbf{N}}_R = \mathbf{M}_3 \mathbf{M}_1^{-1}$, $\mathbf{P}_R = \mathbf{P}_2 \mathbf{P}_1^{-1}$, and $\underline{\mathbf{P}}_R = \mathbf{P}_3 \mathbf{P}_1^{-1}$.

By subsequently expressing the \mathbf{N} and \mathbf{P} matrices of (42) and (43) in terms of eigenvectors and eigenvalues, as in (37) and (38), we can specify the matrix \mathbf{R} . The constant amplitude and phase factors included in equation (29), however, remain unknown. The amplitude factor c can be solved for by substituting the known \mathbf{R} and \mathbf{T} matrices back into equation (28), and solving for c :

$$|c| = \frac{|(\mathbf{N}_j)_{mn}|}{|(\mathbf{R} \mathbf{P}_j \mathbf{T})_{mn}|} \quad (44)$$

The matrix \mathbf{P}_j should be selected such that it is the most accurate of the three, thereby giving a more accurate estimation of c . The mn^{th} elements of the matrices should probably be selected to correspond to one of the co-polar channels (HH or VV), since

they are in general larger in magnitude, and therefore are less affected by noise. The absolute phase factor (ϕ') is given by:

$$\phi' = \phi + \tan^{-1}\left(\frac{\text{Im}\{c\}}{\text{Re}\{c\}}\right) \quad (45)$$

Where the unknown constant ϕ represents the phase represented by the propagation distance between the antenna and object.

Finally, the calibrated scattering matrix of an unknown object (\mathbf{P}^u) can be found from the measured scattering matrix (\mathbf{N}^u) by the expression:

$$\mathbf{P}^u = e^{-i\phi'} \frac{1}{|c|} \mathbf{R}^{-1} \mathbf{N}^u \mathbf{T}^{-1} \quad (46)$$

3.4 Bistatic via Monostatic Calibration

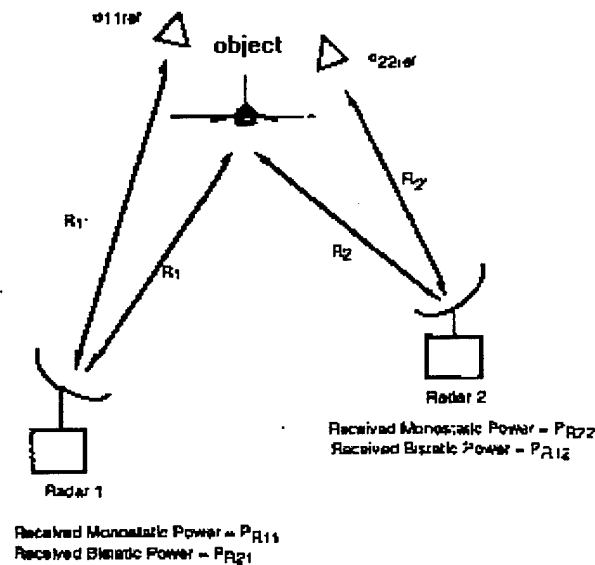


Figure 8: BICOMS Calibration Geometry (Alexander, et al, 1995)

Used by the Bistatic Coherent Measurement System (BICOMS) at Holloman AFB, NM, this Type-3 calibration technique utilized the calibration procedure described in

(Whitt, et al, 1991). This procedure is designed around the unique measurement conditions of this facility. Initially, each monostatic leg of the bistatic path is calibrated separately, as illustrated in Figure 8. The normalized full-polarimetric distortion matrices (PDM's), \mathbf{R} and \mathbf{T} , are solved for in each case, exactly as outlined in Section 3.3, yielding the relationship stated in equation (28) for each monostatic leg. This process gives four matrices; a receiver PDM and a transmitter PDM for each of the two antennas as follows:

$$\mathbf{R}_1 = \begin{bmatrix} 1 & r_{vh} \\ r_{hv} & r_{vv} \end{bmatrix} \quad \mathbf{T}_1 = \begin{bmatrix} 1 & t_{vh} \\ t_{hv} & t_{vv} \end{bmatrix} \quad (47)$$

$$\mathbf{R}_2 = \begin{bmatrix} 1 & r_{vh} \\ r_{hv} & r_{vv} \end{bmatrix} \quad \mathbf{T}_2 = \begin{bmatrix} 1 & t_{vh} \\ t_{hv} & t_{vv} \end{bmatrix} \quad (48)$$

where $r_{pq} = r'_{pq}/r'_{hh}$, and $t_{pq} = t'_{pq}/t'_{hh}$ (Tuley, 1995). The above equations need only solve for the PDMs within a complex constant, the exact scattering solutions for the three monostatic reference objects offers no useful information, since the amplitude and phase constant for the bistatic path cannot be found from the monostatic path. The advantage of this technique is realized when objects are selected such that the *structure* of the scattering matrix is well known, but the precise solution is not. For instance, the theoretical scattering matrix that would be input to the procedure for a sphere, a dihedral oriented vertically, and a trihedral would be

$$\mathbf{S}_{\text{sphere}} = \begin{bmatrix} 1 & 0 \\ 0 & 1 \end{bmatrix} \quad \mathbf{S}_{\text{vertical,dihedral}} = \begin{bmatrix} 0 & 0 \\ 0 & 1 \end{bmatrix} \quad \mathbf{S}_{\text{tilted,dihedral}} = \begin{bmatrix} -1 & -1 \\ -1 & 1 \end{bmatrix} \quad (49)$$

for every frequency.

At this point the necessary PDMs for each bistatic path are known, relative to the gain of the VV channel. A separate calibration compensation step is performed on the bistatic leg to solve for the constant amplitude and phase factor. An object is measured which has a known VV-polarized return; in the case of the BICOMS calibration method, the end-cap of a large squat cylinder is used to determine the phase factor, and the same cylinder is measured to determine the amplitude factor, but rotated such that the curved surface is oriented forming a peak specular return along the bistatic path. The PO solution for a circular disk is used as a theoretical prediction for the end-cap cylinder. The ratio of the theoretical and measured amplitudes of the cylinder's curved surface, and the difference of the theoretical and measured phases for the end-cap cylinder provide the necessary constants c and ϕ for the VV channel,

$$c = \frac{|M_{vv,cylinder}|}{|S_{vv,cylinder}|} \quad \phi = \frac{\angle M_{vv,end-cap}}{\angle S_{vv,end-cap}} \quad (50)$$

and as such there exists an absolute PDM for each antenna subsystem.

This technique, while providing a way to perform the general Type-3 calibration technique without a precise theoretical prediction for the three monostatic reference objects, has the disadvantage that it requires additional objects to compensate for absolute amplitude and phase. For an RCS measurement facility such as BICOMS, this is a significant deficiency; it requires more time in mounting the additional objects, and system drift and environmental considerations will tend to degrade the performance of the calibration over that time.

4 METHODOLOGY

4.1 Purpose

Since the purpose of this work is primarily to assess the performance of several existing and proven bistatic calibration techniques the techniques are evaluated on the basis of the factors listed in Section 1. Again, they are:

- Sensitivity of calibration to reference object alignment error
- Sensitivity to antenna polarization impurity
- Robustness and repeatability of the technique
- Applicability to fixed-bistatic or true bistatic measurements
- Ease and efficiency of implementation
- Sensitivity to the condition of the reference object scattering matrix

These are the major concerns for the accuracy and efficiency of a given calibration technique. Of course, given the wide variance in measurement conditions from one measurement range to another, a particular calibration technique that is optimal for one range may be unreasonable for another. It is for this reason that calibration techniques that have been or are being used in a wide variety of measurement facilities and scenarios are evaluated.

In addition to evaluating these techniques, another goal of this research is to provide documentation of the specific problems and benefits of using a particular calibration object. Many concerns, such as:

- Ability to produce precise theoretical predictions for the object
- Alignment sensitivity of the object
- Object signal-to-noise ratio

- Other electromagnetic scattering characteristics of the object

are all important information in selecting an object that will yield a precise calibration. A reference calibration object, for instance, nearly always requires a precise calculation of the *exact* RCS amplitude and phase. Reference objects that are more complex than the canonical set of spheres, disks, or small cylinders, require computationally intense Moment Method simulations, which sometimes are impractical, depending on the complexity and electrical size of the object.

Objects such as disks and long cylinders, though often easy to calculate a prediction, tend to be very sensitive to alignment errors. It is desired that reference objects be selected such that they are rather insensitive to alignment, because the precise alignment of an object is often tedious and time-consuming, and also tends to necessitate object pedestals that are large and interact more with the object.

Objects must also be chosen so that the level of their RCS is high enough to be significantly above the noise and clutter. For calibration at a generic bistatic angle, few objects are known which have a relatively constant RCS for all bistatic angles.

Other scattering phenomenon, such as creeping waves, can also adversely affect the suitability of a reference object. If an object is chosen with a large creeping wave component, the phase of the RCS will not be a suitable reference for the range focus. In addition, any surface wave on the object could be retarded when it comes in contact with the pedestal, which would create a deviation in the measurement from the theoretical prediction.

4.2 Resources Required

In order for the factors listed in Section 4.1 to be properly evaluated, the work was performed in a facility which:

- Has the capability of precisely aligning the reference objects
- Has very good antenna polarization purity (at least 30 dB)
- Measurements in the facility are highly repeatable, necessitating a large signal-to-noise ratio
- Has the capability to perform fixed-bistatic or true bistatic measurements
- Is relatively easy to mount objects and configure the system
- Has the capability to perform measurements on a wide variety of objects

The European Microwave Signature Laboratory (EMSL) was chosen because it fits most of these criteria, excepting that the signal-to-noise ratio is less than desirable unless large integration is used. An auxiliary facility is also available for the duplication of the EMSL measurements at the bistatic RCS lab of the Air Force Institute of Technology (AFIT) at Wright-Patterson Air Force Base, Ohio. This facility does not have the capability to collect full-polarimetric data, nor does it have the degree of accuracy like to the EMSL. These factors, among others, make the difference between the facilities sufficient enough to justify its use in extending the applicability of these calibrations to a different measurement environment.

As well as an accurate and versatile measurement facility, it is also necessary to have expertise available in computational scattering and RCS measurements. The theoretical predictions for each of the test objects are a major portion of the project. Expertise in the Method of Moments, as well as Physical Optics and the Uniform Geometrical Theory of Diffraction was necessary in order to obtain all the theoretical

predictions that are required. The proposed object test matrix is varied enough such that all three techniques are required.

Experience in the modeling of electromagnetic scattering as well as RCS measurements are available at the Technologies for Detection and Positioning (TDP) unit of the Space Applications Institute (SAI) at JRC as well as AFIT.

Not least of all the requirements for this project was time. Collecting the raw data for the calibration test objects took many weeks of continuous measurement. The availability of range time in the EMSL was maximal.

4.3 Approach

4.3.1 Assessment of Air Force-wide calibration needs

The concern of the Air Force in the field of bistatic calibration lies naturally in its applicability to bistatic RCS measurement facilities currently in use by the USAF. Facilities currently in use or in development and are the major concern of this work include the Bistatic Coherent Measurement System (BICOMS) at NRTF/RATSCAT at Holloman AFB, NM, the dual compact range under construction at AFRL/SNHE at Hanscom AFB, MA, and the RCS laboratory at the Air Force Institute of Technology (AFIT) at Wright-Patterson AFB, OH. None of these facilities are suitable for a thorough study of calibration involving the specific concerns of each range, so another, more versatile facility is needed to complete the measurements, namely the EMSL. To sum up some of the main concerns for the calibration of bistatic radar systems, the following are of considerable importance:

- Number of calibration object mounts required
- Length of time to perform calibration
- Ability of calibration to account for 1st and 2nd order cross-talk effects (full-polarimetric calibration)
- Ease and practicality of producing theoretical predictions for reference objects

A large part of the solution to these problems lies in the careful selection of the calibration reference objects.

4.3.2 Calibration object selection

There is a range of objects that have been accepted as a canonical set for calibration. Monostatic and bistatic calibration objects are often similar, but there are objects that are used for monostatic calibration that are not suitable in a bistatic scenario. Some popular objects for monostatic calibration are trihedrals, dihedrals, disks and plates, spheres, and cylinders. All objects are usually metallic with a brushed or polished finish. For bistatic calibration, trihedrals are not suitable, and dihedrals, though in some cases practical, are not as useful as in monostatic. Disks, plates, and cylinders make good calibration objects at small bistatic angles, with varying degrees of alignment sensitivity among the three. Due to their complete insensitivity to alignment, and the available exact analytic solution (the Mie Series), the sphere is a universally good calibration object, though the problem of low RCS at any given bistatic angle is an ever-present problem. Though not considered a *canonical* object, the wire mesh has also proven to be a good object for polarimetric calibration, and as a result this object is included in the analysis.

A set of calibration objects was chosen based on their use in bistatic ranges of Air Force interest, and additional non-canonical objects were chosen for comparison. The bistatic measurements were performed, in general, at a relatively small bistatic angle, in

hopes that for some objects, the ease and efficiency of a monostatic calibration can be extended to a bistatic calibration at a small bistatic angle. Table 1 lists the objects that were tested.

Table 1: Test Matrix

<i>Object</i>	<i>Orientation</i>	<i>Measurement Type</i>
Metallic sphere		swept bistatic monostatic
long cylinder	d = 50 mm, h = 200 mm axis parallel to x-axis axis 45 deg from horizontal axis 45 deg from horizontal axis 67.5 deg from horizontal axis 67.5 deg from horizontal	swept bistatic bistatic: 4.6 deg monostatic bistatic: 4.6 deg monostatic
Squat cylinder	d = 215 mm, h = 108 mm axis parallel to x-axis axis 45 deg from horizontal axis 45 deg from horizontal axis 22.5 deg from horizontal axis 22.5 deg from horizontal	swept bistatic bistatic: 4.6 deg monostatic bistatic: 4.6 deg monostatic
Dihedral	one face: l=300 mm, w=150 mm Seam oriented vertical Seam oriented vertical Seam 45 deg from vertical Seam 45 deg from vertical Seam 22.5 deg from vertical Seam 22.5 deg from vertical	bistatic: 4.6 deg monostatic bistatic: 4.6 deg monostatic bistatic: 4.6 deg monostatic
Circular disk	20 cm diameter Specular orientation Specular orientation	bistatic: 4.6 deg monostatic
wire mesh	19 cm x 20 cm (19 20-cm wires spaced 1 cm apart) Wires oriented vertically Tilted 45 deg counter-clockwise Wires oriented vertically Tilted 45 deg counter-clockwise	bistatic: 4.6 deg monostatic bistatic: 4.6 deg monostatic
Trihedral	one face: a=102 mm, c=145 mm Specular orientation	monostatic

For each object and orientation listed in the test matrix, measurements were performed for each of the two Tx/Rx combinations, and all were fully polarimetric; i.e. HH, VH, HV, and VV pol were all collected.

4.3.3 Experimental validation of measurement facility

In order for a valid study of calibration to be done, the idiosyncrasies of the measurement facilities must be first understood. The design of the chamber is the most important factor to consider. Many experimental facilities are designed with a specific purpose in mind. In most cases, an RCS measurement facility is designed around a specific object or set of objects to be measured. The BICOMS system at Holloman AFB, NM, for instance, was designed for full-scale polarimetric measurements of aircraft (Alexander, et al.). The calibration considerations, namely the time necessary to perform the calibration, for a range such as this, are sometimes much different than those of an indoor chamber. Other indoor chambers have very different design specifications, as well. Section 4.4 contains a discussion of the design of the EMSL and its capabilities for this study.

4.3.4 Validation of measurements via computational methods

To ensure that the data taken from the EMSL are reliable, a simple validation was performed on the measurement of the circular disk. The PO solution for the backscattering from a metallic disk is given above in Equation (13). The quasi-monostatic measurement of the disk was calibrated using the EMSL simple polarimetric technique, and compared against the PO prediction. As seen in Figure 9, the RCS error is well within 1 dB, but the calibrated phase shows a marked difference in slope and initial

phase. This is due to the fact that the disk was not located at exactly the phase center defined by the calibration. The deviation here shows a difference in position of about $\frac{1}{2}$ cm (for an approximate phase difference of 50° at 10 GHz).

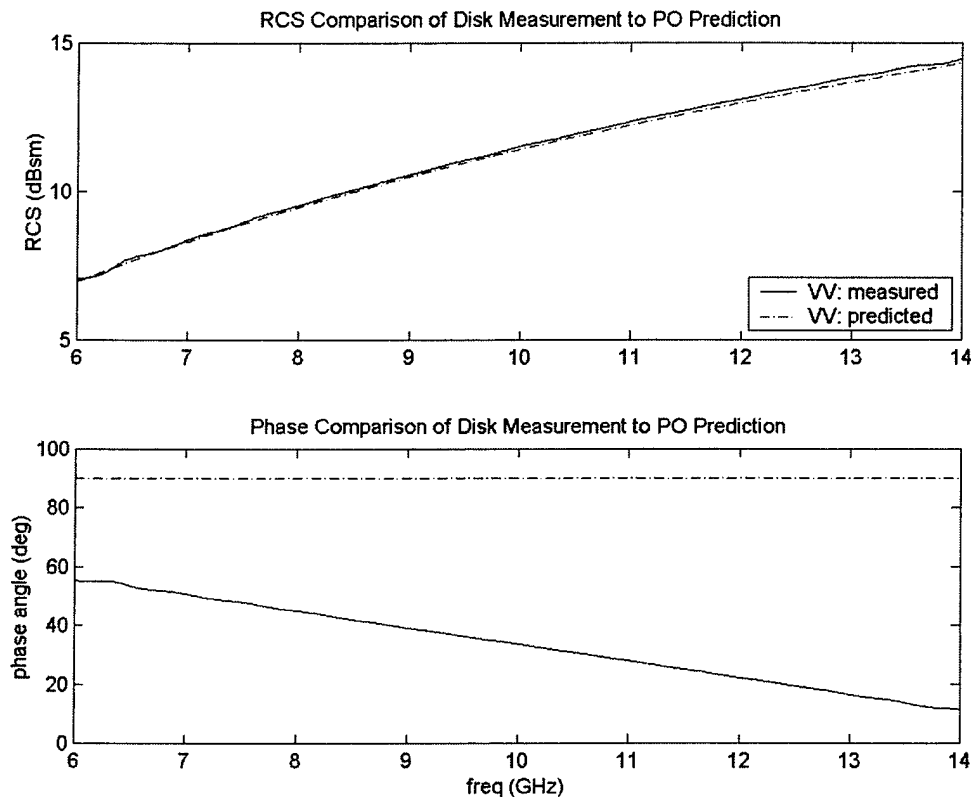


Figure 9: Validation of VV-pol Measurement in EMSL.

4.3.5 Implementation of calibration techniques

All of the calibration techniques listed in Section 4 were implemented as MATLAB functions, which are listed in Appendix B.

4.4 Characterization of the EMSL

Before performing the measurements on the calibration test objects, the EMSL was thoroughly evaluated for its performance of the criteria listed in Section 4.2.

4.4.1 Design of the EMSL

The EMSL was designed as a versatile radar signature measurement facility, with the capability to stable environmental conditions, as well as various operating modes including one-dimensional scatterometer, two-dimensional SAR, and three-dimensional tomogram measurements (Appendix C). Figure 10 is an exploded view of the layout of the EMSL.

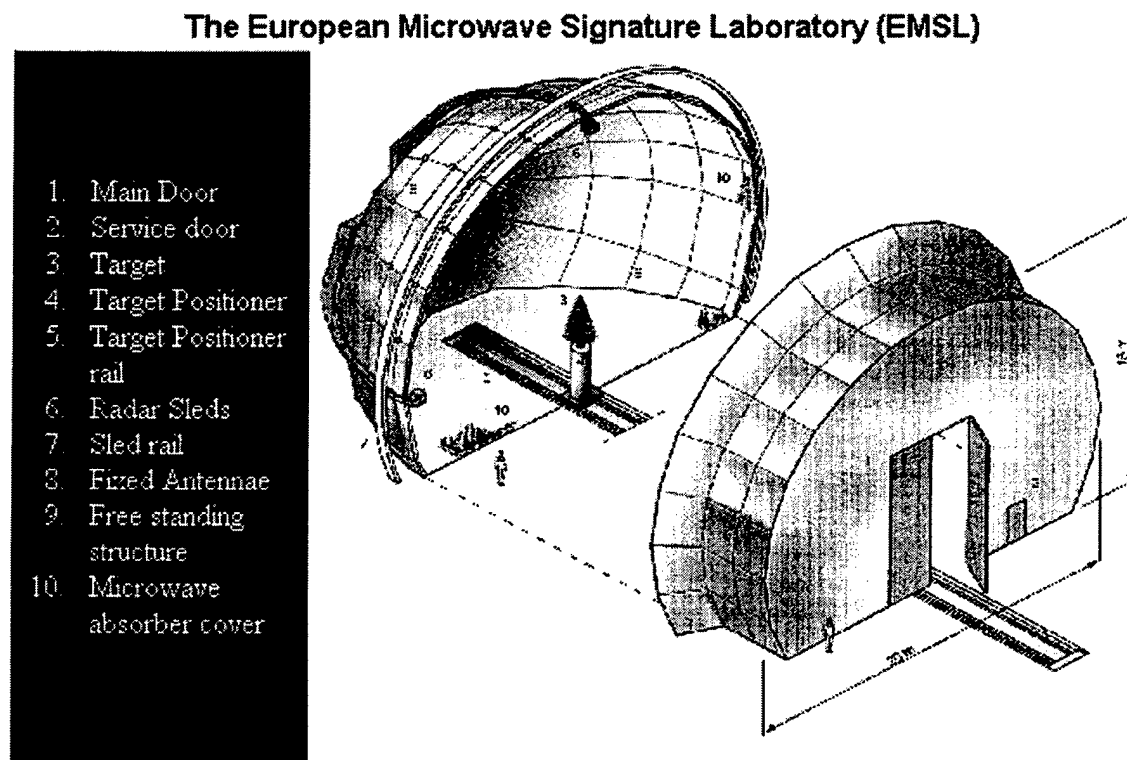


Figure 10: Physical Layout of the EMSL

The distance from the antennae to the range focus is 10 m. One of several object positioners of varying heights can be selected based on the size of the object to be measured. To increase the ease of mounting heavy objects, the object positioner can be moved outside the range through the main door, and a crane is used to place the object upon the positioner. For small objects such as the canonical objects used in this work for

far-field measurements, a mechanical scissor-lift can be brought inside the range so that the object can be manually placed and aligned with relative ease. The interior of the chamber is covered with pyramidal microwave absorber to attenuate the reflections from radiation incident upon the chamber walls.

4.4.2 Alignment of reference objects

The EMSL uses lasers mounted on the antenna sleds to align the objects. The laser is located at the center of the sled, and points to the center of the range focus to within about 0.1 degrees. The transmit and receive antennae, however, are located at a position offset from the laser, such that the angular separation between the lasers of both sleds is the same as the angular separation between the transmit and receive antennae on their corresponding sleds (within the plane of sled movement). When performing a laser alignment for an object such as the calibration disk, the laser of sled B is activated and the disk is oriented such that the laser reflects off the disk and onto the center of sled A. The position of the receive sled (usually sled A) must then be corrected to account for the offset of the antennae with respect to the laser (Figure 11). In this figure the dotted red line represents the laser (transmitted from sled B to sled A), and the dark blue line is the path of the RF energy as it reflects off the disk. It is necessary to close the angular separation between the sleds by 1.4 degrees in order to align the main lobe of the specular reflection of the disk onto the receive antenna of sled A.

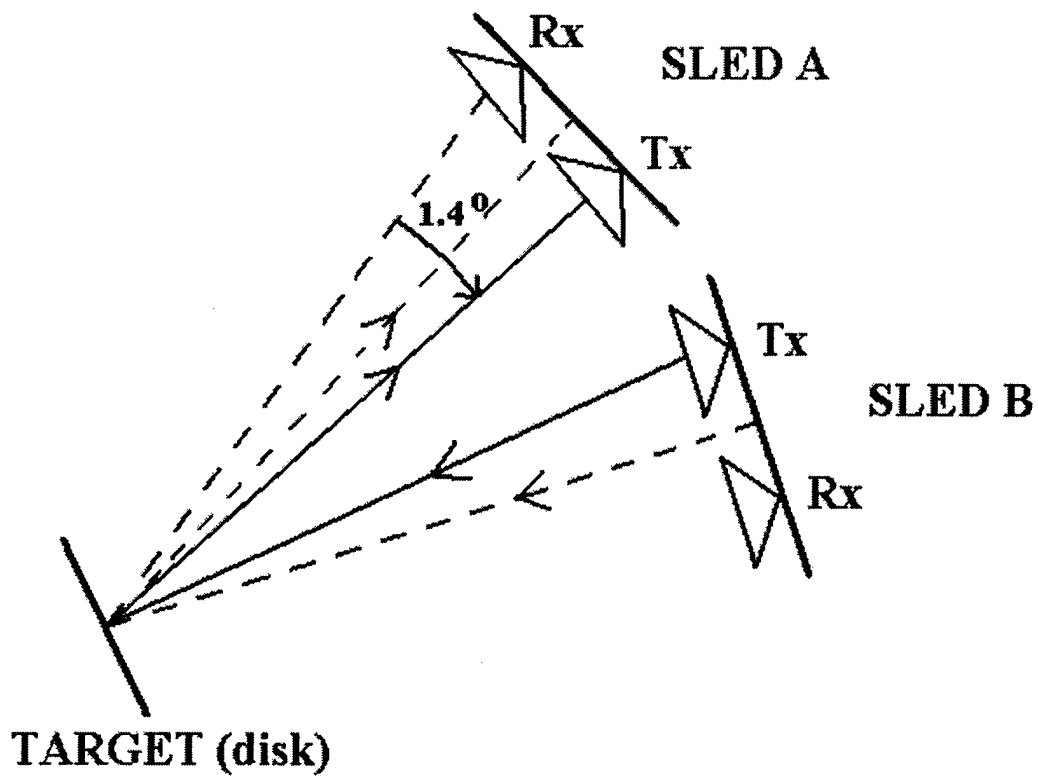


Figure 11: Alignment of Calibration Disk in the EMSL

With this laser alignment procedure, the alignment of a circular metallic disk of 20 cm diameter can be repeated to within 0.1 dB. Figure 12 shows two independent alignments of this disk, separated by over a week's time, and with completely independent pedestal placements. The measurements are both gated and subtracted.

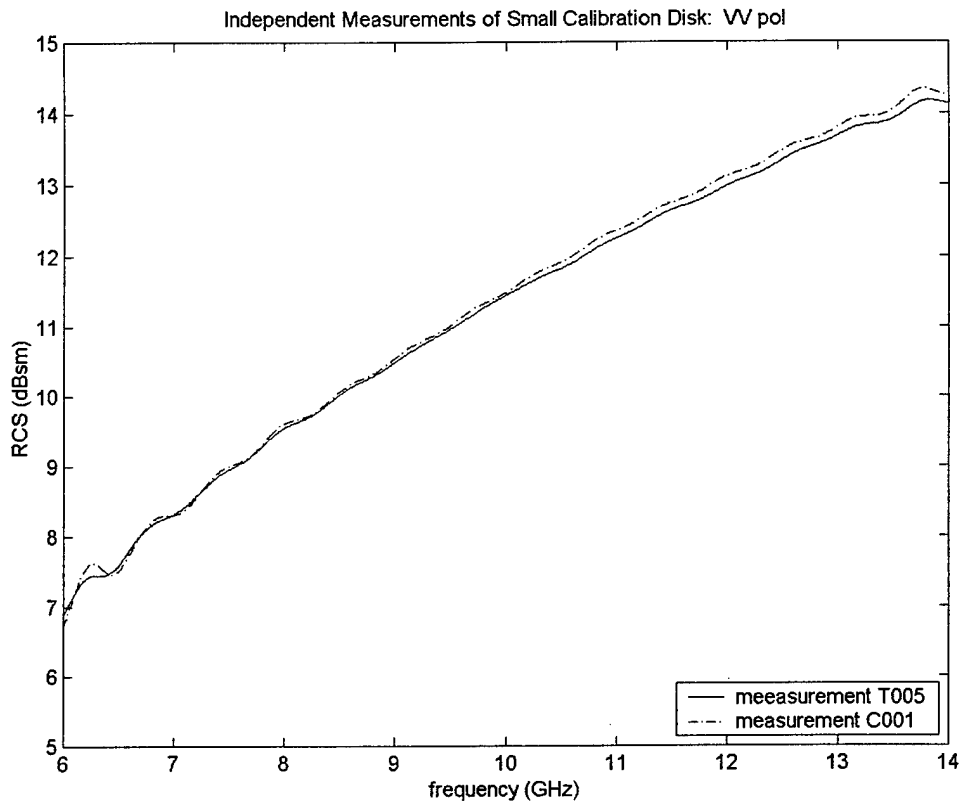


Figure 12: Repeatability Comparison of Calibration Disk Measurements

The 0.2 dB difference between these measurements is likely *not* due to alignment error, but rather system drift. If alignment error was the source, then the disparity between the measurements would increase with frequency, as the electrical size, and therefore the alignment sensitivity of the disk, increased. From the results of this analysis, it can be safely assumed that alignment repeatability will yield results well within the 0.5 dB measurement error limit that is advertised in the EMSL (Nesti, et al, 1994).

4.4.3 Antenna polarization purity

Good antenna polarization purity is an important characteristic to the range in which the test measurements are being taken. Since the goal is to produce results with

wide applicability, to include measurement systems with poor cross-polarization purity as well as those with good cross-polarization purity, this range must be able to simulate both of these. For comparison, one can simulate poor cross-polarization purity by a matrix rotation of the measurement. The purity of the EMSL antennae is between 30 and 40 dB (Nesti, et al, 1994). To verify this, a measurement of a metallic sphere was taken. The sphere has no theoretical cross-polarized RCS; therefore the level of cross-polarized radar return relative to the RCS of the co-polarized channels represents the antenna cross-polarization impurity. Figure 13 shows a measurement of such a sphere from 5 – 15 GHz, which is the frequency range of interest for this work.

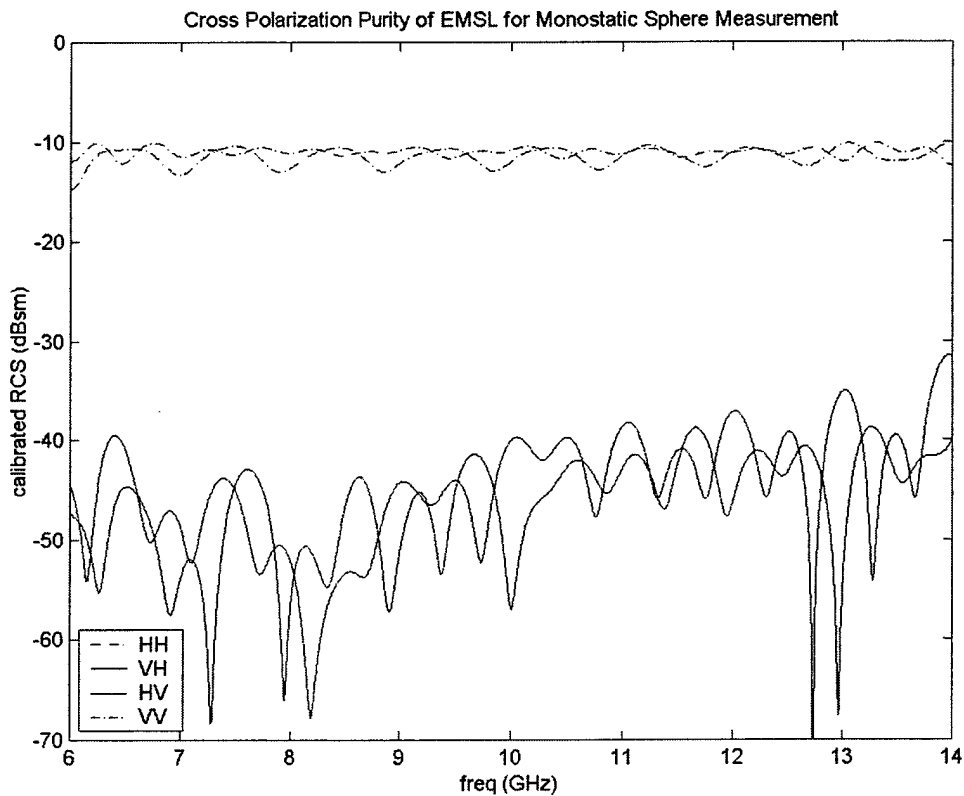


Figure 13: Antenna Cross-Polarization Purity

The separation between the co-polar and cross-polar components of the measurements is about 30 dBsm. As mentioned above, the cross-polar RCS that is measured is representative of the antenna cross-polarization impurity. Therefore it can be said that the cross-polarization purity of the EMSL antennae is about 30 dBsm.

4.4.4 Signal-to-noise ratio and repeatability

The EMSL has no hardware gating capability. As a result, ambiguous clutter (clutter that occurs outside the range cell) in the measurement, which arise as a result of multiple reflections from the chamber walls and mounting apparatus, as well as antenna coupling decrease the signal-to-noise ratio (SNR). Increasing the integration, or averaging of each individual measurement can increase the SNR. Averaging over 2^N points increases the SNR by a factor of N dBsm relative to no averaging. However, averaging beyond 1024 points becomes time-prohibitive and decreases the quality of the background subtraction due to the time separation between the object measurement and empty-room measurement. To evaluate the repeatability of a given microwave measurement and excluding the factor of alignment, independent measurements (i.e., separate mountings, and separated by more than a day's time) are taken for an object that is completely insensitive to alignment. The metallic sphere is such an object. Figure 14 shows two independent measurements and the coherent difference of the two. For these measurements, 2048 averaging points were used. The data were calibrated with identical distortion matrices. This amount of averaging is excessive for most bistatic measurements in the EMSL, as it degrades the quality of the background subtraction.

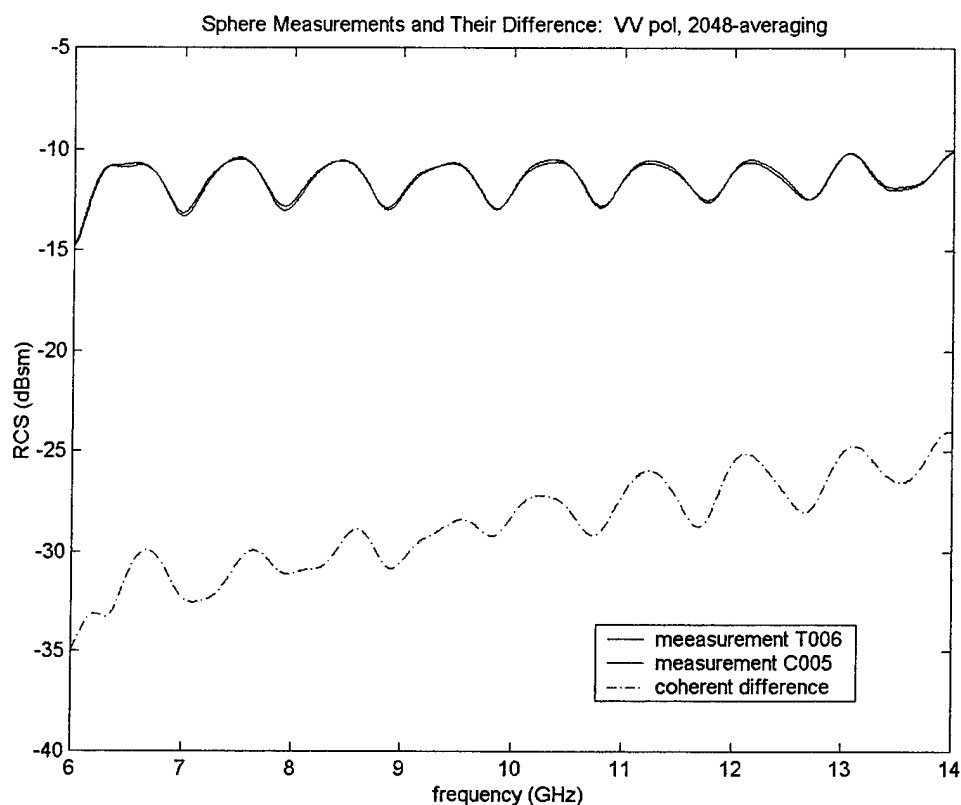


Figure 14: Repeatability of a Measurement of the 30.5 cm Metallic Sphere, $\alpha=120^\circ$

The difference between the measurements of Figure 14 always increases with frequency. This is due to the increased SNR at high frequencies, as a result of the loss in the coaxial cables. At the highest frequency of interest (15 GHz), the measurement can be repeated to within a difference of -12 dB.

One can get a better idea of the actual SNR of the range by eliminating other factors such as mounting and time separation. Two *dependent* measurements (i.e. a single mount, very little time separation between the two) are taken and the results of the two are subtracted. Figure 15 shows these measurements. The difference between the two

represents the noise floor for 512-point averaging.

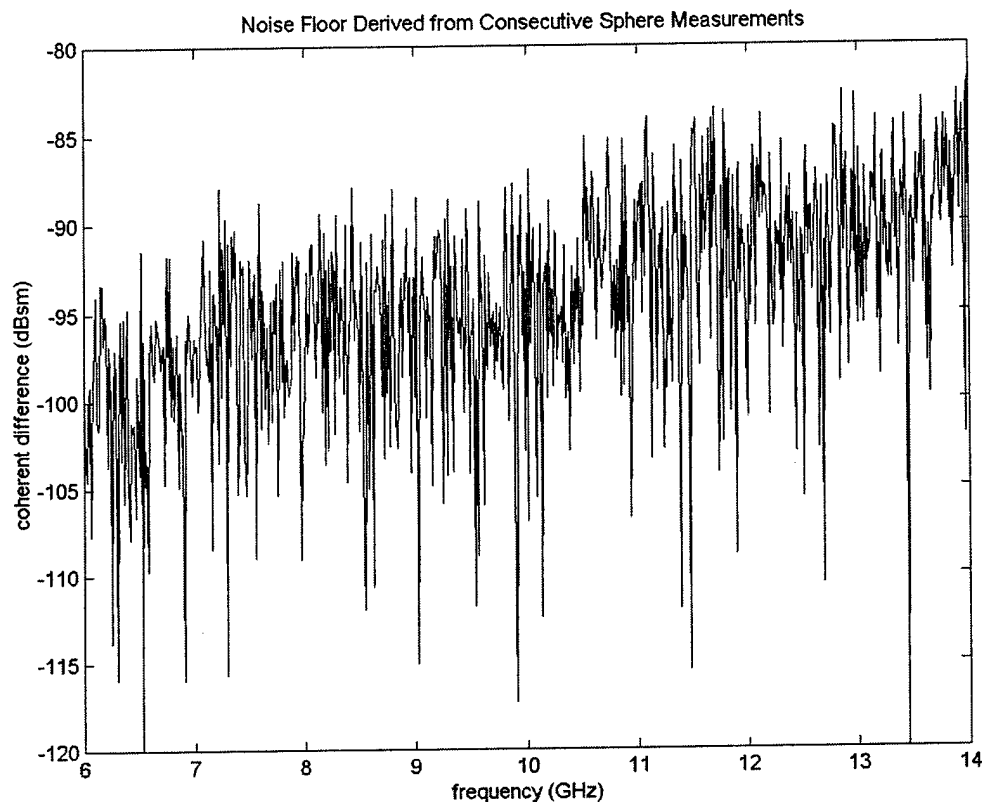


Figure 15: Noise Floor Derived from Sphere Measurement (512-averaging)

From the figure, it can be seen that the noise floor does not exceed -85 dBsm. The noise floor of the system (that is, without averaging) can be calculated by subtracting the effect of averaging. Given that this measurement uses ($2^9 =$) 512-point averaging, 9 dB should be added making the system noise floor about -76 dB.

4.4.5 *Ease, efficiency, and versatility*

Pedestal design is the most important factor in the ease and efficiency of mounting an object for measurement. If pedestals can be designed such that objects can be switched on the object column without the need of any other modifications to the setup,

the time it takes to move the objects is minimal. Because of the EMSL's large size, mechanical lifts are required to facilitate the movement of objects, and as a result safety becomes a major concern. Measurement setup is rather efficient with two or more people operating the range. After the measurement is set up, the EMSL uses an automated data acquisition and control system to allow it to perform a complete measurement without human intervention.

The EMSL was designed to measure a large variety of objects. The object column can support objects of up to six tons in weight. For far-field measurements, the maximum linear dimension of the object must not be more than about 27 cm. For a direct-illumination range (one without reflectors) this is a very sizeable quiet zone, and can easily support a wide variety of canonical objects. ROHACELL 51 foam is used as mounting material. The foam is much more rigid than commercial Styrofoam, and has a relative dielectric constant of $\epsilon_r = 1.071$ (Weinberger and Nesti, 1994). The rigidity of this foam permits the use of heavy objects, and the foam can also be machined into mechanical parts such as pivots and screw threads to make object alignment more efficient.

4.5 Measurement

For each measurement of Table 1, a systematic alignment error was introduced (with the exception of the sphere measurement). As shown in Figure 16 for the small disk, alignment error was introduced from 0° to 2° , in increments of 0.5° .

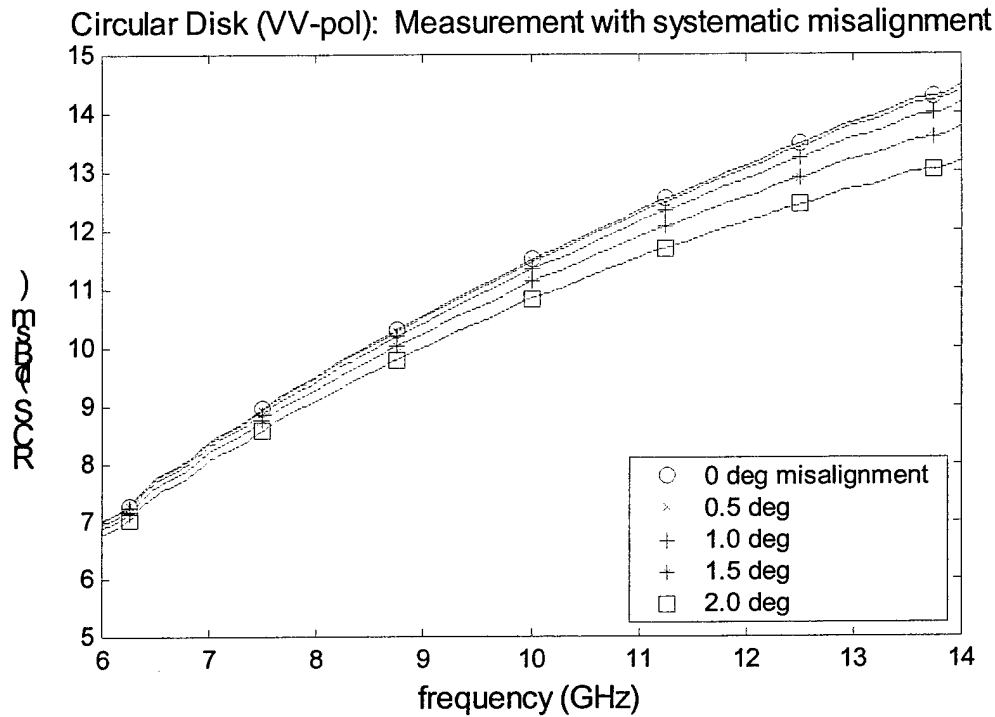


Figure 16: Measurement of circular disk with systematic misalignment

Depending on the object, this alignment error was added in azimuth *or* elevation. The choice of which axis to rotate the object was made in accordance to which would produce the most destructive error in the measurement. In the case of the horizontally cylinders, for instance, an alignment error in the elevation plane would not produce an appreciable error, given that the measurement is in the quasi-monostatic region. An azimuthal alignment error, therefore, was added. For the dihedral measurements, an elevation error was used since the dihedral in the vertical, or near-vertical orientations has a relatively flat RCS vs. bistatic angle when the receiver is scanned in the azimuth plane.

5 RESULTS

5.1 Dihedral (Monostatic)

In a monostatic configuration, a dihedral provides an excellent reference object for the purpose of cross-polarization calibration. The theoretical prediction is not easy to realize; it is necessary to generate a Moment Method simulation. However, cross-polarization calibration can be accomplished with two measurements of the same dihedral in different orientations, without knowledge of the exact theoretical RCS prediction, as done in the EMSL simple polarimetric calibration technique (3.2).

The scattering matrix of the dihedral oriented with the seam parallel to the vertical axis (the direction of vertical polarization) looks like:

$$\mathbf{S} = S_{vert} \begin{bmatrix} -1 & 0 \\ 0 & 1 \end{bmatrix} \quad (51)$$

For a dihedral composed of two identical faces at right angles to each other, with face dimensions a and b , the RCS (S_{vert}) is:

$$S_{vert} = \frac{16\pi a^2 b^2}{\lambda^2} \quad (52)$$

The scattering matrix of the same dihedral rotated in the plane defined by the direction of the wave propagation can be found by a rotation of the scattering matrix of Eq. (51), explained in (Mott, 1992). At a rotation through angle θ , the scattering matrix becomes:

$$\mathbf{S} = \sqrt{S_{vert}} \begin{bmatrix} -\cos(2\theta) & \sin(2\theta) \\ \sin(2\theta) & \cos(2\theta) \end{bmatrix} \quad (53)$$

and if $\theta = 22.5^\circ$, then,

$$\mathbf{S} = \frac{\sqrt{S_{vert}}}{\sqrt{2}} \begin{bmatrix} -1 & 1 \\ 1 & 1 \end{bmatrix} \quad (54)$$

The advantage of using the dihedral in an orientation such that the scattering matrix is of the form of Eq. (54) is twofold: first, the absolute amplitude need not be known if the amplitude in the $\theta = 0^\circ$ orientation is known (S_{vert} is known); second, the elements of the scattering matrix each have equal amplitude, yielding strong cross-polarized response, as well as making it linearly independent from all co-polarizing scatterers.

The disadvantage of using the dihedral as a calibrator is its alignment sensitivity. For measurement systems which use two closely-separated antennas for monostatic measurements (such as the EMSL), this antenna separation can be significant enough so that the RCS of each polarization channel is not balanced as Eq. (51) and (54) would indicate. In the case of the EMSL, the antennae on each sled are separated by about 1.7° . Figure 17 is the MoM prediction of a measurement in this configuration. It can be seen that the difference in the co-polarized channels reflects a difference of up to 1 dB at lower frequencies. The cross-polarized channels are non-zero, but negligible.

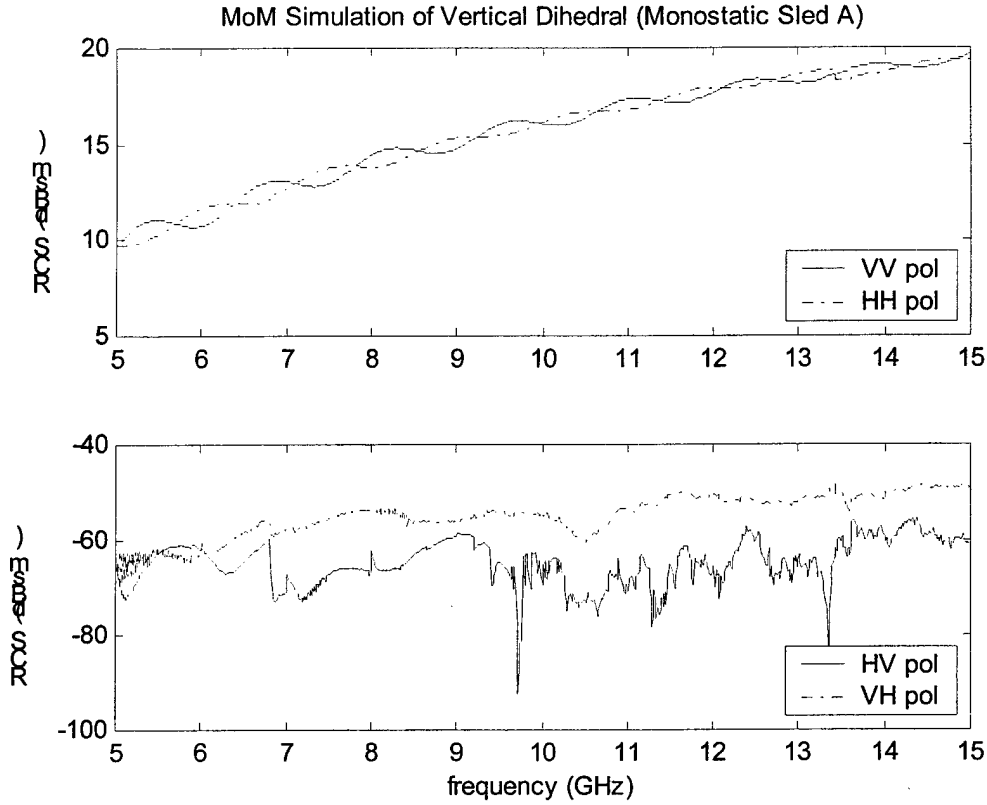


Figure 17: MoM simulation of an EMSL monostatic measurement of the vertical dihedral

These results indicate that the dihedral is best suited for monostatic cross-polarization calibration of a radar system that has a single Tx/Rx antenna, rather than two closely separated antennae.

For a Type-2 calibration, the ratio of the RCS of the vertical dihedral to the tilted dihedral is important. Using Eq. (51) and (54), one can predict the trend vs. frequency of this ratio.

$$\frac{S_{\text{vertical}}}{S_{\text{tilted}}} = \sqrt{2} S_{\text{vert}} \begin{bmatrix} 1 & 0 \\ 0 & 1 \end{bmatrix} \quad (55)$$

If a dihedral measurement such as this were to be used in a Type-2 calibration (one for which the exact scattering matrices of the cross-polarizing reference objects is not

known), the ratio of the RCS the co-polarizing orientation to the RCS in the cross-polarizing orientation (in the case of the dihedral, 0° and 22.5° from vertical, respectively), the trend of RCS vs. frequency shown in Figure 18 results:

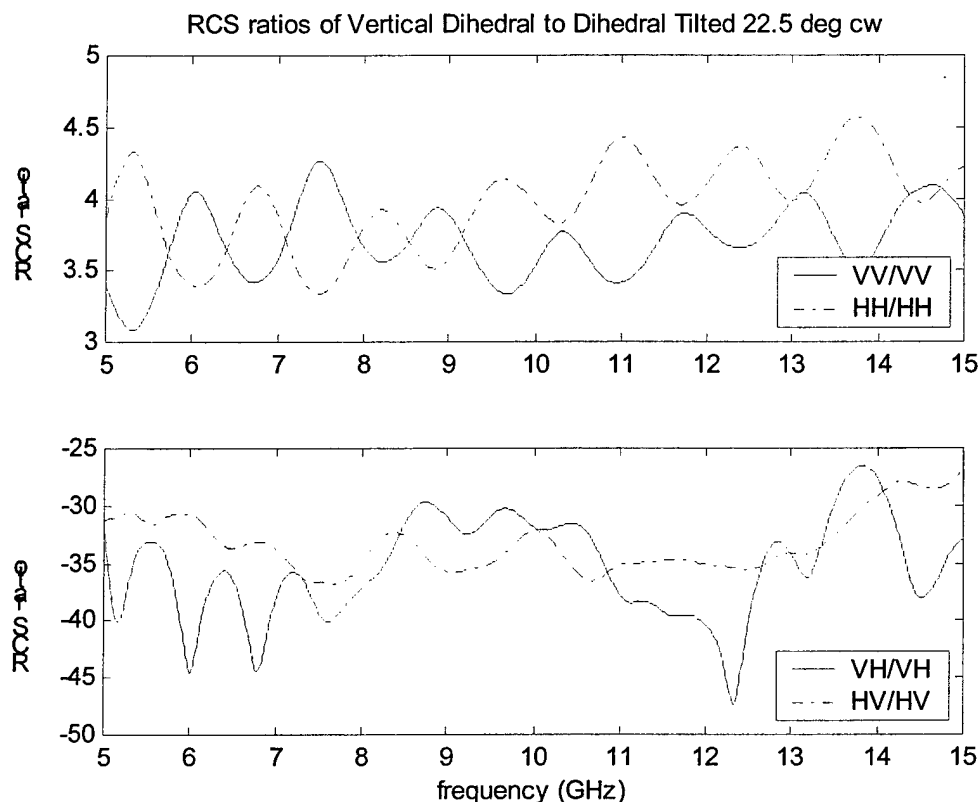


Figure 18: Calibrated RCS ratios of measurement of dihedral in two orientations—performed in the EMSL

The calibrated ratios of this figure would be relatively flat in a true monostatic scenario. The rippling due to the small separation between the Tx and Rx antennas in the EMSL makes these measurements inappropriate for cross-polarization calibration in a Type-2 technique, since the RCS of the tilted dihedral *relative to* the RCS of the vertical dihedral for each polarization channel is a smooth trend vs. frequency, as indicated by Eq. (54).

For a Type-3 calibration, a dihedral measured with a similar angular separation between the antennas would be perfectly suitable. It is only necessary for this type of calibration that the depolarizing object has a high cross-polarized RCS—a requirement that is met in the tilted dihedral, even at a small bistatic angle.

5.2 Dihedral (Bistatic)

As one might predict, the dihedral measurement at a larger bistatic angle (this time, using Tx and Rx antennae on separate sleds, creating a bistatic angle of about 6°), creates an even larger deviation from the ideal monostatic response. The tilted dihedral still yields a large cross-polarized RCS, which makes it suitable for a Type-3 calibration, but the vertical dihedral begins to return higher RCS in the cross-polarized channels. This phenomenon creates problems for the calibration, since it is no longer a good approximation to set the cross-polar RCS to zero in the theoretical prediction; it instead must be solved for. But the low levels of the cross-polarized RCS make it difficult for an iterative MoM solver code to calculate with accuracy (see Figure 17, specifically the HV-pol channel). This effect will not just degrade the cross-polarization calibration capability of a Type-3, but will degrade the *overall* performance of the calibration.

5.3 Long Cylinder

The long cylinder (that is, a cylinder which has a length/diameter ratio of greater than two) offers a higher specular RCS than a sphere of the same diameter, but suffers the problem of alignment sensitivity—more so than is true of the squat cylinder. Figure 19 shows the measurement of the long cylinder with the axis of rotation oriented horizontally, or parallel to the E-field of the H-polarization channel. The results of the

bistatic measurement (using both antenna sleds) are similar to the monostatic measurement (using a single sled), with the exception that the SNR of the bistatic measurement is higher, which is a result of poor amplification characteristics of the antennas on sled A. The levels of the cross-polarized channels (theoretically zero) give some indication of the cross-polarization impurity of the measurement.

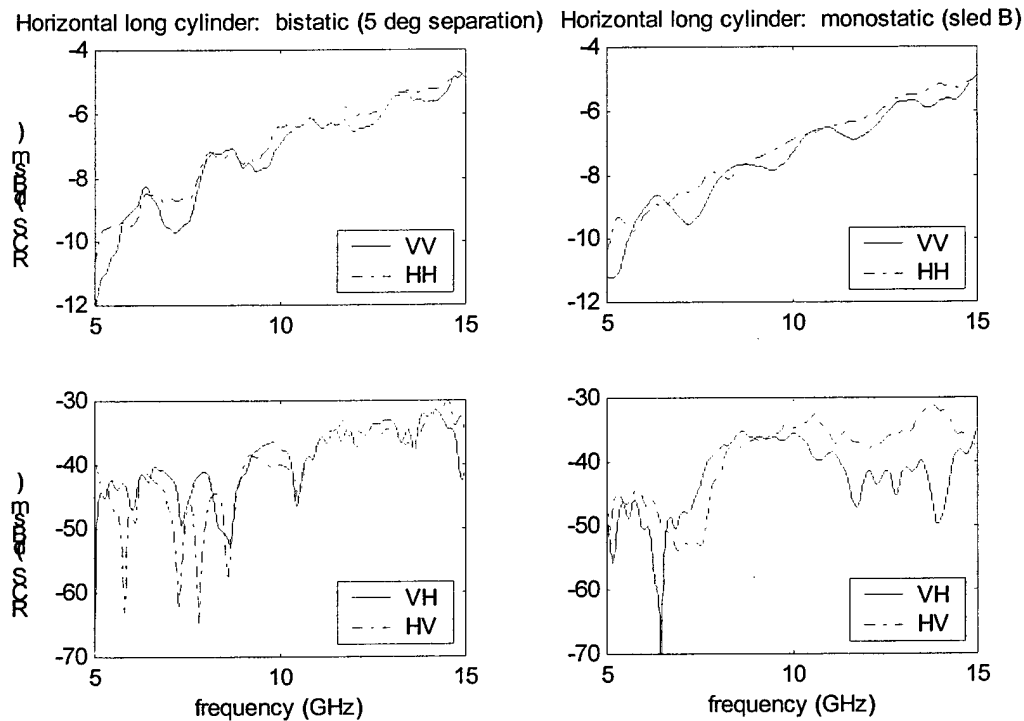


Figure 19: EMSL measurements (Type-2 calibrated) of the long cylinder

Figure 20 compares the co-polarized channels of this measurement with the predicted MoM solution. The agreement of the co-polarized channels is within 1 dB over 5-15 GHz.

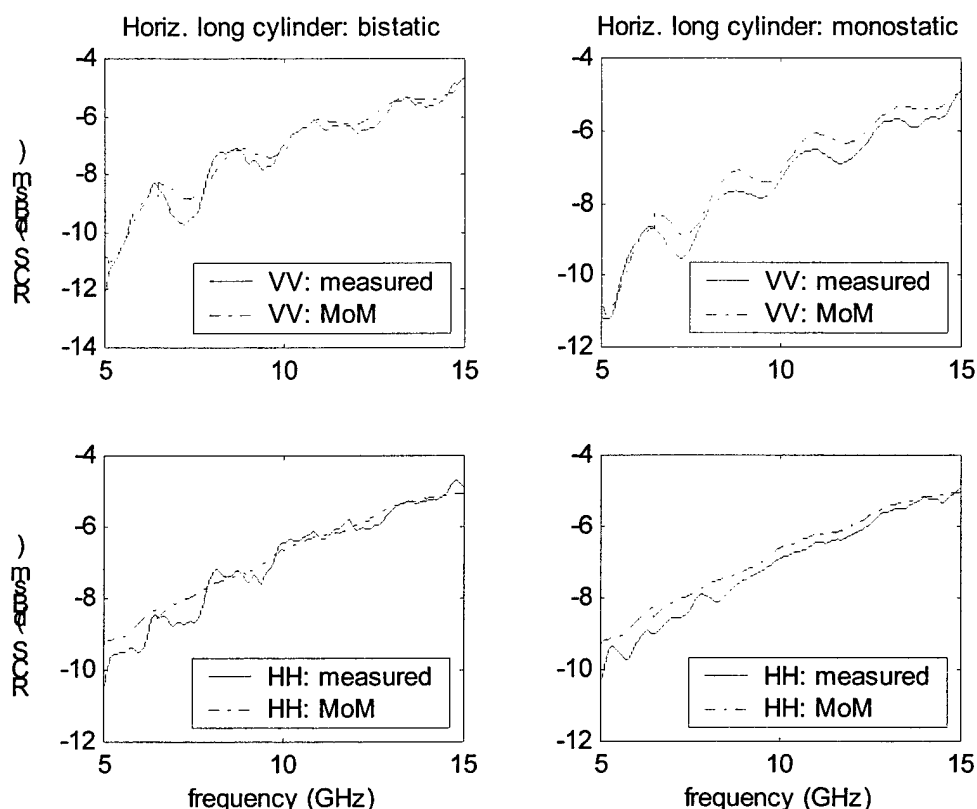


Figure 20: EMSL measurements of Figure 19 vs. MoM simulations

A possible reason for using a long cylinder as a calibration reference object would be the ability to produce a large cross-polarized RCS component when the object is rotated. A thin cylinder, when tilted within the plane defined by the incident plane wave, when the axis of rotation of the cylinder is parallel to that plane, will produce cross-polarized RCS return, much like the dihedral, but has little specular return. By using a fatter cylinder (this long cylinder has a diameter of 50 mm and a length of 200 mm), the specular RCS is increased, at the cost of the amplitude of the cross-polarized RCS that can be returned. Figure 21 shows that the cross-polarized RCS of such a cylinder rotated 45° in the plane of the incident plane wave produces a cross-polar RCS below about -30 dB, which, for the sensitivity of the EMSL, is not sufficient for cross-polarization calibration.

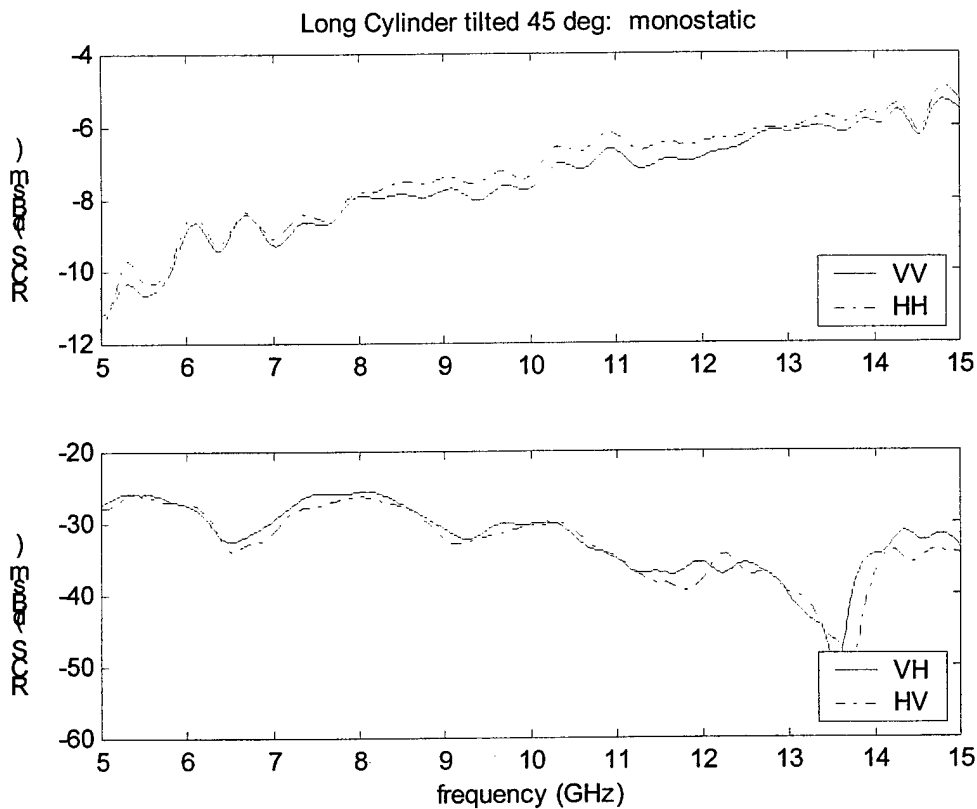


Figure 21: EMSL measurement of long cylinder, tilted 45°

5.4 Squat Cylinder

The squat cylinder (a cylinder with a diameter/length ratio of greater than two) has a higher monostatic RCS than the long cylinder with the same maximum linear dimension. This is important given that the maximum linear dimension of the object is the limiting factor for the maximum size of the object required for far-field measurements. This higher RCS in monostatic and quasi-monostatic measurements is combined with the fact that the squat cylinder provides much less cross-polarized RCS when tilted off the axis of rotation, as seen in Figure 22, in which case the RCS of the squat cylinder is approximately 2 dB higher than in Figure 21, and the cross-polarized RCS component is low enough to be indistinguishable from the ambient noise.

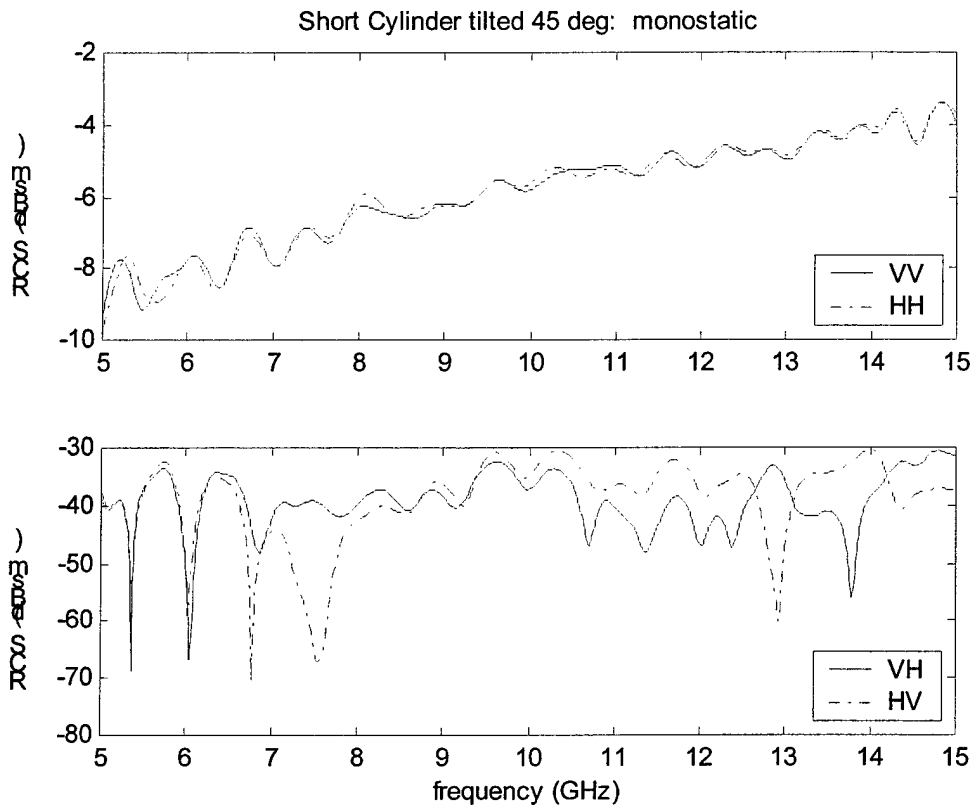


Figure 22: EMSL measurement of short cylinder, tilted 45°

The squat cylinder is used successfully in the calibration of the BICOMS system (Tuley, 1995), and takes advantage of the flat end-cap of the cylinder for bistatic phase calibration. This particular usage illustrates each of the strengths of this cylinder as a bistatic reference object. The RCS is high (higher than a sphere of the same diameter) in the co-polarized channels, is largely insensitive to alignment error (illustrated in Figure 23 through the comparison of the bistatic and monostatic measurements), and provides a flat, circular surface (the end-cap) to provide an RCS return with a distinct phase peak. The MoM prediction of the squat cylinder in both monostatic and bistatic configurations (shown in Figure 24) also demonstrate that the squat cylinder is predicted more easily

than for the long cylinder (using a Combined-Field Integral Equation (CFIE) and an iterative matrix solver).

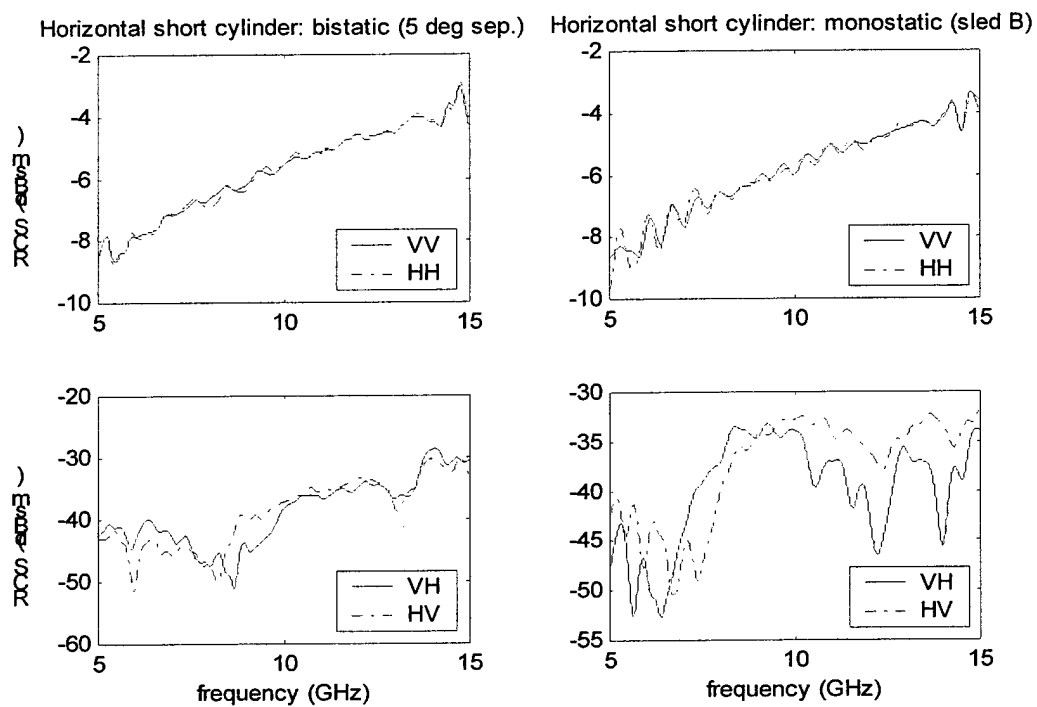


Figure 23: EMSL measurements (Type-2 calibrated) of the short cylinder

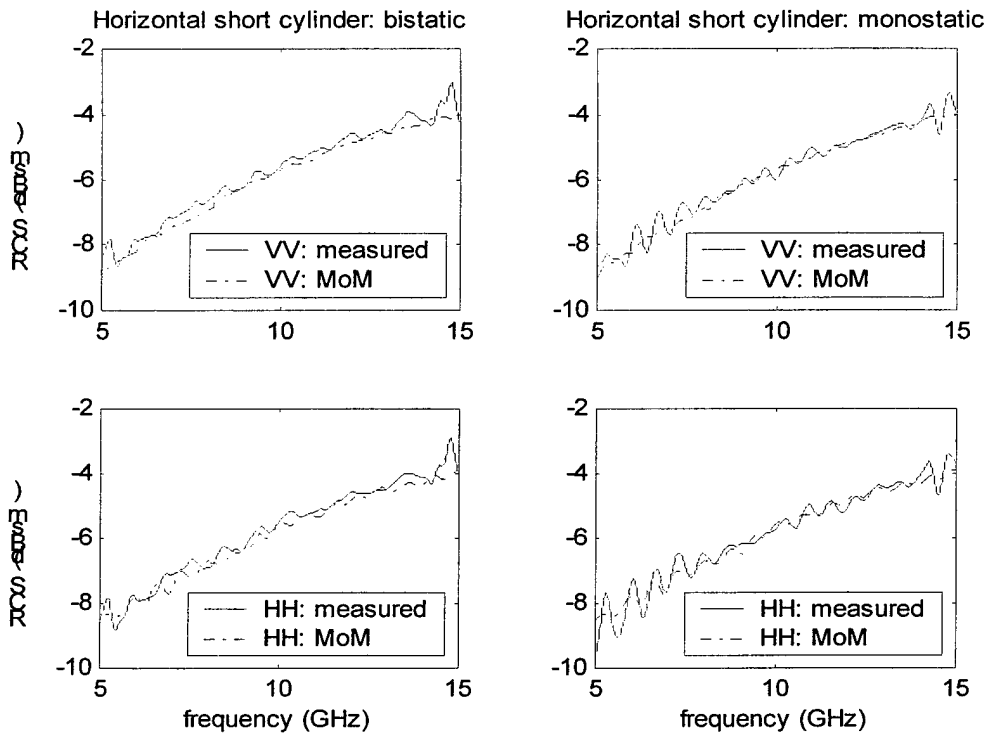


Figure 24: EMSL measurements of Figure 23 vs. MoM simulation

5.5 Trihedral

The high RCS return of the dihedral is the primary reason it is a popular monostatic calibration reference object. The cross-polarized return is non-zero in this case (Figure 25) because the edges of the trihedral are manufactured such that two of the three are aligned diagonally with respect to the horizontal and vertical directions. The diffraction from these edges reflects a cross-polarized RCS.

The experiment published in (Peters, 1962) provides an analysis of this type of trihedral (called a *triangular dihedral*) as a bistatic calibration device. The RCS of the trihedral becomes highly rippled and dramatically lower as the bistatic angle is increased past about 6° . The high degree of rippling makes the trihedral extremely difficult to align such that the RCS is predictable. From this it can be stated that the triangular trihedral is

not suitable at all for bistatic calibration—only for monostatic co-polar amplitude calibration.

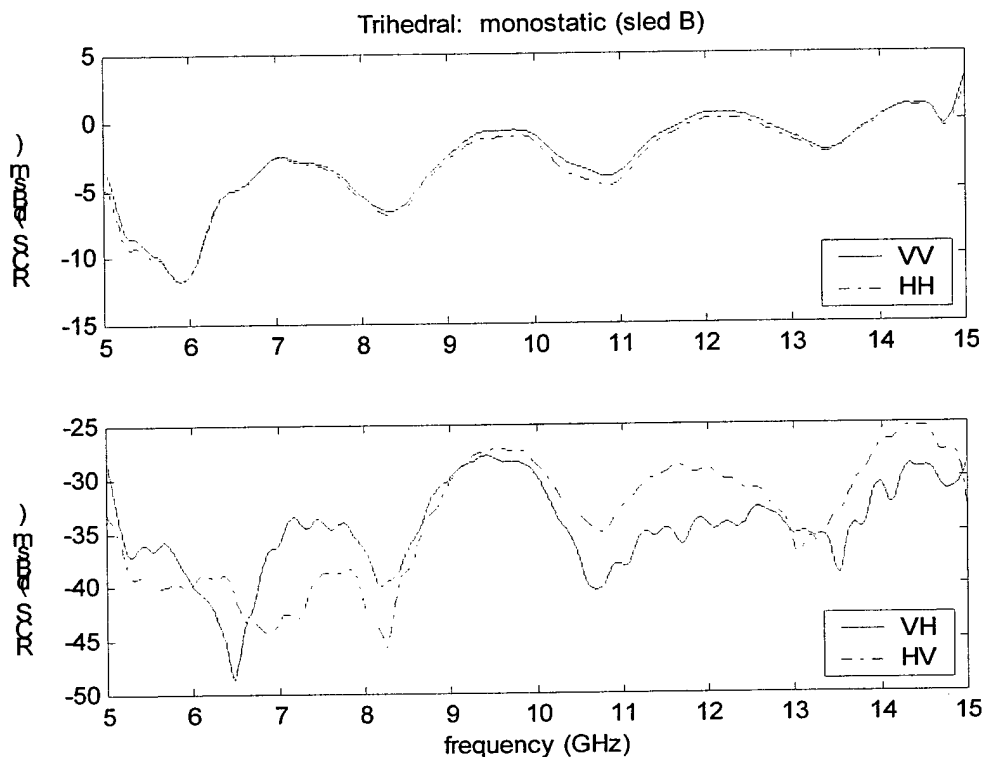


Figure 25: EMSL measurement of the trihedral

Figure 25 displays a monostatic measurement of the trihedral. The cross-polarized RCS is non-zero, but low enough to be indiscernible from the clutter and polarization channel cross talk. The cross-polarized RCS levels are the result of edge diffraction from the forward edges that are oriented diagonally with respect to the antenna. The low levels of the cross-polar RCS make it hard to predict, and thus unsuitable for any Type-3 calibration, because an accurate theoretical prediction cannot be produced. The use of a square dihedral, where the edges are all parallel or perpendicular with respect to the antenna, would alleviate this problem.

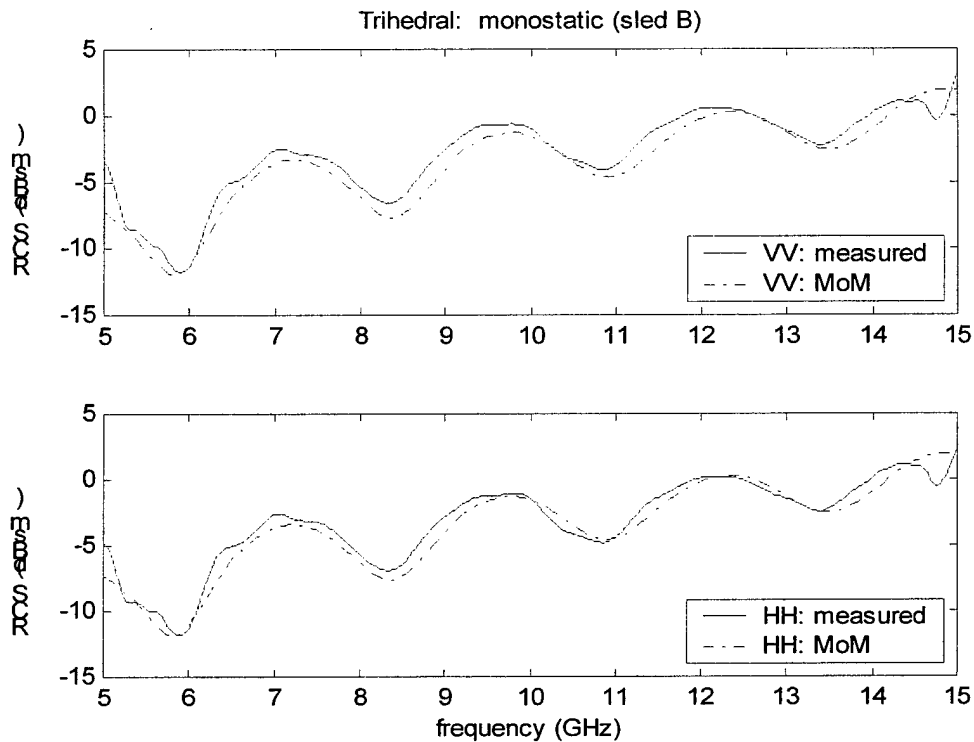


Figure 26: EMSL measurement of Figure 25 vs. MoM simulation

The MoM simulation on the trihedral produces the desired accuracy (within 1 dB), as seen in Figure 26. The lobing in the frequency domain makes the trihedral sensitive to misalignment, however the lobing is shallow enough so that the co-polar RCS remains highly predictable.

5.6 Circular Disk

The combination of high co-polar RCS and a readily available theoretical prediction (via Physical Optics) make the circular disk an obvious choice for monostatic or quasi-monostatic calibration. The disk is extremely alignment-sensitive, however, and alignment verification can add precious time to a calibration procedure. In the EMSL, which uses a precise laser alignment system, the circular disk has shown to be a very valuable object. The cross-polar RCS return due to diffraction from the disk's edge is

very low relative to the co-polar RCS, giving the scattering matrix a nearly pure co-polar response. This response is displayed in Figure 27.

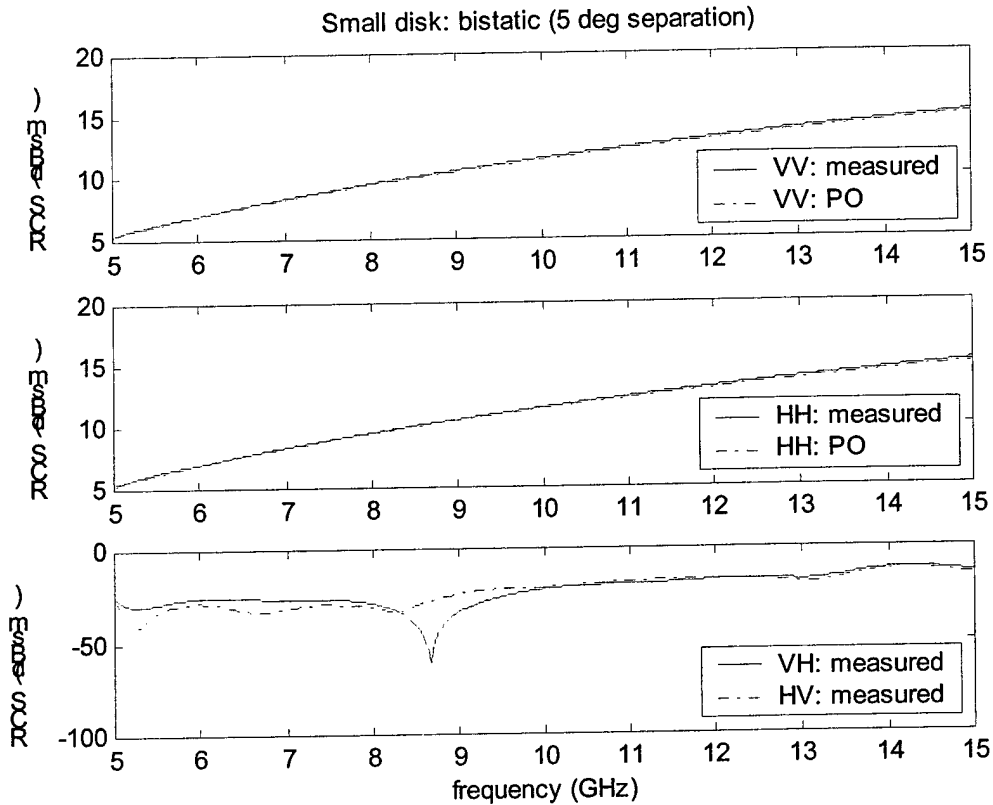


Figure 27: EMSL measurement of the small disk vs. PO prediction

5.7 Sphere

The rotational symmetry of the sphere about any axis alleviates almost all alignment problems normally associated with a calibration measurement. Since the sphere needs to be fairly large to produce an RCS high enough to calibrate with, object positioning can become a problem. A large sphere measured at a small bistatic angle is also necessary to mitigate the creeping wave contribution. The creeping wave for a sphere that occupies all or exceeds the dimensions of the quiet zone will not interact with the specular return in a manner characteristic of a far-field measurement. The magnitude

of this creeping wave decreases in proportion to the size of the sphere, and is further reduced when measured at small bistatic angles, leaving only the specular RCS return, which is contributed primarily from only the front of the sphere, allowing a far-field near-monostatic measurement to be performed on a sphere for which the dimensions exceed the dimensions of the chamber's quiet zone.

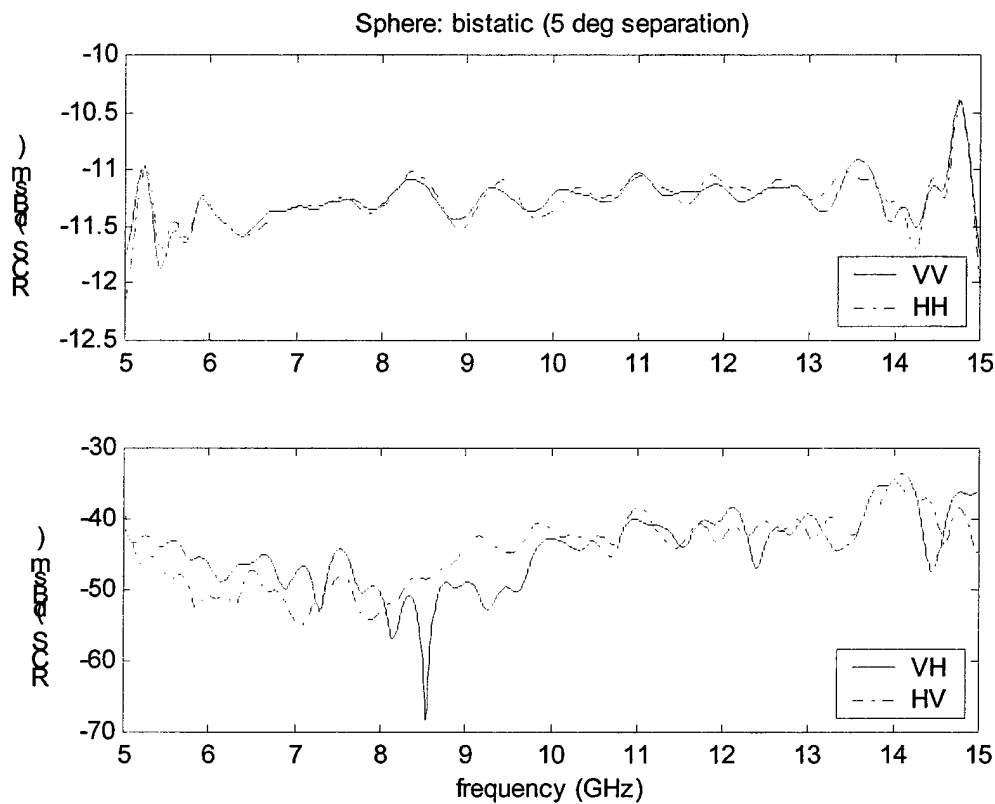


Figure 28: EMSL measurement of the 30.5 cm diameter sphere

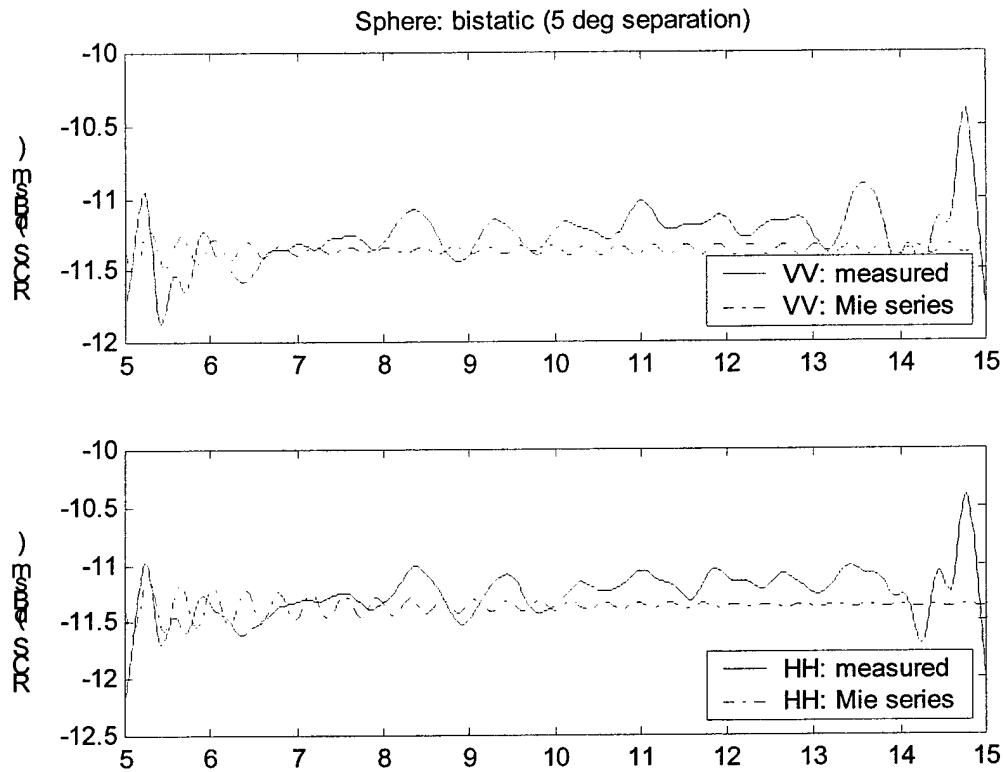


Figure 29: EMSL measurement of Figure 28 vs. Mie series prediction

As seen from Figure 28 and Figure 29, the RCS of the sphere is relatively constant versus frequency in a near-monostatic configuration. This fact brings to light another possible advantage of using the sphere as a calibrator. As seen in the figures, the signal-to-noise ratio of the measurement is not large enough to be able to discern the lobing pattern of the RCS in the frequency domain (for both polarizations). Essentially, for this bandwidth, the lobing pattern is inconsequential. In creating a theoretical prediction, then, it would be just as useful to use a single complex constant for this entire bandwidth, rather than the vector that represents the true RCS. This would save memory and computational time in calibrating with this sphere at this bandwidth.

5.8 Wire Mesh

The wire mesh is a simple arrangement of parallel wires, in this case separated from each other by a distance of 1 cm. The mesh consists of 19 wires, each of length 20 cm. It acts as a sort of polarization filter, in that only the polarization component of the incident wave that is parallel to the length of the wires will be reflected—all other components are transmitted through the mesh. This assumes that the wires are thin enough such that the specular return from the other polarization(s) is negligible.

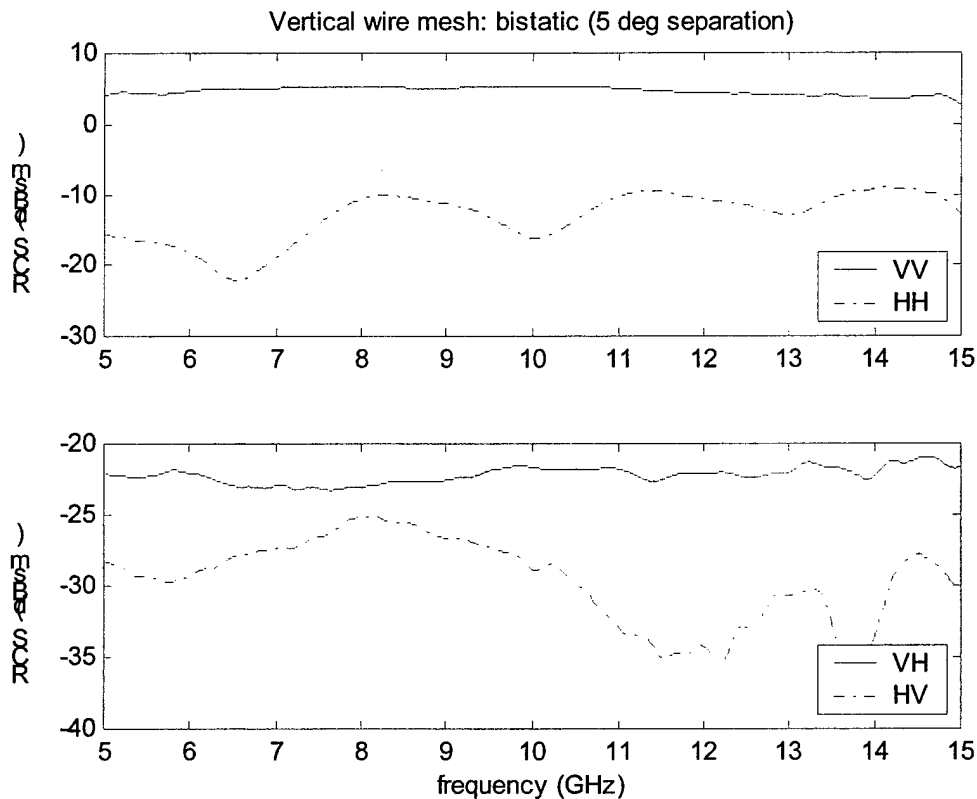


Figure 30: EMSL measurement of wire mesh (vertical orientation)

Under the assumption that the wires are both long and thin with respect to the incident wavelength, and further that the main lobe of the RCS is wide relative to the bistatic angle being considered, the scattering characteristics as a function of the orientation of the wires is approximated by the relationship of Eqn's (19) and (20).

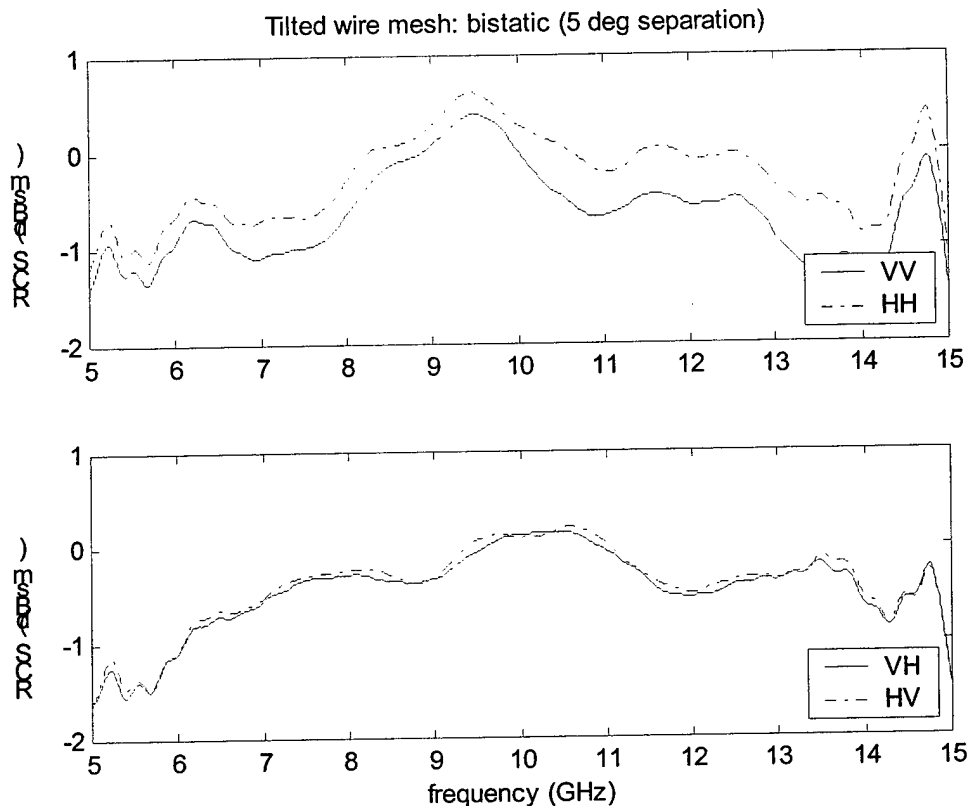


Figure 31: EMSL measurement of wire mesh (oriented 45° counter-clockwise)

In the measurement of the mesh for which the wires are aligned vertically (shown in Figure 30), the high, flat response of the VV channel is immediately apparent. Like the sphere, this is also a good characteristic for a calibration object. The large HH-pol component in this measurement is unexplained, although it could be a specular response or a traveling wave effect. The effect of the Styrofoam substrate on the measurement of the wires has not been considered, and may be necessary for further work on this calibration object.

Figure 31 shows the same wire mesh measured at an orientation 45° from vertical. As predicted, the RCS of each polarization channel is nearly identical, to at least within 1 dB. The ratio of the RCS versus frequency for the vertical and tilted orientations,

however, is not constant, which becomes apparent by a visual comparison of each plot. Since this object is used only as a cross-polarization compensation object for a Type-2 calibration, however, this ratio need not be as precise as the co-polarized amplitude calibrator, since the goal is not to create an amplitude correction factor similar to the co-polar channel compensation, but to isolate the distortion terms of the antenna's polarization distortion matrix.

The mesh of long, thin cylinders (wires) also gives this object exceptional bistatic scattering characteristics. The wide main lobe of the RCS response of each polarization channel allows it to be used as a good polarizing/depolarizing object for bistatic angles wider than 2° . This cannot be said of the dihedral, nor any other object with a high, predictable cross-polarized RCS. In the Type-2 calibrations performed in the EMSL, the calibration objects are measured at a bistatic angle of 5° , and the resulting cross-polarization isolation is quite good, as will be demonstrated in the next section.

5.9 Initial Calibration Analysis

For each of the four calibration techniques described in Section 3, an initial implementation was done as a validation of the calibration routines and measurements.

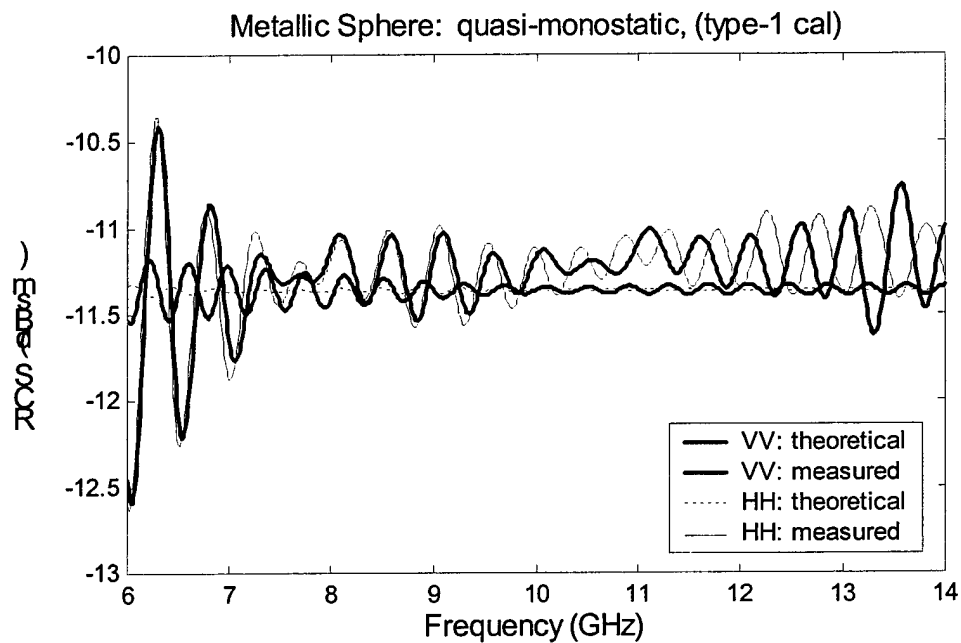


Figure 32: Metallic sphere calibrated using basic Type-1 calibration technique

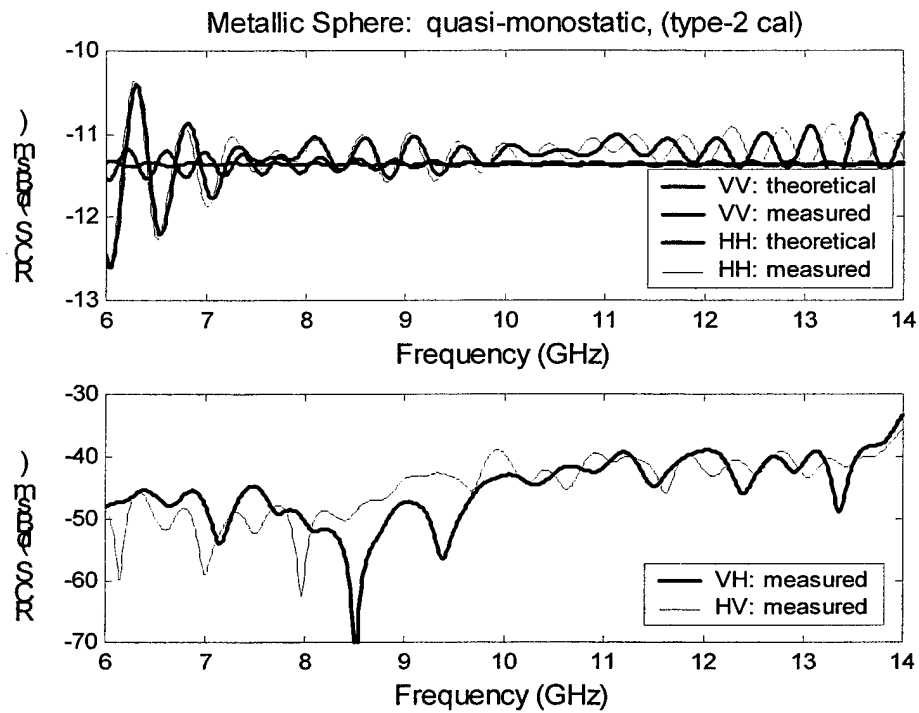


Figure 33: Metallic sphere calibrated using simple polarimetric calibration technique

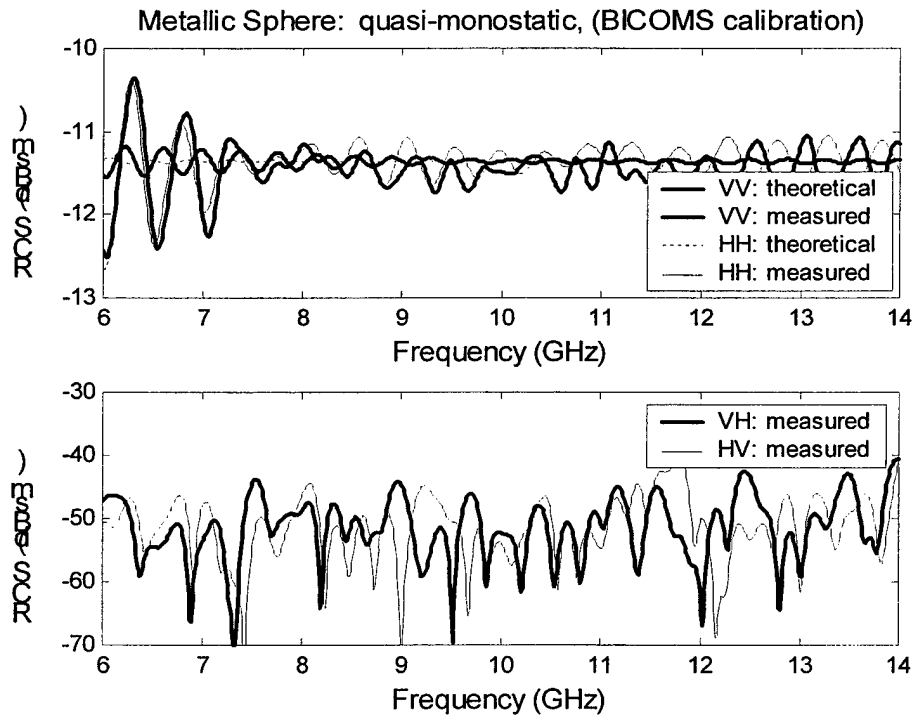


Figure 34: Metallic sphere calibrated using bistatic via monostatic calibration technique

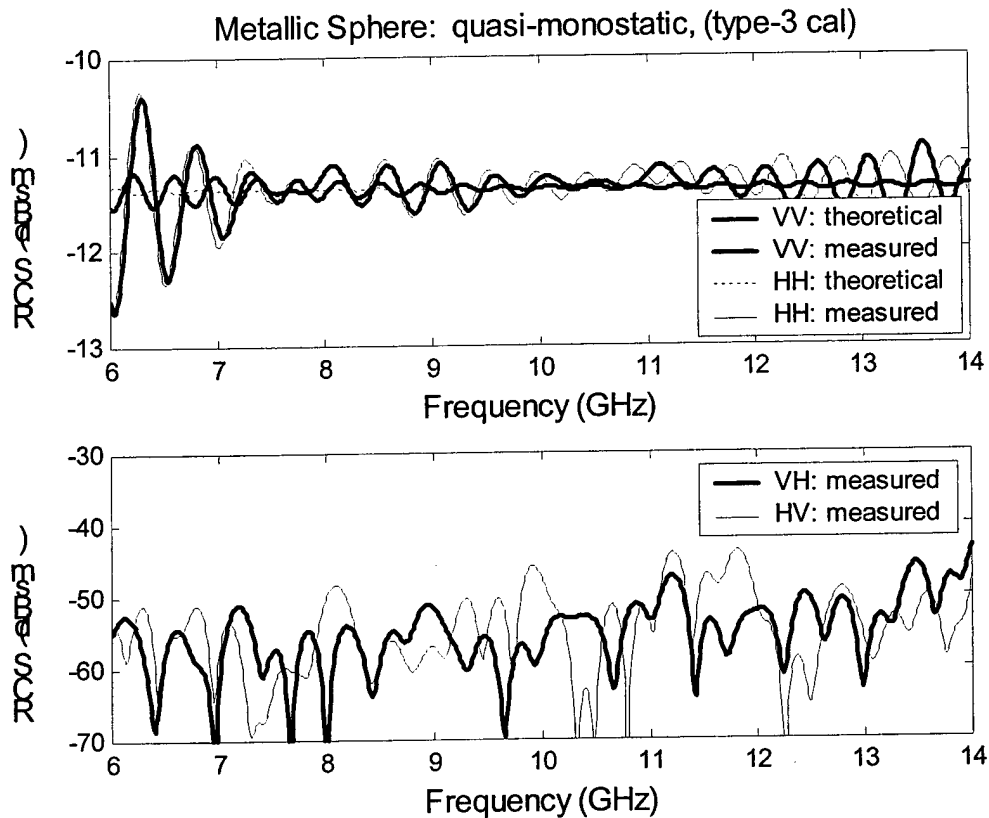


Figure 35: Metallic sphere calibrated using the general dual-antenna calibration technique

The calibrated measurements of in Figure 32 - Figure 35 show unacceptably high rippling in the region of 6–7 GHz. This is due to tight (software) range gating of the measurements. When the software range gate that is applied to the calibration is of a different size or phase than the gate performed on the measurement itself, this rippling becomes prevalent. Provided that the gates are consistent with each other in every measurement, this effect can be significantly reduced. This initial validation proves each of the calibration routines (implemented in MATLAB) to be legitimate.

5.10 Basic Type-1 Calibration Technique

This simple technique is analyzed mainly as a reference for the calibration methods under comparison. An error analysis on the Type-1 technique is another term for an error

analysis of the calibration object prediction itself, which one must find out in order to separate the shortcomings of the calibration and the shortcomings of the object prediction. The test object on which the calibration is used for the analysis here and in the following sections is a bistatic (5 degrees antenna separation) of the metallic sphere. These statistics are calculated only on the highest 1 GHz band of the measurement bandwidth (13-14 GHz) in order to highlight the effect of misalignment on higher frequencies.

Table 2: Average alignment error statistics for Type-1 calibration (small disk)

<u>Object Misalignment</u>	<u>VV-error</u>	<u>HH-error</u>	<u>VH level</u>	<u>HV level</u>
0°	0.17 ± 0.01 dB	0.10 ± 0.01 dB	-inf	-inf
1°	0.32 ± 0.04 dB	0.35 ± 0.01 dB	-inf	-inf
2°	1.24 ± 0.04 dB	1.28 ± 0.01 dB	-inf	-inf

Upon implementing a Type-1 calibration with the small disk, the statistics of Table 2 result. The cross-polar levels are zero (-infinity in dBsm) because the cross-polar RCS of the disk prediction was approximated as zero.

By implementing the Type-1 calibration with a sphere, one eliminates the need for precise alignment, at the cost of average error in the calibration, as seen in Table 3.

Table 3: Error statistics for Type-1 calibration (metallic sphere)

<u>Object Misalignment</u>	<u>VV-error</u>	<u>HH-error</u>	<u>VH level</u>	<u>HV level</u>
<i>N/A</i>	0.79 ± 0.15 dB	0.28 ± 0.03 dB	-inf	-inf

In order to obtain reasonable values for the cross-polarized calibrated RCS, an object must be used that has high RCS for all four polarization channels. The dihedral, tilted 22.5° from the vertical orientation is such an object.

Table 4: Error statistics for Type-1 calibration (dihedral tilted 22.5°)

<u>Object Misalignment</u>	<u>VV-error</u>	<u>HH-error</u>	<u>VH level</u>	<u>HV level</u>
0°	0.38 ± 0.04 dB	0.95 ± 0.01 dB	-39.3 dBsm	-39.3 dBsm
1°	2.76 ± 0.10 dB	3.68 ± 0.06 dB	-36.8 dBsm	-36.0 dBsm
2°	7.10 ± 0.13 dB	8.46 ± 0.43 dB	-32.5 dBsm	-31.5 dBsm

As expected, a misalignment in the tilted dihedral has severe consequences in the calibration. However, this calibration object does calibrate all four polarization channels rather well, offering a cross-polarization isolation of about 28 dB with a nominal 0° misalignment. This value can be obtained approximately by taking the co-polar RCS of the sphere in the region of 13-14 GHz (about -11 dBsm) and subtracting the cross-polarized levels (about -39 dBsm). It is worthy to note that the HH-polarization error in the calibration of Table 4 is consistently higher than the VV-polarization error. This is most likely due to errors in the MoM simulation of the dihedral.

5.11 EMSL Simple Polarimetric Calibration Technique

The first object set used for the analysis of this calibration is the typical set used in the EMSL procedure. For the co-polar amplitude reference object (Object 1), the small disk is used. For the cross-polar reference objects (Objects 2 and 3, respectively), the wire mesh is used in the vertical orientation and subsequently with the wires aligned 45° counter-clockwise from vertical. The next table displays the results of the calibration error analysis for this object set.

Table 5: Error statistics for EMSL calibration (T1: small disk, T2: vertical wire mesh, T3: tilted wire mesh)

<u>Object Misalignment</u>	<u>VV-error</u>	<u>HH-error</u>	<u>VH level</u>	<u>HV level</u>
$T1=0^\circ, T2=0^\circ, T3=0^\circ$	0.17 ± 0.01 dB	0.10 ± 0.01 dB	-42.0 dBsm	-42.0 dBsm
$T1=1^\circ, T2=1^\circ, T3=1^\circ$	0.32 ± 0.04 dB	0.35 ± 0.01 dB	-41.4 dBsm	-41.4 dBsm
$T1=2^\circ, T2=0^\circ, T3=0^\circ$	1.24 ± 0.04 dB	1.28 ± 0.01 dB	-40.8 dBsm	-40.8 dBsm
$T1=0^\circ, T2=2^\circ, T3=0^\circ$	0.17 ± 0.01 dB	0.10 ± 0.01 dB	-43.7 dBsm	-43.7 dBsm
$T1=0^\circ, T2=0^\circ, T3=2^\circ$	0.17 ± 0.01 dB	0.10 ± 0.01 dB	-39.7 dBsm	-39.7 dBsm
$T1=0^\circ, T2=2^\circ, T3=2^\circ$	0.17 ± 0.01 dB	0.10 ± 0.01 dB	-41.3 dBsm	-41.4 dBsm
$T1=2^\circ, T2=2^\circ, T3=2^\circ$	1.24 ± 0.04 dB	1.28 ± 0.01 dB	-40.1 dBsm	-40.2 dBsm

For the “perfect” alignment of the calibration objects, the Simple Polarimetric calibration offers a cross-polarization isolation of about 3 dB more than the Type-1 calibration shown in Table 4 (-42 dBsm compared with -39 dBsm cross-polarization RCS levels).

For the Type-2 calibration as performed in the EMSL, the object set used in Table 5 is the only appropriate set that can be used. The wire mesh is the only known object to return high cross-polarized RCS that is strongly correlated with the co-polar RCS (approximated by a \cos^2 relationship) at a bistatic angle of more than 2° . The small disk, though very sensitive to alignment, returns the largest bistatic co-polar RCS of any object, which reduces the signal-to-noise ratio in the calibration. The EMSL technique could be modified, however, to use the tilted dihedral as a cross-polarization reference object, if the calibration routine is adjusted to use a MoM prediction rather than an approximate prediction based on the vertical wire mesh. This would eliminate one object in the calibration—only the small disk and the tilted dihedral (in a single orientation) would need to be used.

Table 6: Error statistics for modified EMSL calibration (T1: small disk, T2: dihedral tilted 22.5°)

<u>Object Misalignment</u>	<u>VV-error</u>	<u>HH-error</u>	<u>VH level</u>	<u>HV level</u>
$T1=0^\circ, T2=0^\circ$	0.17 ± 0.01 dB	0.10 ± 0.01 dB	-39.3 dBsm	-38.7 dBsm
$T1=1^\circ, T2=1^\circ$	0.32 ± 0.04 dB	0.35 ± 0.01 dB	-36.8 dBsm	-36.0 dBsm
$T1=2^\circ, T2=0^\circ$	1.24 ± 0.04 dB	1.28 ± 0.01 dB	-39.3 dBsm	-38.7 dBsm
$T1=0^\circ, T2=2^\circ$	0.17 ± 0.01 dB	0.10 ± 0.01 dB	-32.5 dBsm	-31.5 dBsm
$T1=2^\circ, T2=2^\circ$	1.24 ± 0.04 dB	1.28 ± 0.01 dB	-40.1 dBsm	-40.2 dBsm

As seen from Table 6, the cross-polarization isolation is about 3 dB less than that of the normal EMSL calibration (Table 5), and the co-polarized RCS error is identical. This degradation is weighed against the advantage of measuring one less calibration object. In effect, this modified Type-2 calibration is identical in procedure to a Type-1 calibration, with the exception that two objects are used: one for co-polar amplitude calibration, and the other for cross-polar amplitude calibration. Comparing this calibration with the Type-1 using the tilted dihedral (Table 4) one observes that the use of the disk enhances the co-polarized RCS error, while the cross-polarization isolation is the same.

5.12 Generalized Dual-Antenna Calibration Technique

This technique (abbreviated as the GCT in (Whitt, et al, 1991),) was expected to yield the best results for ideal alignment conditions and given accurate theoretical solutions. The effect of misalignment of one or more of the reference objects, however, was unknown. Figure 36 displays the co-polarized error in a measurement of the metallic sphere calibrated with the GCT, using what is considered to be a near-optimal object set—the three objects used were the small disk (object 1), the vertical dihedral (object 2), and the dihedral tilted at 22.5° from vertical (object 3). The scattering matrices for each of these objects have the form:

$$\mathbf{T}_1 = \begin{bmatrix} 1 & 0 \\ 0 & 1 \end{bmatrix} \quad (56)$$

$$\mathbf{T}_2 = \begin{bmatrix} -1 & 0 \\ 0 & 1 \end{bmatrix} \quad (57)$$

$$\mathbf{T}_3 = \begin{bmatrix} -1 & -1 \\ -1 & 1 \end{bmatrix} \quad (58)$$

Every scattering matrix meets the requirement of mutual linear independence.

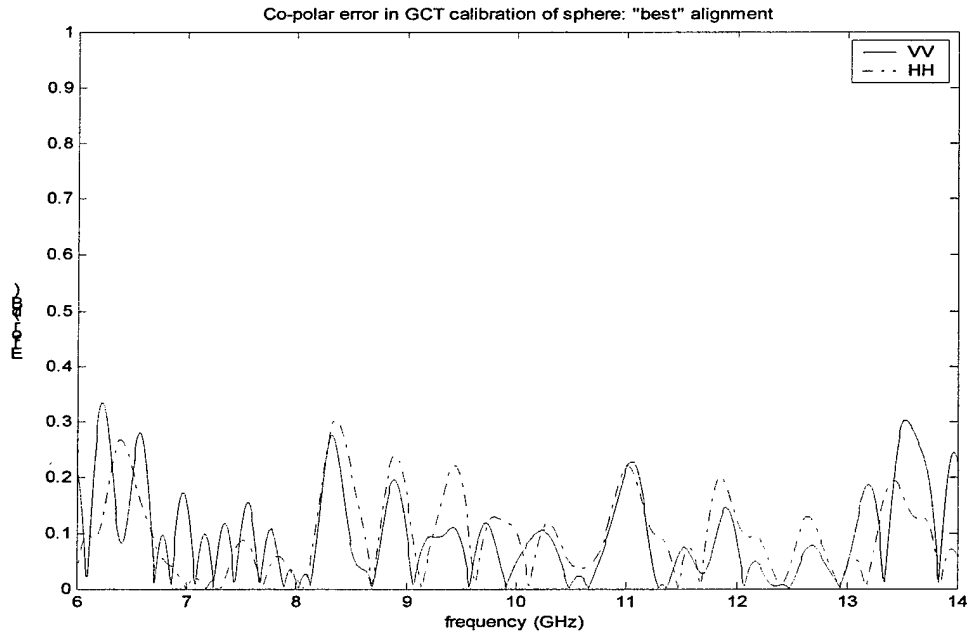


Figure 36: Error in GCT calibration using small disk, vertical, and tilted dihedral

For this calibration, the theoretical prediction for the small disk was approximated with PO, and the predictions for the dihedral was generated using an MoM code, for which the scattering geometry in the simulation reflected the true geometry of the dual-sled measurement in the EMSL.

Using the same object set, but with a systematic misalignment of 2° , the following error versus frequency plot was generated:

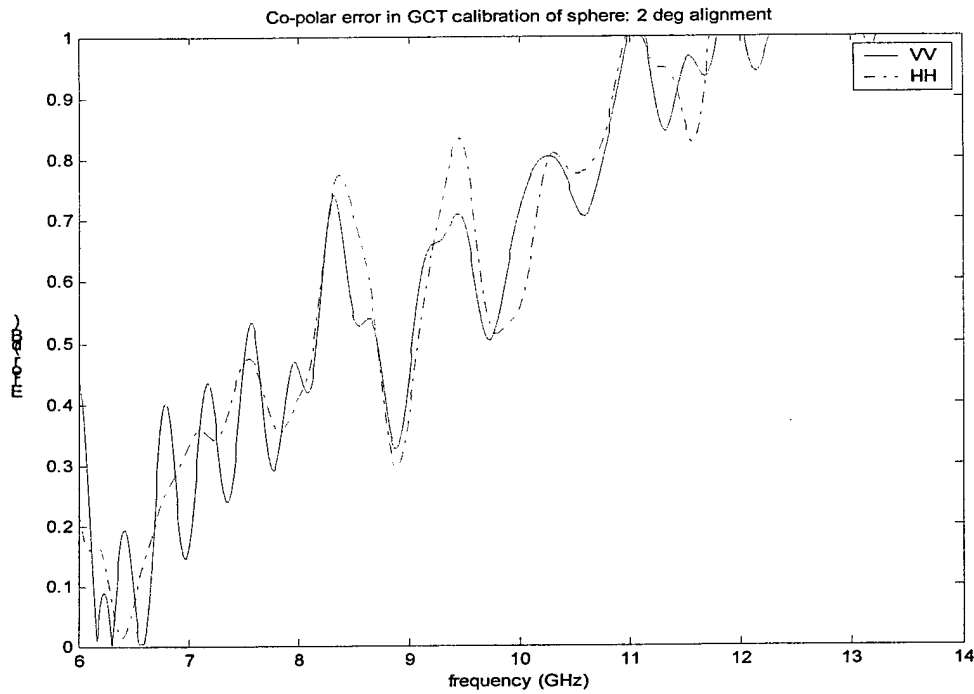


Figure 37: Error in GCT calibration with 2° misalignment associated with each reference object

As one might expect, when misalignment is introduced into the calibration, the calibrated measurement will tend to overestimate the true prediction, and the overestimation will increase with frequency. Table 7 displays the mean and variance of the RCS error between the calibrated measurements and the prediction of the sphere. These statistics are performed only on the highest 1 GHz band of the measurement bandwidth (13-14 GHz) in order to highlight the effect of misalignment on higher frequencies.

Table 7: Average alignment error statistics for GCT calibration (T1: small disk, T2: vertical dihedral, T3: tilted dihedral)

<u>Object Misalignment</u>	<u>VV-error</u>	<u>HH-error</u>	<u>VH level</u>	<u>HV level</u>
$T1=0^\circ, T2=0^\circ, T3=0^\circ$	0.17 ± 0.01 dB	0.10 ± 0.03 dB	-49.2 dBsm	-51.5 dBsm
$T1=1^\circ, T2=1^\circ, T3=1^\circ$	0.32 ± 0.04 dB	0.35 ± 0.01 dB	-48.8 dBsm	-51.5 dBsm
$T1=2^\circ, T2=0^\circ, T3=0^\circ$	1.24 ± 0.04 dB	1.28 ± 0.01 dB	-47.8 dBsm	-50.6 dBsm
$T1=0^\circ, T2=2^\circ, T3=0^\circ$	0.17 ± 0.01 dB	0.10 ± 0.01 dB	-49.2 dBsm	-51.4 dBsm
$T1=0^\circ, T2=0^\circ, T3=2^\circ$	0.17 ± 0.01 dB	0.10 ± 0.01 dB	-49.2 dBsm	-51.5 dBsm
$T1=0^\circ, T2=2^\circ, T3=2^\circ$	0.17 ± 0.01 dB	0.10 ± 0.01 dB	-49.2 dBsm	-51.4 dBsm
$T1=2^\circ, T2=2^\circ, T3=2^\circ$	1.24 ± 0.04 dB	1.27 ± 0.01 dB	-47.8 dBsm	-50.5 dBsm

The cross-polarization isolation for this case is 10 dB greater than the Type-1 calibration (Table 4) and about 7 dB greater than the Simple Polarimetric Calibration (Table 5). If the object set is re-ordered, so that the vertical dihedral is now T_1 , the tilted dihedral is T_2 , and the small disk is T_3 , the following error statistics result:

Table 8: Error statistics for GCT calibration (T1: tilted dihedral, T2: small disk, T3: vertical dihedral)

<u>Object Misalignment</u>	<u>VV-error</u>	<u>HH-error</u>	<u>VH level</u>	<u>HV level</u>
$T1=0^\circ, T2=0^\circ, T3=0^\circ$	0.24 ± 0.02 dB	-0.06 ± 0.02 dB	-33.9 dBsm	-51.6 dBsm
$T1=1^\circ, T2=1^\circ, T3=1^\circ$	-0.44 ± 0.03 dB	-0.73 ± 0.03 dB	-30.6 dBsm	-51.3 dBsm
$T1=2^\circ, T2=0^\circ, T3=0^\circ$	0.24 ± 0.02 dB	-0.06 ± 0.02 dB	-33.7 dBsm	-51.9 dBsm
$T1=0^\circ, T2=2^\circ, T3=0^\circ$	-2.76 ± 0.06 dB	-3.05 ± 0.06 dB	-28.8 dBsm	-48.6 dBsm
$T1=0^\circ, T2=0^\circ, T3=2^\circ$	0.22 ± 0.03 dB	-0.08 ± 0.02 dB	-28.3 dBsm	-51.4 dBsm
$T1=2^\circ, T2=0^\circ, T3=2^\circ$	0.22 ± 0.03 dB	-0.08 ± 0.02 dB	-28.4 dBsm	-51.7 dBsm
$T1=2^\circ, T2=2^\circ, T3=2^\circ$	-2.77 ± 0.07 dB	-3.07 ± 0.07 dB	-25.1 dBsm	-48.7 dBsm

The cross-polar levels are (specifically, of the VH-channel) are considerably lower for the calibration of Table 7. Realizing this, as well as observing that the penalty resulting from the misalignment of T_2 in Table 8 is more than twice the penalty of the misalignment of T_1 in Table 7, it is apparent that though the objects sets are identical, the

order in which the objects are implemented in the calibration is important. Only Object 1 is used in the absolute amplitude calibration in the GCT method. Therefore for any given object set, the most accurate calibration will be that one which uses the object that has the most precise theoretical prediction and uses it as Object 1. In this case, the most precise prediction accompanied the small disk, and as a result, the first calibration (Table 7) used the disk as Object 1 and, as a result, was most accurate.

For the measurement of the metallic sphere, good cross-polarization isolation will be demonstrated in very low cross-polarized RCS levels. The first calibration represents the better cross-polarization isolation. In order to optimize the cross-polar isolation in the measurement, one must determine which of objects 2 and 3 have the most precise prediction, and which of Eqn's (36) and (39) should be used in the calibration routine to offer the best cross-polarization isolation.

5.13 BICOMS Full-Polarimetric Calibration Technique

The BICOMS technique is a modified implementation of the GCT. This method solves for the monostatic subsystem distortion characteristics of each leg of the bistatic measurement path, and uses this complete distortion model to solve for the distortion along the whole bistatic path. Since the PDM's of the antennae are solved for using monostatic measurements, it is not necessary to address the difficult problem of finding a bistatic cross-polarization calibration reference object. This also means, though, that more calibration measurements must be taken, and the operational efficiency of the measurement facility is affected.

Four objects are used for the analysis of this calibration. In the actual BICOMS procedure, a short cylinder is used as one of the three calibration reference objects that determine the system distortion, and the same cylinder is also rotated 90° , and the end-cap of the cylinder is measured to obtain an absolute amplitude/phase correction. The remaining two calibration objects are a horizontal dihedral, and a dihedral oriented 67.5° from horizontal. In the interest of consistency with the calibrations of the previous section, this analysis uses a vertical dihedral and a dihedral oriented 22.5° from vertical. This does not have any bearing on the performance of the calibration. Table 9 lists the error statistics for this particular calibration. The cross-polarization isolation achieved with this calibration is similar to that achieved in the optimum GCT calibration (Table 7).

Table 9: Error statistics for BICOMS calibration (T0: small disk, T1: short cylinder, T2: tilted dihedral, T3: vertical dihedral)

<u>Object Misalignment</u>	<u>VV-error</u>	<u>HH-error</u>	<u>VH level</u>	<u>HV level</u>
$T0=0^\circ, T1=0^\circ, T2=0^\circ, T3=0^\circ$	0.12 ± 0.03 dB	-0.06 ± 0.01 dB	-47.0 dBsm	-49.9 dBsm
$T0=1^\circ, T1=0^\circ, T2=0^\circ, T3=0^\circ$	-0.17 ± 0.04 dB	-0.34 ± 0.01 dB	-46.7 dBsm	-49.6 dBsm
$T0=2^\circ, T1=0^\circ, T2=0^\circ, T3=0^\circ$	-1.09 ± 0.04 dB	-1.26 ± 0.01 dB	-45.8 dBsm	-48.7 dBsm
$T0=0^\circ, T1=1^\circ, T2=1^\circ, T3=1^\circ$	0.08 ± 0.02 dB	-0.06 ± 0.01 dB	-45.7 dBsm	-51.0 dBsm
$T0=0^\circ, T1=2^\circ, T2=2^\circ, T3=2^\circ$	0.17 ± 0.02 dB	-0.06 ± 0.01 dB	-45.7 dBsm	-50.6 dBsm

Objects T1-T3 are all monostatic measurements that characterize the polarimetric distortion involved in each leg of the bistatic path. Since objects T1-T3 are used only to solve for the PDM's and not the absolute amplitude of the calibrated data, they need not necessarily be accompanied by a precise MoM prediction. If the scattering matrix structure of these objects is known (which it is, according to Eqn's (56) - (58), these

simple binary matrices can be used in place of the theoretical prediction. The only object that needs an exact prediction is the amplitude reference object ($T0$). The calibration implementation shown in Table 9 was performed in this manner with near-identical results.

6 CONCLUSIONS

6.1 Calibration Object Selection

It has been shown that the sensitivity of a particular calibration object to alignment error, though significantly affecting the error in the absolute amplitude calibration, has a less pronounced effect in the determination of the associated antenna PDM's. This has been demonstrated with the wire mesh and dihedral specifically, where a 2° misalignment in these objects affects a loss in cross-polarization isolation of about 2 dB.

For full-polarimetric (Type-3) calibration, it is also clear that selecting an object with a simple scattering matrix offers great advantages in the way of computational efficiency and accuracy. Binary scattering matrix structures, such as the vertical dihedral, sphere, and disk (among many others) offer the capability to predict the antenna PDM's more precisely than if these objects were predicted with a complex computational method, such as MoM. In the amplitude correction of a Type-3 calibration, the same considerations apply as to that of a Type-1 calibration: namely that objects with high RCS and are simultaneously insensitive to alignment error are optimal.

It has further been shown that the parallel wire mesh offers promise as a versatile bistatic cross-polarization calibration reference object. It offers high cross-polarization RCS at a much greater bistatic angular range than any other object evaluated here. Further investigation into the suitability of this object for a polarimetric calibration would include:

- Finding accurate predictions for the mesh using a numerical electromagnetic code (NEC),

- Exploring the optimum structure of the mesh, considering variables such as wire length and spacing, and selection of the foam mounting substrate,
- The bistatic angular range at which the wire mesh gives good cross-polarization isolation in a Type-2 or Type-3 calibration,
- The effect of segmenting the wire mesh in order to mitigate traveling wave and grating lobe effects in the RCS return.

6.2 Performance of Type-1, Type-2, and Type-3 Calibrations

For the measurement parameters of the EMSL (antenna polarization purity, gain, signal-to-noise ratio, etc), it has been shown that the gain in cross-polarization isolation in using a Type-3 technique as opposed to a Type-1 technique is about 10 dB. The absolute error in the co-polar channels is comparable between comparisons, provided that the alignment error and signal-to-noise ratio are kept relatively constant. In general, for any type of calibration, the sources of absolute amplitude error and degradation of cross-polarization isolation are separate. Each calibration technique evaluated here follows the general paradigm that two objects with highly independent scattering matrices are necessary to characterize polarization distortion, and a single object with high co-polar RCS is necessary to accurately determine the amplitude and phase constant applied to these PDMs.

Given any particular calibration object, such as those listed in Table 1, it is not difficult to predict the effect of misalignment on the overall error of the calibration. There is a 1:1 correspondence between the dB error per degree of misalignment, and the average amplitude error of the co-polar channels in the calibration.

These results offer fair insight into the capabilities of these various types of calibrations relative to each other. However, the results are only applicable in the context

of the EMSL measurement environment. Further study into this subject should include a similar analysis in varying measurement environments.

APPENDIX A: VALIDATION OF MBETs AND MoM COMPUTATIONS

In order to experimentally validate the accuracy of the MoM computations performed on the Fast-Illinois Solver Code (FISC), a single-frequency study was done for two objects: one simple object and another rigorously complex object, consisting of an assembly of canonical shapes, including a corner reflector, open and closed cylinders, and a shadowing plate. In addition, Falconer's monostatic-to-bistatic scattering conversion formulae for far-field and near-field, (Falconer, "Extrapolation of...", 1988) and (Falconer, "Near-Field Statement...", 1988), are evaluated for their ability to predict bistatic scattering phenomena.

6.3 MBET Theory

Kell's commonly cited MBET (Kell, 1965) relates the bistatic RCS of a point scatterer to its monostatic RCS at the bisector of the bistatic angle and at a reduced frequency. Kell's MBET is stated as:

$$\sigma_B(\theta_T, \theta_R, f) \cong \sigma_M \left(\theta = \left(\frac{\theta_T + \theta_R}{2} \right), f_M = f \cos \left(\frac{\theta_T - \theta_R}{2} \right) \right) \quad (59)$$

where

σ_B = Estimated Bistatic RCS in dBsm

σ_M = Monostatic RCS in dBsm

θ = Equivalent Monostatic Azimuth Angle

θ_R = Bistatic Receiver Azimuth Angle

θ_T = Bistatic Transmitter Azimuth Angle

f = Transmitter Frequency

f_M = Equivalent Monostatic Frequency

Based on the Physical Optics (PO) model for bistatic scattering of point scatterers at small bistatic angles, the equivalent monostatic illumination angle is approximated by the bisector of the bistatic angle of the measurement.

By modeling the object as a set of discrete scattering centers, Kell states that if for any given aspect angle, the amplitude and phase of the scattering centers are insensitive to the bistatic angle β over the range of interest, then the monostatic cross-section measured at the bisector of the bistatic angle and at a frequency lower by a factor of $\cos(\beta/2)$ is equal to the bistatic cross-section.

The range of angles at which this assumption is valid is dependent upon the object's geometry. Classes of objects for which specular reflection is the dominant scattering mechanism are best suited to this approximation. The maximum bistatic angle for which the approximation is valid is also highly dependent on the beamwidth of the pattern of the dominant scattering centers.

Another commonly cited MBET, developed by Crispin (Crispin and Siegel, 1968), is similar to Kell's, but simplified to exclude the adjustment of the monostatic equivalent frequency.

$$\sigma_s(\theta_r, \theta_s, f) \cong \sigma_m\left(\theta = \left(\frac{\theta_r + \theta_s}{2}\right), f\right) \quad (60)$$

The advantage of this expression of the MBET can be immediately seen in that it requires no RCS measurements at frequencies different from the bistatic measurement.

Falconer's adaptation to the above theorems arrives at a different relationship between the bistatic angle and equivalent monostatic aspect angle. Falconer's theorem states:

$$\sigma_B(\theta_T, \theta_R, f) \cong \sigma_M\left(\theta = \arcsin\left(\frac{\sin(\theta_T) + \sin(\theta_R)}{2}\right), f\right) \quad (61)$$

The above MBET is actually valid in both the near and far-fields. Falconer's MBET, similar to Crispin's, approximates the bistatic return by using the monostatic signal at the same transmission frequency but at a reduced look angle. While the structure of the formula appears similar to Crispin's formulation of the MBET, Falconer employed the discrete scattering center model of the object's radiation pattern for his formulation, the same formulation that resulted in Kell's MBET.

This work focuses on a near-field MBET derived by Falconer and based on a similar theorem stated by Kell. To arrive at the MBET, the vector potential is written in scalar form by approximating the scattering surface to be planar and the angles defining the bistatic path to be paraxial, i.e.

$$A(x_r) = \int J(x)G(x, x_r)dx \quad (62)$$

where $A(x_r)$ is the vector potential observed at the point x_r , induced by the current $J(x)$, and $G(x, x_r)$ is the Green's function for the particular medium and frequency.

The magnetic field incident upon the surface can be written as

$$H(x) = H_0 e^{ikr'} \quad (63)$$

where $r' = |x - x_t|$ and x_t is the location of the transmitting antenna.

The Physical Optics current is

$$J(x) = 2H_0 T(x) e^{ikr'} \quad (64)$$

where $T(x)$ is the complex reflectivity of the scatterer, assumed to be relatively independent of frequency.

This is then substituted into the vector potential yielding

$$A(x_r) = 2H_0 \int T(x) e^{ikr'} G(x, x_r) dx \quad (65)$$

The vector potential is related to the E-field by

$$E = -120\pi k A \quad (66)$$

in free space. The E-field at the observation point then becomes

$$E(x_r) = E_0 \int \frac{(-i/\lambda r) T(x) e^{ikr'} e^{ikr}}{4\pi r} dx \quad (67)$$

which for the two dimensional case becomes

$$E(x_r) = E_0 \int \frac{\sqrt{-i/\lambda r} T(x) e^{ikr'} e^{ikr}}{4\pi r} dx \quad (68)$$

The Green's function is approximated with a Fresnel phase approximation for each of the near-field and far-field cases. For the near-field (valid when $0.6(D^3/\lambda)^{1/2} \leq R \leq 2D^2/\lambda$) is

$$r \approx R - x \sin \theta_r - z \cos \theta_r + (x^2 + z^2)/2R \quad (69)$$

and for the far-field (when $R \geq 2D^2/\lambda$),

$$r \approx R - x \sin \theta_r - z \cos \theta_r \quad (70)$$

The above expressions are inserted into the Green's function $\exp(ikr/4\pi r)$ in the numerator of the exponent, and the denominator is approximated by $4\pi r \approx 4\pi R$.

The scalar near-field scattering amplitude can now be expressed as

$$\begin{aligned}
E_b(\theta_r, \theta_i, k, R) &= E_0 \sqrt{-i / \lambda R} e^{i2kR} \int T(x, z) \\
&\bullet \exp[ik(x^2 + z^2) / R - ikx(\sin \theta_r + \sin \theta_i) \\
&- ikz(\cos \theta_r + \cos \theta_i)] dx
\end{aligned} \tag{71}$$

In the development of the near-field MBET (heretofore designated as F2) from the above expression, the exponent is simplified using trigonometric identities, and the reduced monostatic frequency defined by Kell ($k' = k \cos \theta_{1/2}$), where $\theta_{1/2}$ is half the bistatic angle. In addition, Falconer introduces a reduced range $R' = R \cos \theta_{1/2}$. The monostatic amplitude is observed at these reduced frequency and range parameters that altogether yields the scattering amplitude of the following form, where $\theta = \theta_r = \theta_i$:

$$\begin{aligned}
E_m(\theta_r, \theta_i, k', R') &= E_0 \sqrt{-i / \lambda' R'} e^{i2k'R'} \int T(x, z) \\
&\bullet \exp[ik'(x^2 + z^2) / R' - i2k'x \sin \theta - i2k'z \cos \theta] dx
\end{aligned} \tag{72}$$

Recognizing that $\lambda' R' = \lambda R$ and $k' / R' = k / R$, we get

$$\begin{aligned}
E_m(\theta, k', R') &= E_0 \sqrt{-i / \lambda R} e^{i2k'R'} \int T(x, z) \\
&\bullet \exp[ik(x^2 + z^2) / R - i2k'x(\sin \theta + \cos \theta)] dx
\end{aligned} \tag{73}$$

A comparison of this monostatic scattering amplitude to the bistatic scattering amplitude reveals a relationship defined by:

$$E_b(\theta_r, \theta_t, k, R) = e^{i2kR - ik'R'} E_m(\theta_a; k', R') \quad (74)$$

where θ_a is the bisector of the bistatic angle ($\theta_a = (\theta_r + \theta_t)/2$). This is the expression for Falconer's near-field MBET, which requires adjustment of the monostatic frequency and range in order to approximate the bistatic cross-section.

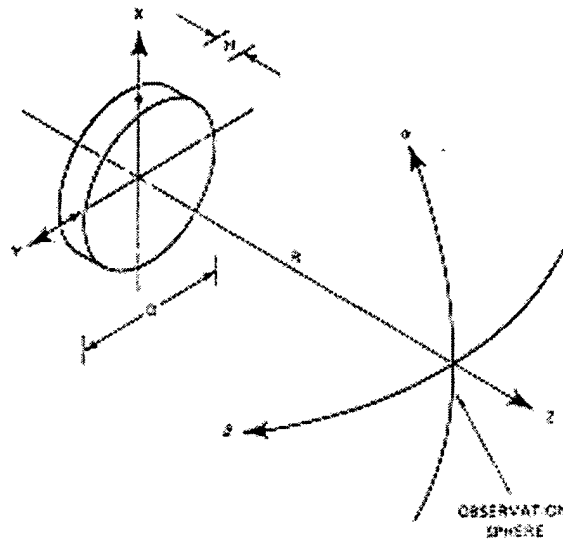


Figure 38: Falconer's MBET geometry. R is observation sphere radius, α and β observation angles, both presumed small, D represents object's nominal diameter, and H its nominal height relative to the illumination direction. (Falconer, "Extrapolation of...", 1988)

Substituting the appropriate expressions for k' and R' , Falconer's extended near-field MBET (F2) is stated completely in terms of frequency and range by:

$$E_B(\theta_T, \theta_R, f, R) \cong e^{ikR \left(2 - \cos^2 \left(\frac{\theta_T - \theta_R}{2} \right) \right)} E_M(\theta, f_M, R_M) \quad (75)$$

where

$$\theta = \left(\frac{\theta_r + \theta_R}{2} \right), \text{ Monostatic Angle}$$

$$f_M = f \cos \left(\frac{\theta_r - \theta_R}{2} \right), \text{ Reduced frequency}$$

$$R_M = R \cos \left(\frac{\theta_r - \theta_R}{2} \right), \text{ Reduced Range}$$

Falconer's CW version of the F2 MBET is valid for both near field and far field scenarios. A different angle parameter, θ_f is introduced which is defined as

$$\sin \theta_f = \frac{\sin \theta_r + \sin \theta_i}{2} \quad (76)$$

and the original relationship between the bistatic and monostatic scattered fields is

$$\begin{aligned} E_b(\theta_r, \theta_i, k, R) &= E_0 \sqrt{-i / \lambda R} e^{i2kR} \int T(x, z) \\ &\bullet \exp[ik(x^2 + z^2) / R - i2kx \sin \theta_f \\ &- i2kz(\cos \theta_r + \cos \theta_i)] dx \end{aligned} \quad (77)$$

If θ_r and θ_i are small, then

$$\cos \theta_f \approx \cos \theta_r \approx \cos \theta_i = 1 \quad (78)$$

and it follows that

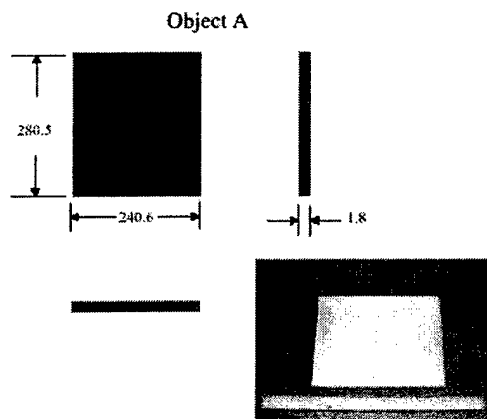
$$E_b(\theta_r, \theta_i, k, R) = E_m(\theta_f; k, R) \quad (79)$$

Therefore the frequency and range of the bistatic measurement are the same as the monostatic equivalent for small bistatic angles. We designate this MBET as F1.

The region of applicability of Falconer's CW MBET is restricted by the object's nominal thickness at the desired observation angle. As seen in Figure 38, the thickness H is defined as the linear extent of the object in the direction of the observation angle. It is appropriate to apply the CW MBET when the bistatic angle satisfies $\theta_b \leq \sqrt{\lambda / H}$.

6.4 Methodology

The following presents a five phased research project consisting of: 1) the collection of far-field empirical data, 2) the evaluation of Falconer's far-field MBET with the empirical data, 3) the validation of the computer prediction code with empirical data, 4) the generation of near-field and far-field scattering with the computer code, and 5) the evaluation of both Falconer's MBETs with computer generated scattering data. Objects A and B, shown in Figure 2, were chosen for their ability to highlight various scattering phenomena at different look angles, such as traveling waves, creeping waves, multi-bounce, and shadowing effects. Co-polarized (VV, HH) monostatic and bistatic waterline pattern cut and imaging data was collected according to the matrix in Table 1 at the European Microwave Signature Laboratory (EMSL) of the EC Joint Research Center in Ispra, Italy.



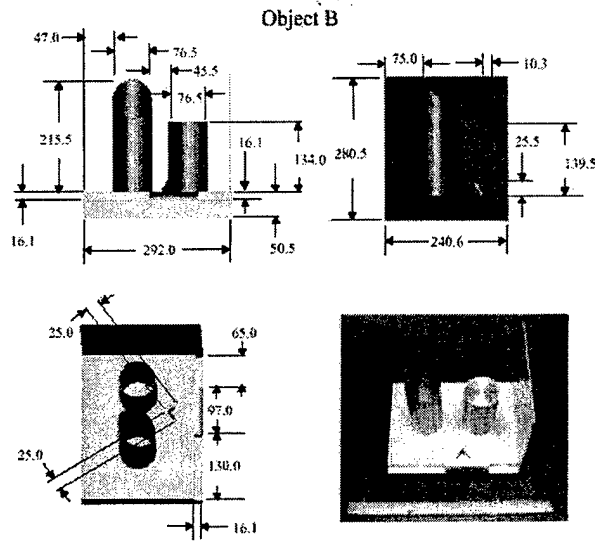


Figure 39: Test Objects (dimensions in mm) (Eigel, 1999)

Table 10: Bistatic RCS Measurement

Object	RF (GHz)	TX illumination aspect angle (deg)	Rx look angle (deg)
A	7 – 15	0	0 – 180
B	7 - 15	45	-20 – 225

For the purposes of this chapter, all measurements and analysis occur in the horizontal (x - y) plane defined relative to the measurement object. Specifically, a Cartesian coordinate system is defined such that the z -axis is tangent to the long flat plate dimension of object A and the cylinder axes of object B. The x -axis is then defined to be the plate normal of objects A and B, where the normal points away from the cylinders in object B. The bistatic arrangement is defined by the transmitter illumination angle, θ_T , and receiver look angle, θ_R , where these are restricted to the (x - y) plane (i.e. $\theta = 90^\circ$ in spherical coordinates). Therefore, the bistatic angle becomes $\theta_T - \theta_R$. Polarization is defined by the E-field vector orientation. For example, VV-polarization indicates both the incident and scattered E-field polarizations are z directed. Similarly, HH-polarization

indicates the E-field vectors lie in the (x-y) plane and are orthogonal to the propagation direction. Only co-polarized data is analyzed in this report (i.e., same transmit and receive polarizations). No measured bistatic data exists for θ_R angles within 4° of the θ_T angle. In the azimuth plane, bistatic estimated data is generated from the monostatic far field measurements through Falconer's CW monostatic-to-bistatic equivalence theorem given by (Falconer, "Near-Field Statement of...", 1988).

Simulation data are generated for the far-field and near-field test set by commercially available electromagnetic field modeling code which computes scattering from an object using the method of moments (MoM).

6.5 Results

6.5.1 Far-field MoM code and MBET evaluation

As an initial validation of the scattering code and the MBETs, a bistatic measurement of Object A with the transmitter positioned at zero degrees of azimuth and elevation was compared with the MoM simulation and also plotted against the MBET approximations.

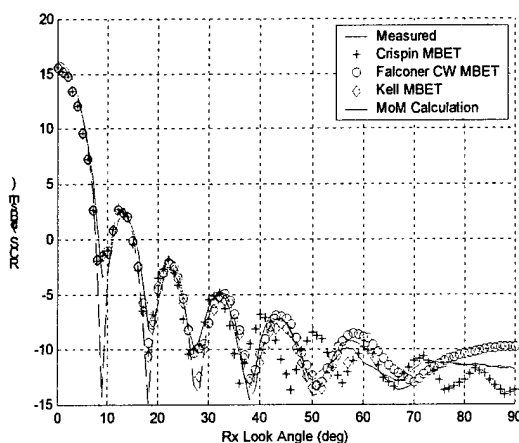


Figure 40: Object A Measured vs. Predicted Bistatic RCS, VV Polarization, 8 HGz, 0° Transmit Angle

Figure 40 shows excellent agreement between the measurements and MoM simulation data. While all MBETs perform well up to about a 30° bistatic angle, Kell's and Falconer's CW MBET (F1) show continued agreement out to about 55°. Note that Kell's MBET is limited by the frequency of the monostatic data collected.

6.5.2 Near-field MBET evaluation (fixed-angle bistatic RCS)

A primary region of interest for the evaluation of the near-field MBETs is the center of the radiating near-field. Location of objects in the middle of their radiating near field, defined in (Gabig et al, 2000), is governed by

$$0.62\sqrt{\frac{l^3}{\lambda}} \leq R \leq \frac{2l^2}{\lambda} \quad (80)$$

where λ refers to the transmitting signal's wavelength, and l designates the longest dimension of the object bisected by the waterline cut. For Object A, $l = 240\text{mm}$, and for Object B, $l = 380\text{mm}$. We analyzed the objects at 8 GHz, which is $\lambda = 37.5\text{mm}$. The variable R designates the limits of the near-field radiating region. Previously we calculated the bistatic return, and its corresponding monostatic return for Object B at the region R 's midpoint.

Maintaining a constant angular separation between the transmitter and receiver antenna of 10° and rotating this system around the object, we generated the data in Figure 4. This data illustrates reasonable null alignment between the computer generated near-field bistatic data and Falconer's F2 MBET approximation, where the main scattering mechanism is specular return from the flat shadowing plate. Additionally, the MBET

continues to track the nulls reasonably well after the transmitter passes 90° and begins illuminating more complex components of Object B.

The initial results obtained and illustrated in Figure 41 would tend to indicate that the F2 MBET performs well throughout a range of observation angles. To determine a more quantitative limit on the antenna separation that would produce results that are approximated well by the MBETs, we ran a series of near-field MOM simulations on both Objects A and B, for illumination angles of 0° , 45° , and 135° . The simulations focus again on the center of the near-field for both objects. For comparison, simulations for both objects were also taken in the far-field.

6.5.3 Near-field MBET evaluation (swept angle bistatic RCS)

Following are figures which display the RCS and phase errors between the bistatic

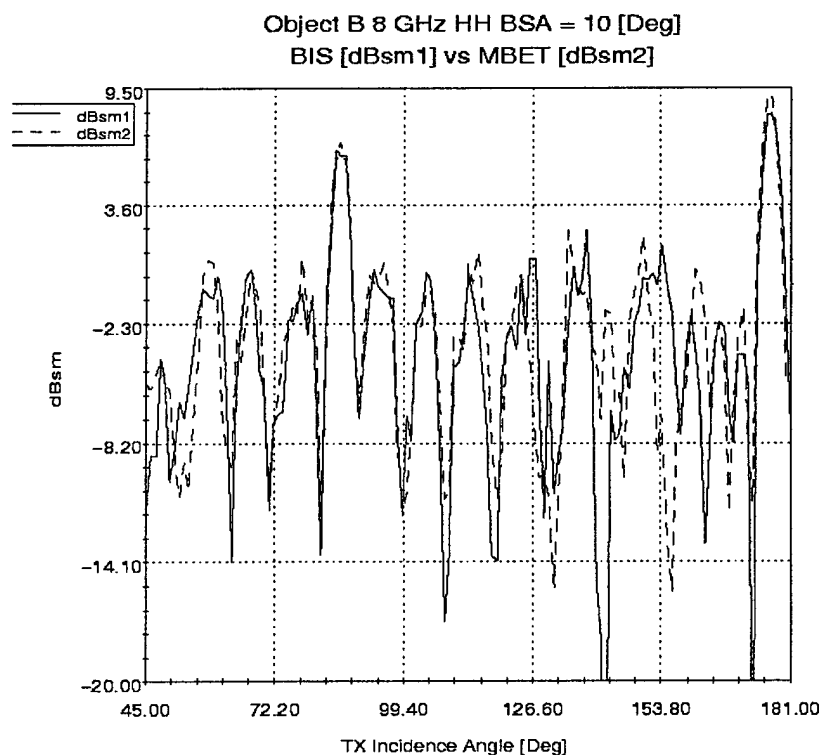


Figure 41: Object B MoM vs. F2 MBET Fixed Angle Bistatic RCS, HH Polarization, 8 GHz, 10° Bistatic Angle.

“truth” data generated by MOM and the F2 MBET approximation applied to monostatic data generated with the same software. The frequency and range parameters used in the monostatic calculations were adjusted corresponding to the appropriate values as determined by the F2 MBET and quantized to 11 levels (in order to save computational time). A sliding average window spanning 10° was applied to the error versus angle data in order to smooth the trend such that a stable threshold might be established. The threshold of tolerable error was taken to be ± 1 dB or $\pm 22.5^\circ$, corresponding to the error limits set forth in the development of the MBET itself.

For an incidence angle of zero degrees, as shown in Figure 5, one would expect the MBETs to perform similarly well for both objects, since the antenna illuminates no complex features. Non-specular effects largely shadowed in Object B, however, are seen to moderately limit the range of validity of both MBETs.

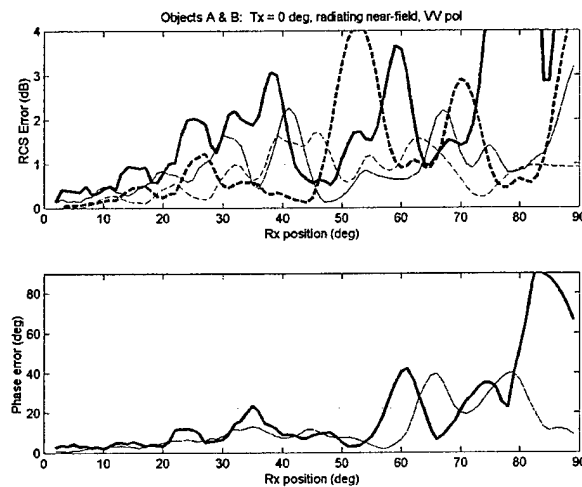


Figure 42: MBET error plot for a 0° transmitter angle. Thin line: Object A, Thick line: Object B. Dashed lines are for the F1 MBET and solid lines are for the F2 MBET.

For incidence angles that illuminate the complex features of Object B, such as 45° and 135° , shown in Figure 43 and Figure 44 respectively, both MBETs have an expected narrower region for which they are valid.

Table 11: Angular Size of Valid Regions for Each of Falconer's MBETs

MBET F1: far-field				MBET F2: radiating near-field		
Tx:	0°	45°	135°	0°	45°	135°
Object A	106°	180°	25°	19°	65°	71°
Object B	86°	19°	14°	8°	19°	9°

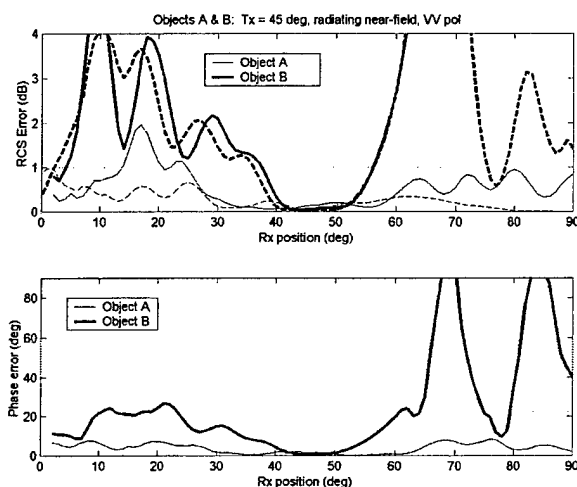


Figure 43: MBET error plot for a 45° transmitter angle.

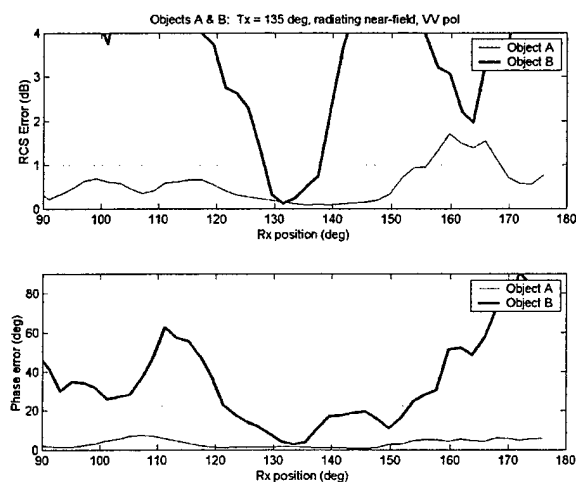


Figure 44: MBET error plot for a 135° transmitter angle.

The worst case for Falconer's near-field MBET is the case in which the complex features of Object B are illuminated fully which corresponds well to the illumination angle of 135° (Figure 44). From the figure the MBET will accurately predict the RCS in a region of less than 10° of antenna separation.

Following we present data that displays the RCS and phase error between the true bistatic MOM simulation and the F1 MBET approximation applied to the monostatic data. The same two objects are used, with identical antenna configurations, with the exception that all simulations are performed in the far-field.

Beyond the direct comparison with the data approximated by this MBET against the F2 MBET, it is interesting to note the incredibly good agreement between the truth and the approximation for Object A at 0° and 45° incidence as shown in Figure 45 and Figure 46. The phase error, also, tends to be very low in all cases using the F1 MBET.

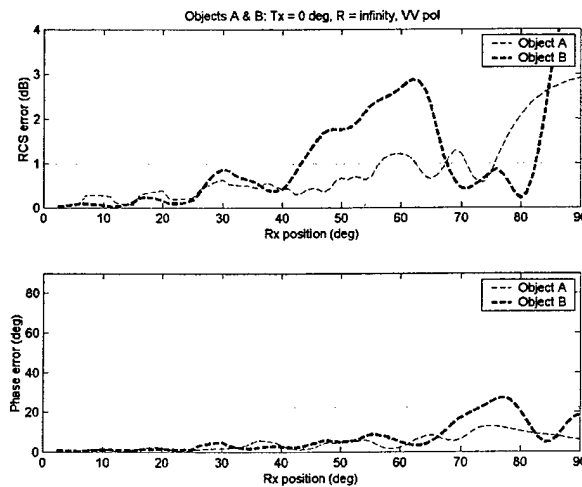


Figure 45: Falconer's F1 MBET error plot.

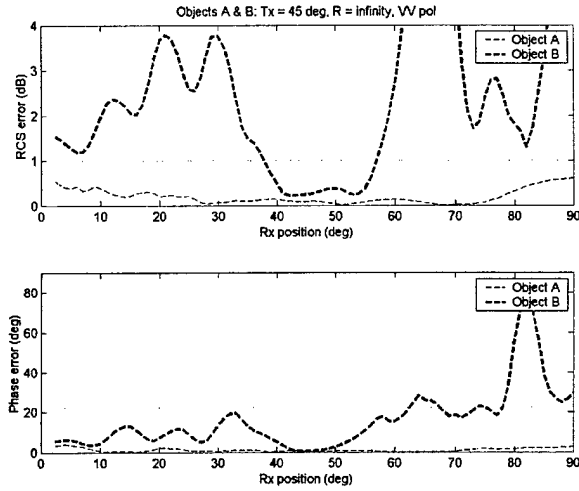


Figure 46: Falconer's F1 MBET error plot.

From these data, we can approximate the angular size of the valid regions for each of Falconer's MBETs based on the 1 dB and 22.5° criteria.

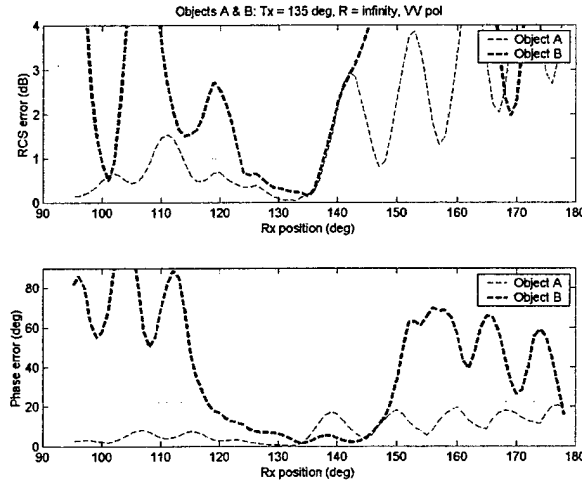


Figure 47: Falconer's F1 MBET error plot.

6.5.4 Near-field MBET evaluation (swept range bistatic RCS)

Finally, to evaluate the MBET error trends as a function of range, we plot the RCS error as a function of range for a 10° and 45° fixed bistatic angle. The ranges correspond to the radiating near field defined in equation (80) for each object.

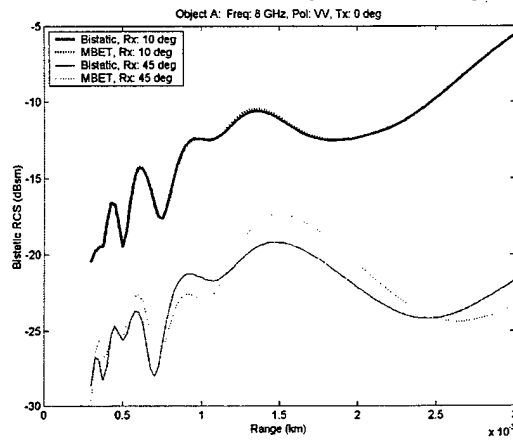


Figure 48: Object A MBET vs. MoM

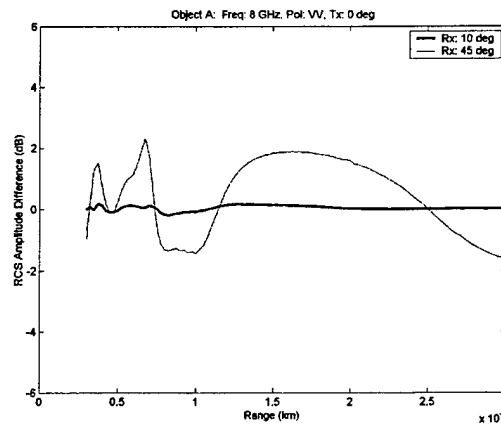


Figure 49: Object A range dependent error plot

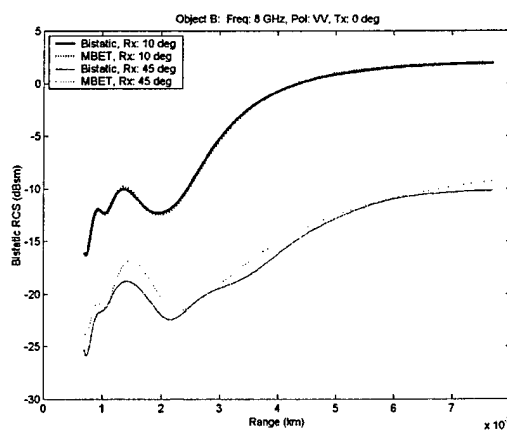


Figure 50: Object B MBET vs. MoM

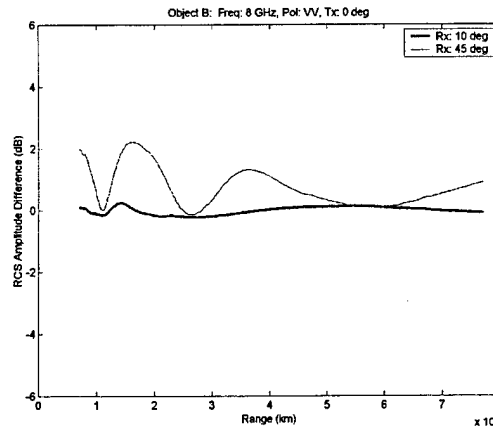


Figure 51: Object B range dependent error plot

6.5.5 Conclusions

These simulations have produced a good idea of the conditions for which Falconer's extended near-field and CW MBET are applicable. By varying the bistatic angle, range, and illuminated object's complexity, we can better understand at what point the MBETs, and consequently, the Physical Optics and discrete scattering center models fail to predict the monostatic cross-section given a bistatic reference measurement. Here it seems the F1 MBET performs better for the conditions presented, although an investigation into the performance of the F2 MBET under far-field conditions would be in order. The upper bound on magnitude error (1 dB) seems to be more restrictive than the phase bound, which would tend to mitigate the importance of the phase correction presented in F2.

It has been clearly shown that the complexity of the scatterer will severely restrict the region of validity for each MBET, where shadowing and multi-path interactions render the assumptions behind the theorems invalid. The wide disparity between the

agreement for Object A and Object B (Figure 46, for illumination angle of 45°) illustrates this point.

It is not known what effect the coarse quantization of the equivalent monostatic range and frequency values has on the F2 approximation. Further work will permit simulations utilizing more quantization levels in order to more closely represent the MBET.

Further MoM simulations are necessary in order to draw a clear conclusion regarding the maximum bistatic angle and object complexity for which the MBETs begin to break down. It has been clearly demonstrated that a complex object (Object B) is not well predicted by any MBET, whether the approximation is based on a scattering center model or Physical Optics model of the object. Where shadowing and multi-path effects are dominant, the errors involved in the prediction of a bistatic measurement by a monostatic measurement processed through a near-field or far-field MBET are great. Conversely, a simple object (Object A) which is well predicted by the Physical Optics and scattering centers model is likewise well-predicted by the MBET, even at bistatic angles greater than 90° .

Further work toward the end of characterizing these MBETs for their applicability in varying bistatic configurations would include extensive monostatic MoM simulations, with finely tuned range and frequency parameters, so that the effect of range and frequency adjustments in Falconer's MBET can be well understood. In addition, several objects with varying degrees of complexity based on the amount of shadowing and multi-path effects should be evaluated simultaneously.

APPENDIX B: MATLAB scripts

The following is a complete list of the MATLAB routines that were used in the processing of measured and theoretical data, as well as in performing the calibrations.

Where outside expertise was used in creating the function, appropriate credit is given.

```
%CAL_D Compute 4x4 calibration matrix (C) from the subtracted
calibration object
%files
%C = cal_d(disk,disk_diam_cm,meshvert,meshtilt)
%INPUTS:
%disk--2x2xn_freq scattering matrix of disk
%disk_diam_cm--diameter of disk in cm
%meshvert--2x2xn_freq scattering matrix of vertical mesh
%meshtilt--2x2xn_freq scattering matrix of tilted mesh
%f_start_GHz--start frequency in GHz
%f_stop_GHz--stop frequency in GHz
%OUTPUT:
%C--4x4xn_freq calibration coefficient matrix

function C = cal_d(M_disk,disk_diam_cm,M_meshvert,M_meshtilt)

global freq_start
global freq_stop
global n_freq
global n_ang
global C

if n_ang>1
    warning('Calibration files contain more than one angle--this routine
will utilize only the first')
    M_disk = squeeze(M_disk(:,:,:1));
    M_meshvert = squeeze(M_meshvert(:,:,:1));
    M_meshtilt = squeeze(M_meshtilt(:,:,:1));
else
    M_disk = squeeze(M_disk);
    M_meshvert = squeeze(M_meshvert);
    M_meshtilt = squeeze(M_meshtilt);
end

C = zeros(4,4,n_freq); %initialization of 4x4 diagonal distortion
matrix

%get PO prediction for calibration disk
S_disk = calcdisk(disk_diam_cm,freq_start,freq_stop,n_freq);

%calculate the co-polar calibration terms
C(1,1,:) = M_disk(1,1,:)./S_disk(1,1,:);
C(4,4,:) = M_disk(2,2,:)./S_disk(2,2,:);

%calculate the absolute magnitude of the vertical mesh
S_meshvert = zeros(2,2,n_freq);
```



```

S_meshvert(2,2,:) = M_meshvert(2,2,:)./C(4,4,:);

%calculate the absolute magnitude of the tilted mesh
S_meshtilt = zeros(2,2,n_freq);

%with a quasi-monostatic angle of 5 degrees, the cross-polar terms are:
theta = 5*pi/180;
S_meshtilt(1,2,:) = -1/2*S_meshvert(2,2,:)/cos(theta/2); %differs by
factor of -1 from bis_simpol.pro
S_meshtilt(2,1,:) = S_meshtilt(1,2,:);

%solve for the remaining diagonal terms of C
C(2,2,:) = M_meshtilt(1,2,:)./S_meshtilt(1,2,:);
C(3,3,:) = M_meshtilt(2,1,:)./S_meshtilt(2,1,:);

%assuming the second-order crosspolar terms are negligible
%(the simple-polarimetric assumption), we can leave the elements
%C(1,2), C(1,3), C(1,4), C(4,1), C(4,2), and C(4,3) as zero.
%C(2,2,:) = Mmesh(2,1,:)./Smesh(2,1,:);
%C(3,3,:) = Mmesh(1,2,:)./Smesh(1,2,:);

%similarly, leave the crosspolar terms C(2,1), C(2,3), C(2,4),
%C(3,1), C(3,2), and C(3,4) as zero.

%Christopher J Bradley
%2d Lt, USAF
%AFIT/ENG
%cbradley@ieee.org
%29 September 2000

```

```

%CAL_D_MOD Compute 4x4 calibration matrix (C) from the subtracted
%calibration object files
%This function is a modification of the EMSL simple polarimetric
%calibration procedure.
%C = cal_d(N_disk,P_disk,N_dihedral,P_dihedral)
%INPUTS:
%disk--2x2xn_freq scattering matrix of disk
%dihedral--2x2xn_freq scattering matrix of dihedral tilted 22.5 deg
%OUTPUT:
%C--4x4xn_freq calibration coefficient matrix

function C = cal_d_mod(N_disk,P_disk,N_dihedral,P_dihedral)

global freq_start
global freq_stop
global n_freq
global n_ang
global C

if n_ang>1
    warning('Calibration files contain more than one angle--this routine
will utilize only the first')
    N_disk = squeeze(N_disk(:,:,1));
    N_dihedral = squeeze(N_dihedral(:,:,1));
else
    N_disk = squeeze(N_disk);
    N_dihedral = squeeze(N_dihedral);
end

C = zeros(4,4,n_freq); %initialization of 4x4 diagonal distortion
matrix

%get PO prediction for calibration disk
S_disk = P_disk;

%calculate the co-polar calibration terms
C(1,1,:) = N_disk(1,1,:)./S_disk(1,1,:);
C(4,4,:) = N_disk(2,2,:)./S_disk(2,2,:);

%calculate the absolute magnitude of the tilted dihedral
S_dihedral = zeros(2,2,n_freq);

%with a quasi-monostatic angle of 5 degrees, the cross-polar terms are:
S_dihedral(1,2,:) = P_dihedral(:,6); %vh pol
S_dihedral(2,1,:) = P_dihedral(:,5); %hv pol

%solve for the remaining diagonal terms of C:
C(2,2,:) = N_dihedral(1,2,:)./S_dihedral(1,2,:);
C(3,3,:) = N_dihedral(2,1,:)./S_dihedral(2,1,:);

%Christopher J Bradley
%2d Lt, USAF
%AFIT/ENG
%cbradley@ieee.org
%7 February 2001

```

```

%CAL_D Compute 4x4 calibration matrix (C) from the subtracted
calibration object
%files (Type-1 calibration version)
%C = cal_d(disk,disk_diam_cm)
%INPUTS:
%disk--2x2xn_freq scattering matrix of disk
%disk_diam_cm--diameter of disk in cm
%f_start_GHz--start frequency in GHz
%f_stop_GHz--stop frequency in GHz
%OUTPUT:
%C--4x4xnfreq calibration coefficient matrix

function C = cal_e(M_disk,disk_diam_cm)

global freq_start
global freq_stop
global n_freq
global n_ang
global C

if n_ang>1
    warning('Calibration files contain more than one angle--this routine
will utilize only the first')
    M_disk = squeeze(M_disk(:,:,:,1));
else
    M_disk = squeeze(M_disk);
end

C = zeros(4,4,n_freq); %initialization of 4x4 diagonal distortion
matrix

%get PO prediction for calibration disk
S_disk = calcdisk(disk_diam_cm,freq_start,freq_stop,n_freq);

%calculate the co-polar calibration terms
C(1,1,:) = M_disk(1,1,:)./S_disk(1,1,:);
C(4,4,:) = M_disk(2,2,:)./S_disk(2,2,:);

%Christopher J Bradley
%2d Lt, USAF
%AFIT/ENG
%cbradley@ieee.org
%7 December 2000

```

```

%CAL_EXEC_C
%Perform the matrix multiplication to calibrate a measurement
%using the C-matrix (4x4 system distortion matrix), given
%the distortion matrix and raw measurement.
%S = cal_exec_c(M)
%INPUT:
%M -- uncalibrated data, with subtraction and gating already performed
%OUTPUT:
%S -- calibrated data

function S = cal_exec_c(M)
global n_freq
global n_ang
global C
S = zeros(size(M));

%invert C-matrix
for m=1:n_freq
    C_inv(:, :, m) = inv(squeeze(C(:, :, m)));
end

q=waitbar(0, 'Calibrating...');
for m=1:n_freq
    for n=1:n_ang
        M_vec = squeeze([M(1,1,m,n);M(1,2,m,n);M(2,1,m,n);M(2,2,m,n)]);
        S_vec(:,m,n) = C_inv(:, :, m)*M_vec;
    end
    waitbar(m/n_freq);
end
close(q)
disp('Converting to scattering matrix format...')
S = convert_scatter(S_vec);

%Christopher J Bradley
%2d Lt, USAF
%AFIT/ENG
%cbradley@ieee.org
%29 September 2000

```

```

%2d Lt Christopher J Bradley
%AFIT/ENG
%Calibration Method A: Whitt, Ulabay, Polatin, & Liepa, "A General
Polarimetric
%Radar Calibration Technique," IEEE Transactions on Antennas and
Propagation,
%vol. 39, no. 1, Jan 1991.
%This is a general fully-polarimetric monostatic/bistatic calibration
technique
%that makes no assumptions regarding the form of the scattering
matrices of the
%reference object (excepting that one of the matrices is invertible) or
of the
%form of the system distortion matrices (R and T). It requires 3
objects with
%precisely known scattering matrices.

function [phi,c,R,T]=cala(P1,P2,P3,N1,N2,N3)

%Objects (3):      metallic sphere
%                  long metallic cylinder (45 deg., horizontal, or
vertical)
%                  squat metallic cylinder (45 deg., horizontal, or
vertical)

%Inputs: (column vectors)
%N1:      Measured scattering matrix of calibration object 1
(invertible)
%P1:      Theoretical scattering matrix of calibration object 1
(invertible)
%N2:      Measured scattering matrix of calibration object 2
%P2:      Theoretical scattering matrix of calibration object 2
%N3:      Measured scattering matrix of calibration object 3
%P3:      Theoretical scattering matrix of calibration object 3
%nrfreq: number of frequency points

%Outputs:
%phi:      Absolute phase correction
%c:      Magnitude correction
%R:      Receiver distortion matrix
%T:      Transmitter distortion matrix

%construct the matrices necessary to perform the calibration:
Nt=inv(N1)*N2;
NtB=inv(N1)*N3;
Pt=inv(P1)*P2;
PtB=inv(P1)*P3;
[Xt,LtP]=eig(Pt);
[Yt,Lt]=eig(Nt);
[XtB,LtPB]=eig(PtB);
[YtB,LtB]=eig(NtB);

Nr = N2*inv(N1);
NrB = N3*inv(N1);
Pr = P2*inv(P1);
PrB = P3*inv(P1);
[Xr,LrP] = eig(Nr);

```

```

[Yr,Lr] = eig(Pr);
[XrB,LrPB] = eig(NrB);
[YrB,LrB] = eig(PrB);

%equations for relative phase of the reference objects (not used here):
diff_philphi2 = angle(LtP)-angle(Lt);
diff_philphi3 = angle(LtPB)-angle(LtB);
diff_phi2phi1 = angle(LrP)-angle(Lr);
diff_phi3phi1 = angle(LrPB)-angle(LrB);

%identify each element of Xt and Yt and assign them to scalar
variables:
x11=Xt(1,1);x12=Xt(1,2);x21=Xt(2,1);x22=Xt(2,2);
x11B=XtB(1,1);x12B=XtB(1,2);x21B=XtB(2,1);x22B=XtB(2,2);
y11=Yt(1,1);y12=Yt(1,2);y21=Yt(2,1);y22=Yt(2,2);
y11B=YtB(1,1);y12B=YtB(1,2);y21B=YtB(2,1);y22B=YtB(2,2);

%formulae for ratios of the elements of the matrix of constants, "C":
rat_c2c1(1) = (x11*x21B-x21*x11B)*(y22*y11B-y12*y21B)/ ...
    (x22*x11B-x12*x21B)/(y11*y21B-y21*y11B);
rat_c2c1(2) = (x11*x22B-x21*x12B)*(y22*y12B-y12*y22B)/ ...
    (x22*x12B-x12*x22B)/(y11*y22B-y21*y12B);
rat_c2Bc1B(1) = (x22*x11B-x12*x21B)*(y22*y12B-y12*y22B)/ ...
    (x22*x12B-x12*x22B)/(y22*y11B-y12*y21B);
rat_c2Bc1B(2) = (x11*x21B-x21*x11B)*(y11*y22B-y21*y12B)/ ...
    (x11*x22B-x21*x12B)/(y11*y21B-y21*y11B);

%one of these ratios may be zero--if so, use the other one:
if rat_c2c1(1)==0
    use_c_rat = rat_c2c1(2);
else
    use_c_rat = rat_c2c1(1);
end
if rat_c2Bc1B(1)==0
    use_CB_rat = rat_c2Bc1B(2);
else
    use_CB_rat = rat_c2Bc1B(1);
end
if ~isfinite(use_c_rat) | ~isfinite(use_CB_rat)
    warning('"c" ratios are infinite--system is indeterminate')
end

if rat_c2c1==0 | rat_c2Bc1B==0
    warning('"c" ratios are zero--system is indeterminate')
end

%if Pt and PtB have more than one eigenvalue in common,
%the system is indeterminate:
if [Xt(1,1) Xt(1,2)] == ( [XtB(1,1) XtB(1,2)] | [XtB(2,1) XtB(2,2)]
)...
    &...
    [Xt(1,1) Xt(1,2)] == ( [XtB(1,1) XtB(1,2)] | [XtB(2,1) XtB(2,2)] )
    warning('Pt and PtB have common eigenvalues--system is
indeterminate')
end

c1 = det(Yt)/(x11*y22-use_c_rat*x12*y21);

```

```

c2 = det(Yt)/(x11*y22/use_c_rat-x12*y21);

%diagonal matrix of constants to solve for Tx distortion matrix:
C = [c1 0; 0 c2];
check = (c1*x11*y22-c2*x12*y21)/det(Yt);
if round(100*check)/100 ~= 1
    warning('first element of matrix T should be "1", but it isnt')
end

%transmitter distortion matrix:
T = Xt*C*inv(Yt);

%The development to solve for the receiver distortion matrix, "R", is
%almost identical to that of the transmitter distortion matrix, "T",
%except the assignment of Nr, Pr, NrB, and PrB (above) is slightly
%different.

%identify each element of Xr and Yr and assign them to scalar
variables:
x11=Xr(1,1);x12=Xr(1,2);x21=Xr(2,1);x22=Xr(2,2);
x11B=XrB(1,1);x12B=XrB(1,2);x21B=XrB(2,1);x22B=XrB(2,2);
y11=Yr(1,1);y12=Yr(1,2);y21=Yr(2,1);y22=Yr(2,2);
y11B=YrB(1,1);y12B=YrB(1,2);y21B=YrB(2,1);y22B=YrB(2,2);

%formulae for ratios of the elements of the matrix of constants, "D":
rat_d2d1(1) = (x11*x21B-x21*x11B)*(y22*y11B-y12*y21B)/ ...
    (x22*x11B-x12*x21B)/(y11*y21B-y21*y11B);
rat_d2d1(2) = (x11*x22B-x21*x12B)*(y22*y12B-y12*y22B)/ ...
    (x22*x12B-x12*x22B)/(y11*y22B-y21*y12B);
rat_d2Bd1B(1) = (x22*x11B-x12*x21B)*(y22*y12B-y12*y22B)/ ...
    (x22*x12B-x12*x22B)/(y22*y11B-y12*y21B);
rat_d2Bd1B(2) = (x11*x21B-x21*x11B)*(y11*y22B-y21*y12B)/ ...
    (x11*x22B-x21*x12B)/(y11*y21B-y21*y11B);

%one of these ratios may be zero--if so, use the other one:
if ~isfinite(rat_d2d1(1)) | rat_d2d1(1)==0
    use_d_rat = rat_d2d1(2);
else
    use_d_rat = rat_d2d1(1);
end
if ~isfinite(rat_d2Bd1B(1)) | rat_d2Bd1B(1)==0
    use_dB_rat = rat_d2Bd1B(2);
else
    use_dB_rat = rat_d2Bd1B(1);
end

if ~isfinite(use_d_rat) | ~isfinite(use_dB_rat)
    warning('"d" ratios are infinite--system is indeterminate')
end
if use_d_rat==0 | use_dB_rat==0
    warning('"d" ratios are zero--system is indeterminate')
end

d1 = det(Yr)/(x11*y22-use_d_rat*x12*y21);
d2 = det(Yr)/(x11*y22/use_d_rat-x12*y21);

%diagonal matrix of constants to solve for Rx distortion matrix:

```

```

D = [d1 0; 0 d2];
check = (d1*x11*y22-d2*x12*y21)/det(Yr);
if round(100*check)/100 ~= 1
    warning('first element of matrix R should be "1", but it is not')
end

%receiver distortion matrix:
R = Xr*D*inv(Yr);

%optimize precision for the constant c:
%best_P = input('Which theoretical matrix to use for "c" (most precise)
? ');

%back-substitute to find magnitude/phase correction factor:

%Note: It is best to use a diagonal element (1 or 4) to find 'c'
%because the diagonal elements are much more stable with noise
%than the off-diagonal elements
%eval(['c_complex = N(1)' num2str(best_P) './(R(1)*P(1)'\...
%      num2str(best_P) '*T(1));'])
c_complex = N1(4)./(R(4)*P1(4)*T(4));
%magnitude correction factor:
c = abs(c_complex);

%phase correction factor (relative):
phi = angle(c_complex);

%Christopher J Bradley
%2d Lt, USAF
%AFIT/ENG
%cbradley@ieee.org
%29 September 2000

```



```

%CALE Implementation of Type-1 calibration technique
%2d Lt Christopher J Bradley
%AFIT/ENG
%Calibration Method E: Jersak, "Bistatic, Fully Polarimetric Radar
Cross-Section
%Calibration Techniques and Measurement Error Analysis," Ph.D.
dissertation,
%University of Texas at Arlington, Dec. 1993, pp. 94-96.

%This is a very basic polarimetric calibration technique requiring only
a single
%reference object (sphere). It does not account for cross-pol leakage
of the
%antennas, and at bistatic angles at which there is a null in the
return from
%the sphere, the technique cannot be performed. It has the advantage
that it
%is completely insensitive of object orientation.

%INPUTS:
%M0: measurement of sphere (matrix)
%S0: predicted value of sphere (matrix)

%OUTPUTS:
%Ch: modified distortion matrix: pointwise (hadamard) product with
% unknown object scattering matrix reveals the calibrated value

%Objects (1): metallic sphere

function Ch = cale(M0,S0)
global n_freq

Ch = zeros(2,2); %initialization of 4-element distortion matrix

%fill distortion matrix:
Ch(1,1) = S0(1,1)/M0(1,1);
Ch(2,2) = S0(2,2)/M0(2,2);
Ch(1,2) = S0(1,2)/M0(1,2);
Ch(2,1) = S0(2,1)/M0(2,1);

%Christopher J Bradley
%2d Lt, USAF
%AFIT/ENG
%cbradley@ieee.org
%29 September 2000

```

```
%GET_C Compute system distortion matrix C using the EMSL simple
%polarimetric calibration technique. No inputs are given, and the
%output (C) is returned to a global variable. Utilizes "cal_d.m"
%to compute the C matrix.
```

```
function get_C
global C
global n_freq
global freq_start
global freq_stop
f = linspace(freq_start,freq_stop,n_freq);

disp('Input raw calibration files--')
C1_s = input('calibration disk file: ','s');
C2_s = input('empty room file: ','s');
C3_s = input('vertical mesh: ','s');
C4_s = input('tilted mesh: ','s');
diam = input('calibration disk diameter (cm): ');
C1 = read_emsl(C1_s);
C2 = read_emsl(C2_s);
C3 = read_emsl(C3_s);
C4 = read_emsl(C4_s);
C1 = C1-C2;
C3 = C3-C2;
C4 = C4-C2;
g1 = input('Gate start time (ns): ');
g2 = input('Gate stop time (ns): ');
t = linspace(g1,g2,n_freq);
C1_ga = time_gate(C1,f,t);
C3_ga = time_gate(C3,f,t);
C4_ga = time_gate(C4,f,t);
C = cal_d(C1_ga,diam,C3_ga,C4_ga);

s = input('Save coefficient matrix C as a mat file? ','s');
if s(1)=='y'
    dir = input('directory: ','s');
    name = input('File name: ','s');
    eval([name, '=C;'])
    eval(['save ',dir,'\ ',name,' ',name])
    size(C)
else
end

%Christopher J Bradley
%2d Lt, USAF
%AFIT/ENG
%cbradley@ieee.org
%29 September 2000
```

```

%CALCDISK
%generate theoretical scattering matrix for a metallic circular disk
%(Physical Optics approximation), in amplitude, NOT dBsm
%Inputs:
%diam = diameter in centimeters
%freq_start = start frequency (GHz)
%freq_stop = stop frequency (GHz)
%nfreq = number of frequency samples

function S = calcdisk(diam,freq_start,freq_stop,nfreq)

%convert diameter (m) to radius (cm)
r = diam/2/100;

%initialize structure
S = zeros(2,2,nfreq);

%propagation velocity
c0 = 2.998E8;

%wavelength
lambda = c0./linspace(freq_start*1E9,freq_stop*1E9,nfreq);

%cross-sectional area
A = pi*(r)^2;

%co-polar components are equal, cross-polar are zero
S(1,1,:) = 2*i*sqrt(pi)*A./lambda;
S(2,2,:) = S(1,1,:);

```

```

%CALIBRATE_DATA Calibrate gated and subtracted data
%The routine is interactive within the Matlab workspace, and prompts
%for the raw data files, which must be in the unprocessed EMSL HP
format
%S = calibrate_data(M)
%INPUT:
%M -- input scattering matrix: 2 x 2 x n_freq x n_ang
%OUTPUT:
%S -- calibrated scattering matrix of the same dimensions

```

```

function S = calibrate_data(M)

global freq_start
global freq_stop
global n_freq
global n_ang
global ang
global C
file = input('Enter file name of data: ','s');
read_hdr(file);
f = linspace(freq_start,freq_stop,n_freq);

%calibrate:
docal = input('Perform new calibration? ','s');
if docal(1)=='y'
    which_cal = input('Calibrate with sphere? ','s');
    if which_cal(1) == 'n'
        get_C;
    else
        get_C_sph;
    end
elseif docal(1)=='n'
    disp('If not in memory, enter dir and filename--');
    dir = input('directory: ','s');
    name = input('file name: ','s');
    if isempty(name)
        %do nothing--C is a global variable.
    else
        eval(['load ',dir,'\',name])
        eval(['C=',name,',';'])
    end
end
read_hdr(file);
S = cal_exec_C(M);
read_hdr(file);
in_2 = input('Plot calibrated data? ','s');
if in_2(1) == 'y'
    pol = input('View polarization: ','s')
    sel_f = input('View frequency (GHz): ');
    [sel_f,sel_f_ind] = min(abs(f-sel_f));
    if n_ang>1
        sel_a = input('View angle (deg): ');
        [sel_a,sel_a_ind] = min(abs(ang-sel_a));
        view_data_a = get_angle_sweep(S,pol,sel_f_ind);
        view_data_f = get_freq_sweep(S,pol,sel_a_ind);
        figure(1)
        subplot(2,1,1)
    end
end

```

```

        plot(ang,view_data_a)
        title(['RCS vs. angle, ', num2str(f(sel_f_ind)), ' GHz'])
        subplot(2,1,2)
        plot(f,view_data_f)
        title(['RCS vs. frequency, ', num2str(sel_a), ' deg'])
    elseif n_ang==1
        view_data = get_freq_sweep(S,pol,1);
        figure(1)
        plot(f,view_data)
        title('RCS vs. frequency')
    end
end
s = input('Save data as a .mat file? ','s');
if s(1)=='y'
    dir = input('Directory: ','s');
    name = input('File name: ','s');
    eval([name, '=S;'])
    eval(['save ',dir,'\ ',name,' ',name])
else
end

%Christopher J Bradley
%2d Lt, USAF
%AFIT/ENG
%cbradley@ieee.org
%29 September 2000

```

```

%CONVERT_FISC Convert .mat files generated from "fiscread.m"
%or "read_field_2.m" into another .mat file corresponding to the
structure
%of the measurement scattering matrices
scat_data = convert_fisc(a,f,n_ang)
function scat_data = convert_fisc(a,f,n_ang)

%initialize vectors:
f_data = round(a(:,1)*10000)/10000;
f = round(f*10000)/10000;
n_freq = length(f);
scat_data = zeros([2,2,n_freq,n_ang]);

%sort by frequencies:
global m
%fill scattering matrix:
h=waitbar(0,'filling matrix');
for m = 1:n_freq
    f_ind = find(f_data==f(m));
    scat_data(2,2,m,:)=a(f_ind,4);    %vv pol
    scat_data(1,1,m,:)=a(f_ind,7);    %hh pol
    scat_data(1,2,m,:)=a(f_ind,6);    %vh pol
    scat_data(2,1,m,:)=a(f_ind,5);    %hv pol
    waitbar(m/n_freq)
end
close(h)

```

```

%CONVERT_SCAT
%scat_new = convert_scat(scat,n_freq)
%convert structures between scattering matrix and scattering
%vector format (toggle):
%Scattering matrix = [ HH  VH ]
%                   [ HV  VV ]
%Scattering vector = [ HH ]
%                   [ VH ]
%                   [ HV ]
%                   [ VV ]
%INPUTS:
%scat:      input structure variable
%OUTPUT:
%S:    converted scattering structure

function S = convert_scat(scat)
global n_freq
global n_ang
%if the number of dimensions of the input structure is 4,
%then we must convert to the 3-dimensional (scattering matrix)
%format:
if n_ang>1
if ndims(scat)==4
S=zeros(4,n_freq,n_ang);
for m=1:n_freq
for n=1:n_ang

S(:,m,n)=squeeze([scat(1,1,m,n);scat(1,2,m,n);scat(2,1,m,n);scat(2,2
,m,n)]);
end
end
%conversely, if the number of dimensions of the input
%structure is 3, then we convert to the 4-dimensional
%(scattering vector) format:
elseif ndims(scat)==3
n_ang=length(scat(1,1,:));
S=zeros(2,2,n_freq,n_ang);
for m=1:n_freq
for n=1:n_ang
S(1,1,m,n)=scat(1,m,n);
S(1,2,m,n)=scat(2,m,n);
S(2,1,m,n)=scat(3,m,n);
S(2,2,m,n)=scat(4,m,n);
end
end
else
error('input structure "scat" has the wrong dimensions')
end
end
if n_ang==1
if ndims(scat)==3
S=zeros(4,n_freq);
for m=1:n_freq
S(:,m)=squeeze([scat(1,1,m);scat(1,2,m);scat(2,1,m);scat(2,2,m)]);
end
elseif ndims(scat)==2

```

```

S=zeros(2,2,n_freq);
for m=1:n_freq
    S(1,1,m)=scat(1,m);
    S(1,2,m)=scat(2,m);
    S(2,1,m)=scat(3,m);
    S(2,2,m)=scat(4,m);
end
else
    error('input structure "scat" has the wrong dimensions')
end
end

```

```

%Christopher J Bradley
%2d Lt, USAF
%AFIT/ENG
%cb Bradley@ieee.org
%29 September 2000

```



```

%GATE_DATA Read, view and/or gate unprocessed data
%The routine is interactive from the Matlab workspace. The input
%data files should be in the raw format from the EMSL HP, and are
output
%into scattering matrix format.
%S = gate_data
%OUTPUT:
%S_final -- processed data, as defined by user prompts

function S_final = gate_data
close all

tar_file = input('Directory and name of object file: ','s');
ER_file = input('Directory and name of empty room file: ','s');
disp('Loading data files...')
ER = read_emsl(ER_file);
tar = read_emsl(tar_file);
global object
global mnemonic
global freq_start
global freq_stop
global f
global n_freq
global n_ang
global ang

tar_name = [mnemonic, ', ', 'object'];

S = tar - ER;
df = f(2)-f(1);

p = input('Plot frequency domain? (y or n): ','s');
if p(1) == 'y'
    pol = input('Polarization? ','s');
    if n_ang>1
        scat_plot_2D(S,pol,f, 'freq')
        label('freq',0,pol)
    else
        plot(f,get_freq_sweep(S,pol))
        label('freq',0,pol)
    end
elseif p(1) == 'n'
end

g = input('Apply range gate (y or n)? ','s');
if g(1)=='y'
    pol = input('View polarization: ','s');
    if length(pol)==2
        w1 = input('Time window--start (ns): ');
        w2 = input('Time window--stop (ns) : ');
        t_range = linspace(w1,w2,n_freq);
        if w1>w2
            error('improper windowing parameters: w1>w2')
        elseif w2>round((1/df))
            warning('window is beyond unambiguous range')
        end
        if n_ang==1

```

```

        time_view = tfconvert(S,f,t_range, 'time');
        time_view = get_freq_sweep(time_view,pol,1);
        figure(1)
        plot(t_range,time_view)
        label('time',0,pol)
    elseif n_ang>=1
        time_view = tfconvert(S,f,t_range, 'time');
        figure(1)
        scat_plot_2D(time_view,pol,t_range, 'time');
        label('time',0,pol)
    end
end
g1 = input('Select gate cutoff--start: ');
g2 = input('Stop : ');
if g1>g2
    error('improper windowing parameters: w1>w2')
elseif g2>(1/df)
    warning('gate is beyond unambiguous range')
end
S_final = time_gate(S,f,linspace(g1,g2,n_freq));
v = input('View data? ','s');
if v(1)=='y'
    if n_ang>1
        sel_a = input('angle (deg): ');
        sel_f = input('frequency (GHz): ');
        pol = input('View polarization: ','s');
        [q,sel_f_ind] = min(abs(f-sel_f));
        [q,sel_a_ind] = min(abs(ang-sel_a));
        view_ga_a = get_angle_sweep(S_final,pol,sel_f_ind);
        view_ga_f = get_freq_sweep(S_final,pol,sel_a_ind);
        figure(1)
        subplot(2,1,1)
        plot(ang,view_ga_a)
        label('angle',f(sel_f_ind),pol)
        subplot(2,1,2)
        plot(f,view_ga_f)
        label('freq',ang(sel_a_ind),pol)
    elseif n_ang==1
        pol = input('View polarization: ','s');
        view_ga = get_freq_sweep(S_final,pol,1);
        figure(1)
        plot(f,view_ga)
        label('freq',0,pol)
    end
else
    end
elseif g(1)=='n'
    S_final = S;
end
s = input('Save data as a .mat file? ','s');
if s(1)=='y'
    dir = input('Directory: ','s');
    name = input('File name: ','s');
    eval([name, '=S_final;'])
    eval(['save ',dir,'\',name,' ',name])
else
    end
end

```

%Christopher J Bradley
%2d Lt, USAF
%AFIT/ENG
%cbradley@ieee.org
%29 September 2000

```

%GET_ANGLE_SWEEP Read the scattering matrix 'S' (in complex power
%format), select a single frequency, and convert to dBsm.
%S_dB = get_angle_sweep(S,pol,freq_index)
%INPUTS:
%S -- input scattering matrix (complex power)
%pol -- desired polarization
%freq_index -- desired frequency index
%OUTPUT:
%S_dB -- vector of RCS (dBsm) for a single polarization, single
frequency
function S_dB = get_angle_sweep(S,pol,freq_index)

if pol=='hh'
    r = 1;
    c = 1;
elseif pol=='vh'
    r = 1;
    c = 2;
elseif pol=='hv'
    r = 2;
    c = 1;
elseif pol=='vv'
    r = 2;
    c = 2;
else
    error('Unrecognized variable "pol" ')
end

S_dB = 20*log10(abs(squeeze(S(r,c,freq_index,:))));

%Christopher J Bradley
%2d Lt, USAF
%AFIT/ENG
%cbradley@ieee.org
%29 September 2000

```

```

%GET_ANGLE_SWEEP Read the scattering matrix 'S' (in complex power
%format), select a single angular position, and convert to dBsm.
%S_dB = get_freq_sweep(S,pol,ang_index)
%INPUTS:
%S -- input scattering matrix (complex power)
%pol -- desired polarization
%ang_index -- desired angular position index
function S_dB = get_freq_sweep(S,pol,ang_index)

if pol=='hh'
    r = 1;
    c = 1;
elseif pol=='vh'
    r = 1;
    c = 2;
elseif pol=='hv'
    r = 2;
    c = 1;
elseif pol=='vv'
    r = 2;
    c = 2;
else
    error('Unrecognized variable "pol" ')
end

if length(size(S))<=3
    S_dB = 20*log10(abs(squeeze(S(r,c,:))));
else
    S_dB = 20*log10(abs(squeeze(S(r,c,:,ang_index))));
end

%Christopher J Bradley
%2d Lt, USAF
%AFIT/ENG
%cbradley@ieee.org
%29 September 2000

```

```

%IDLCONVERT
%input and convert a '.fre' (w/o frequency and time values)
%file from IDL and read into MATLAB also convert the values
%into complex scattering matrix format:
%      [ HH   VH ]
%scat_mat = [      ]
%      [ HV   VV ]
% The scattering matrix is (in general) 4-dimensional--
%scat_mat(k,l,m,n):
% k,l: polarization dimensions (traditional 2x2 scattering matrix)
% m:   frequency dimension
% n:   angle dimension
%This function is different from "read_ems1.m" in that it uses '.fre'
%or '.tim' files which do not contain a header.
%INPUTS:
%file_name:      string containing the directory and file name
%numfreq:        number of frequencies per sweep

%The output tensor 's' is in complex power (absolute, not dB)
%form. To convert to dB --> 20*log10(abs(scat_mat))

function s = idlconvert(file_name,numfreq)

%data files always contain 4 polarizations:
numpol = 4;

    fid = fopen(file_name, 'r','b');
    [a, count] = fread(fid, 'float');
    numangle = count/2/numfreq/numpol;
    stmp = zeros(2,2,2,numfreq,numangle);
    stmp(:) = a;
    s = stmp(1,:,:,:,:) + j*stmp(2,:,:,:,:);
    s = squeeze(s);

    %Christopher J Bradley
    %2d Lt, USAF
    %AFIT/ENG
    %cbradley@ieee.org
    %29 September 2000

```

```

%MCHIRPZ Chirp-z transform
%g = mchirpz(x,f,t,sgn)
%INPUTS:
%x:    input vector
%f:    vector of frequency values (or initial domain)
%t:    vector of time values (or transform domain)
%sgn:  1 to convert to time, -1 to convert to frequency
%Joaquim Fortuny, 27 Aug 2000

function g=mchirpz(x,f,t,sgn)

x=x(:).';
f=f(:);
t=t(:);
n=length(x);
m=length(t);
tpi=2*pi;
dw=tpi*(f(2)-f(1));
dt=t(2)-t(1);
w0=tpi*f(1);
t0=t(1);
l=n+m-1;
l=pow2(floor(log2(l))+1);

xa=zeros(1,l);
xb=xa;
xc=xa;
xa(1:n)=x.*exp(j*sgn*(dw*t0*(0:n-1)+dw*dt*(0:n-1).^2/2));
xa=fft(xa);

xb(1:m)=exp(-j*sgn*dw*dt*(0:m-1).^2/2);
xb(1-n+2:l)=exp(-j*sgn*dt*dw*(l-(l-n+1:l-1)).^2/2);
xb=fft(xb);
xc=ifft(xa.*xb);
if sgn==1
    factor=1/length(f);
else
    factor=1;
end
g=xc(1:m).*exp(j*sgn*((t0+(0:m-1)*dt)*w0+dw*dt*(0:m-1).^2/2));
g=g*factor;

```

```

%READ_EMSL Read the raw, unprocessed data from the EMSL HP into a
%scattering matrix understandable to MATLAB. Uses global variables
%initialized in "read_hdr.m"
%S = read_emsl(file)

%INPUT:
%file -- directory and file name of the EMSL unprocessed data
%OUTPUT:
%S -- data in 2 x 2 x n_freq x n_ang scattering matrix format

function S = read_emsl(file)
global n_freq
global n_ang
global n_hdr

%read the header of the data file and give values to the
%global variables above:
read_hdr(file);

%useful constants:
bytes = 9;      %number of bytes per line of data
bad_lines = 3;  %number of lines of bad data per position

%read IDL data:
fclose('all');
fid = fopen(file, 'r', 's');
f=fread(fid, 'double');
%select binary data:
%The data begins 3 lines after the end of the header
hdr_length = bytes*(n_hdr);
f_data_1 = f(hdr_length+1:end);

%The raw data has 3 lines of garbage at the beginning
%of each frequency sweep which have to be removed:
n = [];
for m=1:(bytes*n_freq+bad_lines*bytes):length(f_data_1);
    n = [n m:m+bad_lines*bytes-1];
end
f_data_1(n) = [];

%find and remove frequency indices:
freq = [];
f_data = f_data_1;
f_data(1:bytes:length(f_data)) = [];

%(2 channels (real, imaginary), 4 polarizations, n_freq frequencies)
%convert the vector into scattering matrix format:
stmp = zeros(2,2,2,n_freq,n_ang);
stmp(:) = f_data;
S = squeeze(stmp(1,:,:,:,:)+j*stmp(2,:,:,:,:));

%Christopher J Bradley
%2d Lt, USAF
%AFIT/ENG
%cbradley@ieee.org
%29 September 2000

```



```

%READ_FIELD_2
%field_mat = read_field_2(filename)
%This function takes the .field file generated by FISC
%and converts it to a MATLAB matrix that is output to
%the workspace. The output matrix is of the same form
%as the original file, i.e. 7 columns:
%frequency : obs-EL : obs-AZ : VV : HV : VH : HH

%2d Lt Christopher J Bradley
%AFIT/ENG
%29 Nov 2000

function field_mat = read_field_2(filename)
%element 1: incident elevation
%element 2: incident azimuth
%element 3: observation elevation
%element 4: observation azimuth
%element 5: frequency (GHz)
%element 6: vv-real
%element 7: vv-imaginary
%element 8: hv-real
%element 9: hv-imaginary
%element 10: vh-real
%element 11: vh-imaginary
%element 12: hh-real
%element 13: hh-imaginary

inc_el = [];
inc_az = [];
obs_el = [];
obs_az = [];
f = [];
vv_r = []; vv_i = [];
hv_r = []; hv_i = [];
vh_r = []; vh_i = [];
hh_r = []; hh_i = [];
vv = [];
hv = [];
vh = [];
hh = [];

tic
data = textread(filename, '%s',...
    'whitespace',' ','headerlines',5);
toc
%data = textread('short_cyl_10t11.field','%s','whitespace','
    ','headerlines',5);
tic
N = length(data);
q_char = [];
x_data = [];
for n=1:N
    x = data(n);
    q_char = cat(1,x{:});
    if length(q_char)>1
        k_open = findstr(q_char, '(');
        k_clos = findstr(q_char, ')');

```

```

        k_comm = findstr(q_char, ',');
        if ~isempty(k_open)
            x_data(n) = str2num(q_char(k_open+1:k_comm-1)) ...
                +j*str2num(q_char(k_comm+1:k_clos-1));
        else x_data(n) = str2num(q_char);
        end
    elseif length(q_char)==1
        x_data(n) = NaN;
    end
end
N_data = length(x_data);
n=1;
while n<length(x_data)
    if isnan(x_data(n))
        x_data(n) = [];
    end
    n=n+1;
end
N_data = length(x_data)

for n = 1:9:N_data
    inc_el = [inc_el x_data(n)];
    inc_az = [inc_az x_data(n+1)];
    obs_el = [obs_el x_data(n+2)];
    obs_az = [obs_az x_data(n+3)];
    f = [f x_data(n+4)];
    vv = [vv x_data(n+5)];
    hv = [hv x_data(n+6)];
    vh = [vh x_data(n+7)];
    hh = [hh x_data(n+8)];
end

field_mat = zeros(N_data/9,7);
field_mat(:,1) = f';
field_mat(:,2) = obs_el';
field_mat(:,3) = obs_az';
field_mat(:,4) = vv';
field_mat(:,5) = hv';
field_mat(:,6) = vh';
field_mat(:,7) = hh';

%save as .mat file
eval([filename(1:end-7),'_field = field_mat;'])
eval(['save i:\igars2000\fisc\fiscmat\'',...
    %     filename(1:end-7),'_field ', filename(1:end-7),'_field'])
eval(['save i:\igars2000\fisc\fiscmat\'',filename(1:end-7),...
    %     '_field ',filename(1:end-7),'_field'])

```

```

%READ_HDR read and interpret information from EMSL file header
%and store the pertinent information in global variables. The routine
%is presently only capable of handling up to two tasks in the EMSL data
file.
%read_hdr(file)
%INPUT:
%file -- directory path and name of unprocessed data file from the
%EMSL HP.
%The function returns the pertinent variables as global
%variables, namely:
%object:      object name as identified in header
%mnemonic:    object mnemonic name as identified in header
%freq_start:  start frequency, in GHz
%freq_stop:   stop frequency, in GHz
%n_freq:      number of frequency samples
%f:           vector of frequencies
%avg:         number of averaging points
%tx_sled:     sled used for transmitter
%rx_sled:     sled used for receiver
%movement:    axis that is moving
%A_position:  initial position of Sled A
%B_position:  initial position of Sled B
%D_position:  initial position of rotation axis
%L_position:  initial position of linear translation axis
%n_ang:       number of angular samples
%ang:         vector of angular movements/separation of relevant axis
%n_hdr:       number of lines contained in the header
%hdr:         complete text of header

```

```

function read_hdr(file)

```

```

global object
global mnemonic
global freq_start
global freq_stop
global n_freq
global f
global avg
global tx_sled
global rx_sled
global movement
global A_position
global B_position
global D_position
global L_position
global n_ang
global ang
global n_hdr
global hdr

```

```

%read header again to get information about the EMSL data file:

```

```

fclose('all');
fid=fopen(file, 'rt');
hdr=fscanf(fid, '%c', 200*72);
hdr_size=size(hdr);

```

```

%get size of header (line 4):
n_head_1 = 72*3+18;

```

```

n_head_2 = 4*72;
n_hdr = str2num(hdr(n_head_1:n_head_2));

%get object and mnemonic(lines 1 and 11):
mnemonic = hdr(7:72);
object = hdr(72*10+10:72*11);

%get initial axis positions (lines 28-31):
A_position = str2num(hdr(27*72+1:28*72));
B_position = str2num(hdr(28*72+1:29*72));
D_position = str2num(hdr(29*72+1:30*72));
L_position = str2num(hdr(30*72+1:31*72));

%get LB/UHF parameters:
s_f = 'Microwave LB/UHF';
a = findstr(s_f, hdr);
LB = hdr(a(2):a(2)+24*72);

freq_start = str2num(LB(72+1+12:2*72));
freq_stop = str2num(LB(2*72+1+12:3*72));
n_freq = str2num(LB(3*72+1+12:4*72));
f = linspace(freq_start, freq_stop, n_freq);
avg = str2num(LB(6*72+1+12:7*72));
tx_sled = str2num(LB(17*72+1+12:18*72));
if tx_sled == 1
    tx_sled = 'A';
elseif tx_sled == 2
    tx_sled = 'B';
else
    warning('This is a monostatic measurement')
end
rx_sled = str2num(LB(21*72+1+12:22*72));
if rx_sled == 1
    rx_sled = 'A';
elseif rx_sled == 2
    rx_sled = 'B';
else
    warning('This is a monostatic measurement')
end

%which antenna, if any, is moving:
s8 = 'Sled A movement';
s9 = 'Sled B movement';
s10 = 'Axis rotation';
a = findstr(s8, hdr);
b = findstr(s9, hdr);
c = findstr(s10, hdr);

if n_hdr==82
    movement = 'none';
    n_ang = 1;
    ant_start = 'N/A';
    ant_stop = 'N/A';
    %get antenna movement parameters:
elseif ~isempty(b)
    movement = 'B';
    SLED = hdr(b(2):b(2)+4*72);

```

```

elseif ~isempty(a)
    movement = 'A';
    SLED = hdr(a(2):a(2)+4*72);
elseif ~isempty(c)
    movement = 'D';
    SLED = hdr(c(2):c(2)+4*72);
end
if n_hdr>82 %if the measurement is more than a single frequency sweep,
    mov_start = str2num(SLED(72+1+13:2*72));
    mov_stop = str2num(SLED(2*72+1+13:3*72));
    n_ang = str2num(SLED(3*72+1+13:4*72));
end

%interpret antenna movement parameters:
if tx_sled==rx_sled & n_ang~=1 %if the measurement is monostatic,
    ang = linspace(mov_start,mov_stop,n_ang);
    if movement=='A'
        initial = A_position;
        ang = linspace(mov_start,mov_stop,n_ang);
    elseif movement=='D'
        initial = D_position;
        ang = linspace(mov_start,mov_stop,n_ang);
    elseif movement=='none'
        ang = abs(A_position - B_position);
    end
else %if the measurement is bistatic,
    if movement=='A'
        initial = B_position;
        ang = linspace(abs(initial-mov_start),abs(initial-
mov_stop),n_ang);
    elseif movement=='B'
        initial = A_position;
        ang = linspace(abs(initial-mov_start),abs(initial-
mov_stop),n_ang);
    elseif movement=='D'
        initial = D_position;
        ang = linspace(mov_start,mov_stop,n_ang);
    elseif movement=='none'
        ang = abs(A_position - B_position);
    end
end

%Christopher J Bradley
%2d Lt, USAF
%AFIT/ENG
%cbradley@ieee.org
%29 September 2000

```

```

%SCAT_PLOT_2D Plot normalized 2-D bistatic RCS with a dynamic range
%of 80 dBsm.
%scat_plot_2D(M,pol,x,domain)
%INPUTS:
%M -- input scattering matrix (2 x 2 x n_freq x n_ang)
%pol -- desired polarization to plot
%x -- vector of values of x-axis
%domain -- string with which to label x-axis

function scat_plot_2D(M,pol,x,domain)
global n_freq
global n_ang
global mnemonic
global object

if pol=='hh'
    r = 1;
    c = 1;
elseif pol=='vh'
    r = 1;
    c = 2;
elseif pol=='hv'
    r = 2;
    c = 1;
elseif pol=='vv'
    r = 2;
    c = 2;
else
    error('Unrecognized variable "pol" ')
end

figure(1)
theta = linspace(4,184,n_ang);
fig = abs(squeeze(M(r,c,:,:)));
fig_norm = 20*log10(fig/max(abs(M(:)))));
imagesc(x,theta,rot90(fig_norm),[-80 0]);
xlabel(domain)
ylabel('bistatic angle')
title([object(1:50),pol, ' pol',',', ',domain]);

%Christopher J Bradley
%2d Lt, USAF
%AFIT/ENG
%cbradley@ieee.org
%29 September 2000

```

```

%TFCONVERT  convert bistatic data between time and frequency domain
%S_tf = tfconvert(S,f,t,t_or_f)
%INPUTS:
%S -- input scattering matrix
%f -- vector of frequency values (in GHz)
%t -- vector of time values (in ns)--same length as "f"
%t_or_f -- to convert to time, t_or_f = 'time'
%         to convert to frequency, t_or_f = 'freq'
%OUTPUTS:
%S_tf -- transform-domain scattering matrix (identical dimensions
%as input structure "S")

function S_tf = tfconvert(S,f,t,t_or_f)
global n_ang

if t_or_f == 'time'
    sgn = 1;
    vec1 = f;
    vec2 = t;
elseif t_or_f == 'freq'
    sgn = -1;
    vec1 = t;
    vec2 = f;
else
    ERROR('Unknown input argument for "t_or_f":  Enter -1 or +1')
end

q = waitbar(0, 'Computing Chirp-z transform...');
for m=1:n_ang
    for n=1:2
        for p=1:2
            S_tf(p,n,:,m) = mchirpz(S(p,n,:,m),vec1,vec2,sgn);
        end
    end
    waitbar(m/n_ang);
end
close(q)

%Christopher J Bradley
%2d Lt, USAF
%AFIT/ENG
%cbradley@ieee.org
%29 September 2000

```

```

%TIME_GATE apply time gate to data using "mchirpz.m"
%S = time_gate(M,f,t)
%INPUTS:
%M -- input data
%f -- vector of frequency
%t -- vector of time (desired gate)
%OUTPUTS:
%M_fre -- gated frequency-domain data
%M_tim -- gated time-domain data (optional)

function [M_fre, M_tim] = time_gate(M,f,t)
global n_ang
global gate_start
global gate_stop
gate_start = t(1);
gate_stop = t(end);
n = length(f);

%create Hamming window:
H = hamming(n)';
big_H = zeros(2,2,n,n_ang);
for p = 1:2
    for n = 1:2
        for m = 1:n_ang
            big_H(p,n,:,m) = H;
        end
    end
end

>window in frequency:
M_win = M.*big_H;

%transform to time-domain:
q = waitbar(0, 'Applying gate...');
i=1;
for p=1:2
    for n=1:2
        for m=1:n_ang
            M_tim(p,n,:,m) = mchirpz(M_win(p,n,:,m),f,t,1);
            waitbar(i/4/n_ang/2,q)
            i=i+1;
        end
    end
end

%transform back to frequency-domain:
for p=1:2
    for n=1:2
        for m=1:n_ang
            M_win_ga(p,n,:,m) = mchirpz(M_tim(p,n,:,m),t,f,-1);
            waitbar(i/4/n_ang/2,q)
            i=i+1;
        end
    end
end
close(q)

```



```
%undo Hamming window:  
factor=(t(1)-t(end))*(f(2)-f(1));  
M_fre = factor*M_win_ga./big_H;
```

```
%Christopher J Bradley  
%2d Lt, USAF  
%AFIT/ENG  
%cbradley@ieee.org  
%29 September 2000
```

APPENDIX C: The EMSL

http://www.tdp.sai.jrc.it/TDP/test_and_evaluation_facilities.htm

Radar measurements

The European Microwave Signature Laboratory (EMSL)

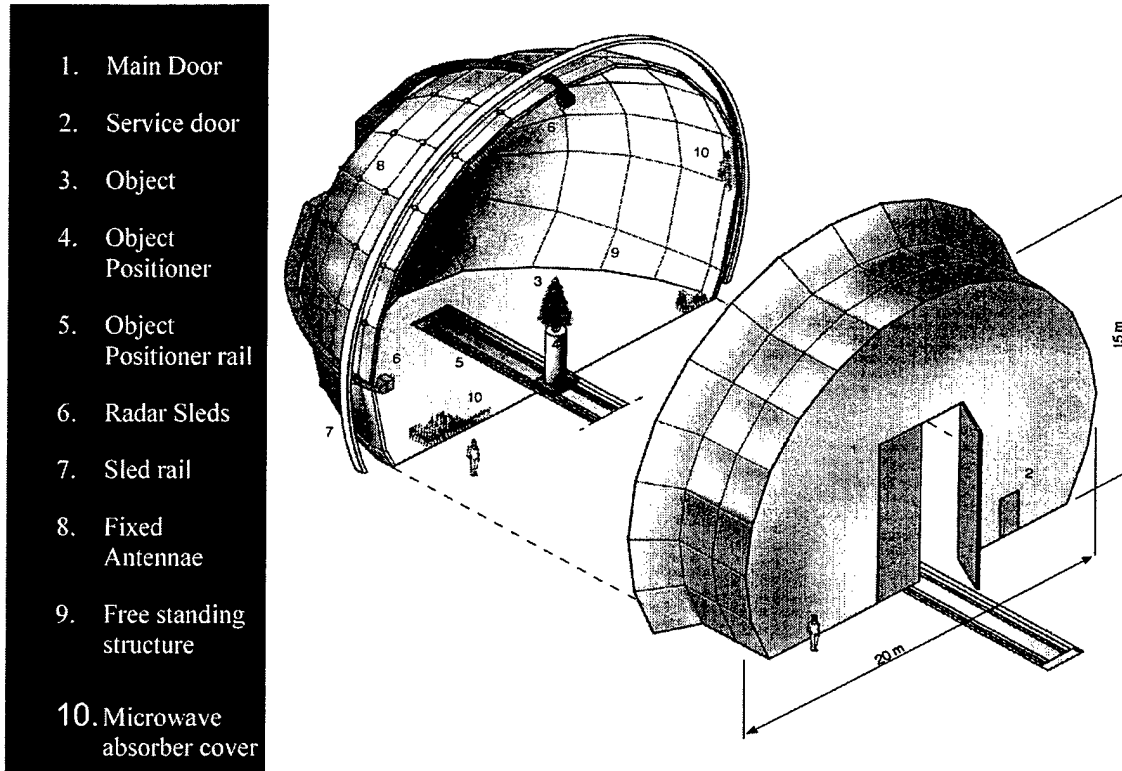


Table 1: Positioner Mechanical Specifications

Positioner	Range	Repeatability	Max Load
Radars	-110/110°	+/- 0.005°	50 Kg
Object (linear)	-2.5/2.5 m	+/- 0.5 mm	6000 Kg
Object (rotation)	0/360°	+/- 0.05°	6000 Kg

Table 2: Measurement Systems Specifications

Measurement configuration	mono/bistatic/multistatic
Frequency Range	0.5 - 26.5 GHz

Polarisation	Full polarimetric (HH, VH, HV, VV)
Measurement mode	Continuous Wave (Step or Ramp)
Detection	Coherent (phase locked)
Sensitivity	-60 dBsm
Dynamic Range	100 dB
Transmitted power	< 1 W

The European Microwave Signature Laboratory (EMSL) of the Space Applications Institute at the Joint Research Centre at Ispra (Italy) is designed for experiments in the field of radar signature research. It is a unique European facility which complements in-field, air- and space- borne radar measurements by providing stable and reproducible environmental conditions and operational modes for well controlled experiments of microwave scattering.

The EMSL consists of a large anechoic chamber, providing the environment and the facilities to perform radar measurements. The measurements essentially can provide the spatial scattering pattern of the object under test in a three-dimensional characterization. The radar scattering matrix is measured, which represents the Microwave Signature of the object, the most comprehensive information from active microwave measurements. Other widely used parameters such as the Radar Cross Section (RCS) can be directly derived from the scattering matrix. The variety of measurement options can be used in two basic ways: scatterometric and imaging modes.

The facility, in addition to the monostatic configuration of usual radar systems, offers polarimetric measurement features in bistatic and multistatic configurations. This gives additional dimensions in the measured data for characterizing an object, validating a model, or testing of new sensors.

The overall structure is made of a hemispherical and a cylindrical part, both with a diameter of 20 m. A circular rail is mounted between the two parts on which two sleds carrying antennas and other sensors are moved independently. Further, 37 receiving antennas are fixed on the inner surface of the hemisphere and are integrated in the microwave measurement system.

Objects of varied sizes and shapes can be located on the object positioner. The positioner moves on a rail to allow the precise linear and rotational positioning of the object under test inside the chamber for the microwave measurements. The spatial resolution depends on the measurement mode and parameters; it ranges from few meters to less than 1 cm.

The electro-mechanical devices and the microwave measurement system are remotely controlled. The control program allows user-defined sequences of operations to create measurement scenarios, including microwave measurements and data storage, sensor positioning and object movements. Complex, extended measurement sequences may be executed automatically by this control system.

All collected data (microwave data, system parameters, environmental conditions, optical images) are transferred to the EMSL Information Management System. This data archiving and handling system was especially developed to cope with the complex information management for all data generated by the EMSL activities and the related research.

The EMSL was first applied to the investigation of the use of radar to counter the APL threat some three years ago following a request from the European Parliament.

BIBLIOGRAPHY

1. Alexander, N. T., Currie, N. C., Tuley, M. T. "Calibration of Bistatic RCS Measurements." Proceedings of Antenna and Propagation Techniques Association (AMTA) 1995 Symposium. Columbus, OH: 13-17, November 1995.
2. Alexander, N. T., T. L. Lane, C. A. Blevins, "Overview of the Bistatic Coherent Measurement System (BICOMS)," Internal Memorandum, NRTF/RATSCAT, Holloman AFB, NM.
3. Balanis, C.A., Advanced Engineering Electromagnetics, John Wiley & Sons, Inc., New York, NY, 1989.
4. Bicci, Alberto, "Simulation Scattering Response of a Wire Mesh." Technical Report RT92/034, Ingegneria dei Sistemi s.p.a., August 1992. JRC/EMSL contract number 4801-92-05 ED-ISP-I.
5. Crispin, J.W. and K.M. Siegel, Methods of Radar Cross Section Analysis, Academic Press, New York, 1968.
6. Eigel, R. L., Jr., Bistatic Radar Cross Section Characterization of Complex Objects. MS thesis, AFIT/GE/ENG/99J-01, School of Electrical Engineering, Air Force Institute of Technology (AETC), Wright-Patterson AFB, OH, June 1999.
7. Falconer, David G., "Extrapolation of Near-Field RCS Measurements to the Far Zone", IEEE Transactions on Antennas and Propagation, June 1988, pp. 822-829.
8. Falconer, David G., "Near-field Statement of Monostatic-Bistatic Theorem", Abstracts: 1988 USRI National Radio Science Meeting, Boulder, CO, Jan. 1988.
9. S.J. Gabig, K.L. Wilson, P.J. Collins, A.J. Terzuoli, Jr., G. Nesti, and J. Fortuny, "Validation of Near-Field Monostatic to Bistatic Equivalence Theorem", Proceedings of the IEEE 2000 International Geoscience and Remote Sensing Symposium, 24-28 July 2000, pp. 1012-1014.
10. Harrington, R.F., Field Computation by Moment Methods, IEEE Press, 1993.
11. Jersak, B. D., Bistatic, Fully Polarimetric Radar Cross-Section Calibration Techniques and Measurement Error Analysis, PhD dissertation, The University of Texas at Arlington, December 1993.
12. Jost, R. J., R. F. Fahlsing, "Bistatic Cross-Polarization Calibration," Proceedings of the Antenna and Propagation Techniques Association (AMTA) 1997 Symposium, November 1997.

13. Kahny, D., K. Schmitt, W. Weisbeck, "Calibration of Bistatic Polarimetric Radar Systems," IEEE Transactions on Geoscience and Remote Sensing, vol. 30, no. 5, September 1992.
14. Kell, Robert E., "On the Derivation of the Bistatic RCS from Monostatic Measurements," Proceedings of the IEEE, Vol XX No Y: 983-988, Aug 1965.
15. Knott, E.F., J. F. Shaeffer, M. T. Tuley, Radar Cross Section, 2nd ed., Artech House, Norwood, MA, 1993.
16. Kouyoumjian, R. G., P. H. Pathak, "A Uniform Geometrical Theory of Diffraction for and Edge in a Perfectly Conducting Surface," Proceedings of the IEEE, vol. 62, no. 11, pp. 1448-1461, 1974.
17. McLaughlin, D. J., Z. Ren, Y. Wu, "A Bistatic Polarimeter Calibration Technique," IEEE Transactions on Geoscience and Remote Sensing, vol. 33, no. 3, May 1995.
18. Mortensen, H. B., "Implementation of Bistatic Polarimetric Calibration Procedure for the EMSL", European Microwave Signature Laboratory, 25 October 1995.
19. Mott, Harold, Antennas for Radar and Communications: A Polarimetric Approach, John Wiley & Sons, New York, NY, 1992.
20. Nesti, G. and M. Hohmann, "An Efficient Calibration Procedure for Polarimetric Radar Systems", International Geoscience and Remote Sensing Symposium, vol. II, pp. 1099-1103, Washington, D.C., 1990.
21. Nesti, G., A.J. Sieber, G. de Grandi, J. Fortuny, and E. Ohlmer, "Recent Advances at the European Microwave Signature Laboratory", SPIE Proceedings vol. 2313, Microwave Instrumentation and Satellite Photogrammetry for Remote Sensing of the Earth, pp 56 – 63, 28 – 30 Sept 1994, Rome, Italy.
22. Peterson, A. F., S. L. Ray, R. Mittra, Computational Methods for Electromagnetics, IEEE Press, New York, NY, 1998.
23. Peters, L., "Passive Bistatic Radar Enhancement Devices", The Proceedings of the Institution of Electrical Engineers, vol. 109, part C, no. 15, March 1962.
24. Sarabandi, K, F.T. Ulaby, M. A. Tassoudji, "Calibration of Polarimetric Radar Systems with Good Polarization Isolation," IEEE Transactions on Geoscience and Remote Sensing, vol. 28, no. 1, January 1990.
25. Tuley, M., "Draft (Rev 3) Calibration Procedures for BICOMS," Internal Memorandum, NRTF/RATSCAT, Holloman AFB, NM, 20 May 1998.

26. Tuley, M., "Full Polarimetric Calibration of BICOMS," Internal Memorandum, NRTF/RATSCAT, Holloman AFB, NM.
27. Tuley, M., N. Alexander, "Phase Calibration," Internal Memorandum, NRTF/RATSCAT, Holloman AFB, NM.
28. Ufimtsev, P. Y., "Comments on Diffraction Principles and Limitations of RCS Reduction Techniques", Proceedings of the IEEE, vol. 84, no. 12, pp. 1830-1852, 1996.
29. Ulaby, F. T., C. Elachi (ed.), Radar Polarimetry for Geoscience Applications, Artech House, Norwood, MA, 1990.
30. Umari, M. H., Ghodgaonkar, D. K., Varadan, V. V., and Varadan, V. K. "A Free-Space Bistatic Calibration Technique for the Measurement of parallel and Perpendicular Reflection Coefficients of Planar Samples." IEEE Transactions on Instrumentation and Measurement, Vol 40, No 1: 19-24, February 1990.
31. Weinberger, M. and G. Nesti, "Measurement of the Dielectric Constant of ROHACELL 51", EMSL Internal Work Notice (EMSL-IWN 10/10/94), Joint Research Center, Institute for Remote Sensing Applications, Advanced Techniques, 10 October 1994.
32. Whitt, Michael W., Fawwaz T. Ulaby, Paul Polatin, Valdis V. Liepa, "A General Polarimetric Calibration Technique," IEEE Transactions on Antennas and Propagation, vol. 39, no. 1, Jan 1991.

REPORT DOCUMENTATION PAGE

Form Approved
OMB No. 0704-0188

The public reporting burden for this collection of information is estimated to average 1 hour per response, including the time for reviewing instructions, searching existing data sources, gathering and maintaining the data needed, and completing and reviewing the collection of information. Send comments regarding this burden estimate or any other aspect of this collection of information, including suggestions for reducing the burden, to Department of Defense, Washington Headquarters Services, Directorate for Information Operations and Reports (0704-0188), 1215 Jefferson Davis Highway, Suite 1204, Arlington, VA 22202-4302. Respondents should be aware that notwithstanding any other provision of law, no person shall be subject to any penalty for failing to comply with a collection of information if it does not display a currently valid OMB control number.

PLEASE DO NOT RETURN YOUR FORM TO THE ABOVE ADDRESS.

1. REPORT DATE (DD-MM-YYYY) 07-03-2001		2. REPORT TYPE Thesis		3. DATES COVERED (From - To) Aug 1999 - March 2001	
4. TITLE AND SUBTITLE THE CALIBRATION OF BISTATIC RADAR CROSS SECTION MEASUREMENTS				5a. CONTRACT NUMBER	
				5b. GRANT NUMBER	
				5c. PROGRAM ELEMENT NUMBER	
6. AUTHOR(S) 2d Lt Christopher J Bradley				5d. PROJECT NUMBER	
				5e. TASK NUMBER	
				5f. WORK UNIT NUMBER	
7. PERFORMING ORGANIZATION NAME(S) AND ADDRESS(ES) Air Force Institute of Technology, Graduate School of Engineering and Management 2950 P Street, Bldg 640 WPAFB, OH 45433				8. PERFORMING ORGANIZATION REPORT NUMBER AFIT/GE/ENG/01M-03	
9. SPONSORING/MONITORING AGENCY NAME(S) AND ADDRESS(ES) Attn: Maj Kelce Wilson AFRL/SNAS Bldg 620 WPAFB, OH 45433				10. SPONSOR/MONITOR'S ACRONYM(S)	
				11. SPONSOR/MONITOR'S REPORT NUMBER(S)	
12. DISTRIBUTION/AVAILABILITY STATEMENT APPROVED FOR PUBLIC RELEASE, DISTRIBUTION UNLIMITED					
13. SUPPLEMENTARY NOTES					
14. ABSTRACT Recent advances in signal processing and remote sensing have highlighted the importance of bistatic radar systems for the purposes of environmental monitoring, surveillance, and tracking radar. The calibration of such systems has been problematic-much more so than similar monostatic systems, primarily as a result of the lack of reference objects suitable for calibrating at any given bistatic angle. This research deals with the problems of calibrating full-polarimetric laboratory-environment bistatic radar systems, including the lack of suitable calibration targets and procedures, and operational considerations such as alignment and mounting. Several popular bistatic calibration techniques are classified, evaluated, and comparisons are made between the relative merits of various calibration objects. The analysis addresses sensitivity to target alignment error, sensitivity to polarization impurity, and ease of implementation. Both theoretical concepts and practical considerations are discussed, based on measurements accomplished at the European Microwave Signature Laboratory (EMSL) of the Joint Research Center (JRC) in Ispra, Italy. Significant gains in co-polarized channel accuracy and cross-polarization purity are realized with calibrations that utilize the complete system distortion model, and these conclusions are discussed in detail.					
15. SUBJECT TERMS Bistatic, radar, calibration, measurement					
16. SECURITY CLASSIFICATION OF:			17. LIMITATION OF ABSTRACT	18. NUMBER OF PAGES 160	19a. NAME OF RESPONSIBLE PERSON
a. REPORT U	b. ABSTRACT U	c. THIS PAGE U			Dr. Andrew J. Terzuoli, Jr.
					19b. TELEPHONE NUMBER (Include area code) (937) 255-3636 x4717